이학박사 학위논문

Environmental Effects on Ultra-diffuse Galaxies and Jellyfish Galaxies in Massive Galaxy Clusters

무거운 은하단에 있는 크고 희미한 은하와 해파리은하의 환경 효과에 대한 연구

2022년 08월

서울대학교 대학원
물리·천문학부 천문학전공
이 정 환

Environmental Effects on Ultra-diffuse Galaxies and Jellyfish Galaxies in Massive Galaxy Clusters

무거운 은하단에 있는 크고 희미한 은하와 해파리은하의 환경 효과에 대한 연구

지도교수 이 명 균

이 논문을 이학박사 학위논문으로 제출함

2022년 05월

서울대학교 대학원

물리·천문학부 천문학전공

이 정 환

이 정 환의 이학박사 학위논문을 인준함

2022년 06월

위 원 장 __________________________

부 위 원 장 __________________________

위 원 __________________________

위 원 __________________________

위 원 __________________________

ABSTRACT

Gas-rich galaxies in dense environments evolve to gas-deficient galaxies due to tidal or hydrodynamic interactions with other galaxies or surrounding matter. These environmental effects closely involve the gas removal process or star formation activity in cluster galaxies, sometimes generating extreme galaxy populations in rich galaxy clusters. This thesis focuses on studying two different types of extreme galaxies, ultra-diffuse galaxies (UDGs) and jellyfish galaxies, in massive galaxy clusters. UDGs are abnormally large low surface brightness galaxies, and jellyfish galaxies are characterized by asymmetric tails and star-forming knots. To date, both types of galaxies have rarely been studied in massive clusters at intermediate redshift. In this thesis, we investigate the environmental effects on observational properties of UDGs and jellyfish galaxies in the clusters from the MAssive Cluster Survey (MACS) and Hubble Frontier Fields (HFF). For our scientific goals, we conduct three research projects using *HST* images and GMOS/IFU spectroscopic data.

First, we find 46 UDGs in a massive cluster, Abell 370 ($z = 0.375$), from the HFF images and combine the UDG sample with those in two other massive HFF clusters (Abell S1063 and Abell 2744). We analyze the properties of UDGs in these massive clusters in terms of 1) radial number density profile, 2) the relation between the abundance of UDGs (N(UDG)) and virial masses of the host systems (M_{200}), and 3) dynamical masses. The mean number density profile of UDGs shows a flattening as clustercentric distance decreases, while that of bright galaxies shows a continuous increase. This trend implies that UDGs are prone to disruption in the central region of the clusters. The $N(\mathrm{UDG}) - M_{200}$ relation is described by a power-law with an index of nearly one: $N(\mathrm{UDG}) \propto M_{200}^{1.00\pm0.05}$ for $M_{200} > 10^{13}\ M_{\odot}$. This relation indicates that the survival efficiency of UDGs is little dependent on their environments. We estimate approximate dynamical masses of UDGs and find that most UDGs have dwarf-like masses ($M_{200} < 10^{11}\ M_{\odot}$). This mass range implies that most UDGs have a dwarf-like origin, except for a small number of L^{*}-like galaxies. From these results, we conclude that the properties of UDGs in massive clusters are similar to those in the less massive environments in the local universe.

Second, we study the ionized gas properties of five jellyfish galaxies in massive clusters with Gemini GMOS/IFU observations: MACSJ0916-JFG1 ($z = 0.330$), MACSJ1752-JFG2 ($z = 0.353$), A2744-F0083 ($z = 0.303$), MACSJ1258-JFG1 ($z = 0.342$), and MACSJ1720-JFG1 ($z = 0.383$). Their host clusters are massive ($M_{200} \gtrsim 10^{15}\ M_\odot$) and X-ray luminous ($\log L_X \gtrsim 44.5$ erg s^{-1}), implying that jellyfish galaxies in these clusters are subject to much stronger ram-pressure stripping (RPS) than those in low-mass clusters. The Hα flux distributions are spatially consistent with stellar emission in all jellyfish galaxies. The radial velocity distributions of ionized gas seem to follow disk rotation of galaxies, with the appearance of a few high-velocity components in the tails as a sign of RPS. Mean gas velocity dispersion is lower than 50 km s^{-1} in most star-forming regions except near AGNs or shock-heated regions, indicating that ionized gas in most star-forming regions is dynamically cold. Integrated star formation rates (SFRs) are much higher than those of other jellyfish galaxies in the local universe. These high SFR values imply that RPS triggers intense star formation activity in these extreme jellyfish galaxies. The five jellyfish galaxies in this study have similar gas kinematics and dynamical states to those in the local universe, but they show a much higher SFR than the local jellyfish galaxies.

Finally, we perform a detailed analysis of the star formation activity of jellyfish galaxies, focusing on the short-term effect of ram-pressure stripping (RPS). It has been thought that the star formation activity of jellyfish galaxies may depend on the host cluster properties, but previous studies have not yet found a clear correlation. We estimate the Hα-derived star formation rates (SFRs) of five jellyfish galaxies in massive clusters ($\sigma_{v,\mathrm{cl}} \gtrsim 1000$ km s^{-1}) at $z \sim 0.3 - 0.4$ using Gemini GMOS/IFU observations to explore the relationship. Combining our results with those in the literature, we find that the star formation activity of jellyfish galaxies shows a positive correlation with their host cluster velocity dispersion as a proxy of cluster mass and dynamical states. We estimate their SFR excess relative to the star formation main sequence (starburstiness; $R_{\rm SB} = {\rm SFR}/{\rm SFR}_{\rm MS}(z)$) and the density of the surrounding intracluster medium (ICM) using scaling relations with the cluster velocity dispersion. As a result, the starburstiness of jellyfish galaxies with strong RPS signatures exhibits positive correlations with cluster velocity dispersion, ICM density, and strength of ram pressure. This relationship shows how ram pressure temporarily affects the star formation activity of jellyfish galaxies depending on the host cluster properties and degree of RPS.

Keywords: Galaxy clusters, Environmental effects, Galaxy evolution, Star formation, Ultra-diffuse galaxies, Jellyfish galaxies, Ram-pressure stripping

Student Number: 2015-22604

Contents

List of Figures

List of Tables

Chapter 1

Introduction

1.1 Galaxy Evolution via Environmental Effects

Environmental effects are crucial for understanding galaxy evolution in dense environments. Most gas-rich galaxies evolve into gas-deficient galaxies in galaxy groups or clusters, losing their gas by environmental effects. The environmental effects transform the observational properties of galaxies, such as morphology, mass, size, color, and star formation activity. The link between environment and galaxy properties was shown well by morphology-density relation (Dressler 1980; Postman & Geller 1984; Whitmore et al. 1993), which suggested that the fraction of spiral galaxies decreases and that of elliptical and S0 galaxies increases as the local galaxy density increases. In addition, the colors of galaxies become redder, and their star formation rates (SFRs) decrease as the local galaxy density increases, as shown in the studies using the 2dF Galaxy Redshift Survey (Lewis et al. 2002) and the Sloan Digital Sky Survey (SDSS; Gómez et al. 2003; Hogg et al. 2004; Bamford et al. 2009).

In dense environments, physical mechanisms of environmental effects on galaxies can be divided into two major categories: tidal interactions and hydrodynamic interactions with the surrounding matter. First, tidal interactions occur when galaxies experience gravitational forces by the close encounter with other neighboring galaxies (Toomre & Toomre 1972) or by the potential well of their host systems (Byrd & Valtonen

1990). This process can generate tidal relics such as galactic bridges and tails and even strip the interstellar medium (ISM) from galaxies (Toomre & Toomre 1972; Merritt 1983). When a galaxy undergoes multiple fly-by encounters with high-speed galaxies, so-called "galaxy harassment" (Moore et al. 1996, 1998), the galaxy can also lose its gas and be transformed into quiescent galaxies. Second, the ISM within galaxies can undergo hydrodynamic interactions with intracluster medium (ICM) filled with the host halo. When a galaxy moves through the intergalactic space with high velocity ($\gtrsim$ 1000 km s^{-1}), external pressure from the ICM exerts a force on ISM towards the opposite direction of the motion of the galaxy ("ram pressure"). This ram pressure can effectively strip gas from the galaxies, which is called "ram-pressure stripping" (RPS; Gunn & Gott 1972). The effect of viscosity and turbulence on the flow of hot ICM gas can also accelerate this stripping process (Nulsen 1982). In addition, the hot surrounding ICM ($T \sim 10^8$ K) can suppress the gas supply for cluster galaxies from gas-rich companions ("starvation"; Larson et al. 1980) or evaporate the cold ISM gas in galaxies ("thermal evaporation"; Cowie & Songaila 1977), which drives mass loss of the galaxies. As a result of these environmental effects, late-type galaxies in dense environments eventually lose their gas ingredients for star formation and evolve into early-type galaxies.

1.2 Extreme Galaxy Populations in Galaxy Clusters

During the galaxy transformation, the environmental effects give rise to a variety of galaxy populations in rich galaxy clusters compared to the low-density environments (Dressler 1984; Boselli & Gavazzi 2006). For instance, some cluster galaxies exhibit abnormal morphology or temporarily enhanced star formation activity, such as ultra-diffuse galaxies (UDGs; Sandage & Binggeli 1984; van Dokkum et al. 2015), ultra-compact dwarf galaxies (UCDs; Hilker et al. 1999; Drinkwater et al. 2000; Phillipps et al. 2001), brightest cluster galaxies (BCGs; Sandage 1972a,b), or jellyfish galaxies (Bekki 2009; Chung et al. 2009), in the intermediate phase of galaxy evolution.

The formation of these extreme galaxy populations involves closely with the environmental effects. First, UDGs are abnormally large ($R_{\rm eff} > 1.5$ kpc) low surface brightness (LSB) galaxies. These ghost-like galaxies are much more abundant in galaxy clusters than in the field or group environments (van der Burg et al. 2016; Román & Trujillo 2017b; Lee et al. 2017; Mancera Piña et al. 2018). UDGs can form via multiple routes of environmental effects such as RPS (Yozin & Bekki 2015) or tidal stripping (Carleton et al. 2019) and internal processes such as high-spin dark matter (Amorisco & Loeb 2016) or stellar feedback (Di Cintio et al. 2017). Second, UCDs are very compact ($R_{\rm eff} = 10 - 100$ pc) old stellar systems but much brighter than typical globular clusters ($-10 > M_V > -13.5$ mag), which are very abundant in the central region of clusters or near massive galaxies. UCDs might be remnant nuclei of tidally stripped dwarf galaxies (Bekki et al. 2003; Pfeffer & Baumgardt 2013) or massive globular clusters (Fellhauer & Kroupa 2002). Third, BCGs are the most luminous and massive ($\log M_*/M_\odot = 10.5 - 12.5$) galaxy, located in the cores of galaxy clusters. Previous studies stated that these giant galaxies have grown through the accretion of cold gas from the surrounding ICM (Fabian & Nulsen 1977; Fabian 1994) or repeated merger of low-mass galaxies (Ostriker & Hausman 1977; Merritt 1985). Finally, jellyfish galaxies are peculiar starburst galaxies characterized by disturbed tails and extraplanar star-forming clumps. They have primarily been found in the central region of galaxy clusters (Poggianti et al. 2016). Jellyfish galaxies are striking examples of ram-pressure stripped galaxies with enhanced star formation activity (Fujita & Nagashima 1999; Bekki & Couch 2003; Kronberger et al. 2008; Poggianti et al. 2017).

Among these extreme galaxy populations, this thesis focuses on the studies of UDGs and jellyfish galaxies. These two galaxy populations are different phases on the evolutionary track of galaxies undergoing RPS. While jellyfish galaxies show ongoing star formation in their ram-pressure stripped tails (Smith et al. 2010; Yagi et al. 2010; Arrigoni Battaia et al. 2012; Kenney et al. 2014), UDGs can be “post-RPS galaxies” with their gas components already blown away by ram pressure (Yozin & Bekki 2015; Grishin et al. 2021).

1.3 Ultra-diffuse Galaxies

1.3.1 What are UDGs?

The studies of UDGs have a long history. In the extensive photographic studies of the Virgo cluster, Sandage & Binggeli (1984) and Impey et al. (1988) discovered a new class of dwarf galaxies that have a large diameter ($\gtrsim$ 3 kpc) and low central surface brightness ($\mu_0(V) > 24$ mag arcsec^{-2}). They found about 20 such LSB galaxies, which are mainly located in the central region of the Virgo cluster. Caldwell & Bothun (1987) and Conselice et al. (2003) also found similar LSB galaxies in the Fornax cluster and the Perseus cluster, and these galaxies were called low-mass cluster galaxies (Conselice 2018, and references therein). van Dokkum et al. (2015) found such large LSB galaxies in the Coma cluster and renamed them "ultra-diffuse galaxies (UDGs)".

UDGs have exceptionally large sizes ($R_{\rm eff} > 1.5$ kpc) but low surface brightness ($\mu_0(g) > 24.0$ mag arcsec^{-2}), which are considered as the extreme version of LSB dwarf galaxies. UDGs are outliers from the conventional galaxy scaling relations, so they are one of the main interests in the studies of the LSB universe. **Figure 1.1** shows the color image of an example UDG in a massive cluster, Abell 370, in comparison with M104, a massive early-type disk galaxy.

1.3.2 Observational Properties of UDGs

Recent studies have found a large number of nearby UDGs in the environments of clusters (van der Burg et al. 2016; Yagi et al. 2016; Mihos et al. 2017; Venhola et al. 2017; Mancera Piña et al. 2018, 2019), groups (Merritt et al. 2016; Román & Trujillo 2017b; Shi et al. 2017; van der Burg et al. 2017; Cohen et al. 2018), and fields (Martínez-Delgado et al. 2016; Bellazzini et al. 2017; Trujillo et al. 2017; Román et al. 2019). The properties of UDGs vary with their host environments. Cluster UDGs generally have red colors ($g - i \sim 0.8$), round shapes (axis ratios $b/a \sim 0.8$), smooth exponential light profiles (Sèrsic indices $n \sim 1.0$), and gas-deficient properties (Koda et al. 2015; van Dokkum et al. 2015). Thus, UDGs in high-density environments are composed of old

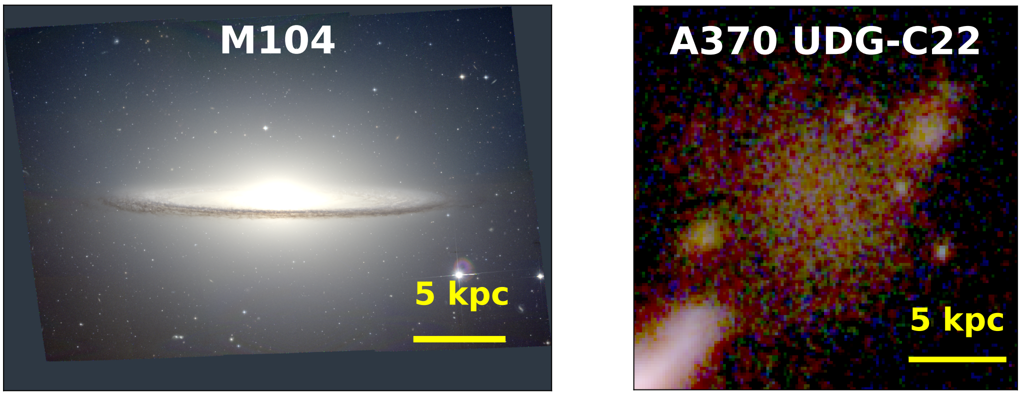

Figure 1.1. *HST* color images of M104 (left), a nearby giant E/S0 galaxy, and an example of UDGs in the Abell 370 cluster (right). *Credit (M104): NASA and the Hubble Heritage Team (STScl/AURA)*

stellar populations, and their star formation activity is expected to have been quenched early by gas removal processes. In contrast, most UDGs in low-density environments have bluer colors ($g - i < 0.5$), irregular shapes with star-forming knots, and relatively high HI masses ($M_{\rm HI} \sim 10^8\ M_\odot$) (Román & Trujillo 2017b; Spekkens & Karunakaran 2018). Therefore, these isolated UDGs have young stellar populations and gas-rich properties. The existence of these various types of UDGs in different environments gives us questions about the origin of UDGs.

1.3.3 Recent Issues on UDGs

A key motivation of the studies of UDGs is their formation mechanisms. There are three main scenarios proposed to explain the formation of UDGs in the literature (Amorisco & Loeb 2016; van Dokkum et al. 2016; Di Cintio et al. 2017; Bennet et al. 2018, and references therein). In the first scenario, the so-called "failed galaxies" scenario, UDGs failed to generate a typical amount of stars given their halo masses due to environmental effects. In the second scenario, the "extended dwarf galaxies" scenario, UDGs were extended from normal dwarf galaxies due to internal processes. In the third scenario, UDG progenitors were tidally extended by interactions with neighboring massive galaxies. Since diverse types of UDGs have been found by observations, recent studies have mostly suggested mixed formation mechanisms of UDGs with a combination of the above scenarios (Lee et al. 2017; Papastergis et al. 2017; Alabi et al. 2018; Ferré-Mateu et al. 2018; Lim et al. 2018; Pandya et al. 2018).

Another important issue in the studies of UDGs is the relation between the abundance of UDGs (N(UDG)) and the dynamical masses of their hosts (M_{200}): $N(\mathrm{UDG}) \propto M_{200}^{\alpha}$. The slope of this power-law relation (α) implies how efficient UDGs survive in their host environments. Most previous studies suggested that the slope is nearly one, which implies that the survival efficiency of UDGs does not strongly depend on the masses of their hosts. However, previous searches for UDGs were limited to the low-mass host systems with $M_{200} < 10^{15}\ M_{\odot}$. Thus, more observational studies for UDGs in massive host systems are needed to constrain this relation.

1.4 Jellyfish Galaxies

1.4.1 What are Jellyfish Galaxies?

In high-density environments, some late-type galaxies undergoing RPS show one-sided tails and locally star-forming regions from disks to tails. Bekki (2009) and Chung et al. (2009) found such galaxies with elongated gaseous tails under the effect of RPS using simulations and HI observations, and they first called them "jellyfish galaxies". These jellyfish galaxies have been primarily found in nearby clusters. In the Virgo and Coma clusters, several jellyfish galaxies were found to exhibit a large number of blue knots emitting ultraviolet (UV) light (Hester et al. 2010; Smith et al. 2010; Yoshida et al. 2012; Cramer et al. 2019) or "spur clusters" throughout their disks (Lee & Jang 2016). In addition, spectroscopic studies detected extraplanar Hα-emitting blobs outside the disks of jellyfish galaxies in Abell 3558 (Merluzzi et al. 2013), Abell 3627 (Fumagalli et al. 2014), Abell 2670 (Sheen et al. 2017), and galaxy clusters of the OMEGAWINGS

Figure 1.2. *HST* color image of an example jellyfish galaxy, ESO 137-001, undergoing ram-pressure stripping in the central region of Abell 3627 cluster. *Credit: NASA, ESA*

and WINGS sample at $z = 0.04 - 0.07$ (Poggianti et al. 2016, 2017). **Figure 1.2** shows the color image of a spectacular jellyfish galaxy, ESO 137-001, in Abell 3627.

The young stellar systems in jellyfish galaxies imply that RPS can locally boost the star formation activity in gas-rich galaxies before removing gas completely. Although RPS is known as the most efficient mechanism for halting the star formation activity of cluster galaxies by removing their gas (Dressler 1980; Vollmer et al. 2001; Boschin et al. 2006; Vulcani et al. 2022), RPS can also temporarily induce the star formation in galaxies by compressing the stripped gas. The star formation enhancement can be also supported by simulations (Bekki & Couch 2003; Kronberger et al. 2008; Kapferer et al. 2009) and the "fireball" model (Kenney et al. 2014; Jáchym et al. 2019). Thus, jellyfish galaxies show an interesting snapshot of starburst galaxies undergoing RPS.

1.4.2 Integral Field Spectroscopy of Jellyfish Galaxies

Integral field spectroscopy (IFS) is very useful for investigating the properties of jellyfish galaxies, providing both spatial and spectral information. Thus, recent observational studies of jellyfish galaxies have widely utilized IFS with the integral field unit (IFU) instruments. For instance, the GAs Stripping Phenomena (GASP) survey has observed a large sample of jellyfish galaxies in the nearby clusters from the OMEGAWINGS and WINGS surveys, using Multi Unit Spectroscopic Explorer (MUSE) on Very Large Telescope (VLT) (Poggianti et al. 2017). In addition, there are other IFS observation programs with Wide Field Spectrograph (WiFeS; Merluzzi et al. 2013), MUSE (Fumagalli et al. 2014; Fossati et al. 2016), and SITELLE (Liu et al. 2021), which also detected disturbed Hα morphology of jellyfish galaxies.

These IFS studies analyzed the kinematics, dynamical states, ionization mechanisms, and star formation activity of disks and tails in the jellyfish galaxies. Studies from the GASP survey found that star-forming knots in jellyfish galaxies are in situ formed, dynamically cold ($\sigma_{v,\rm gas} < 40$ km s^{-1}), and excited mainly by photoionization (Bellhouse et al. 2017, 2019). They obtained a mean star formation rate (SFR) of ~ 1.8 $M_\odot$ yr^{-1} in the disks and ~ 0.13 $M_\odot$ yr^{-1} in the tails of jellyfish galaxies (Poggianti et al. 2019; Gullieuszik et al. 2020). In the SFR$-M_*$ relation, Vulcani et al. (2018) revealed that jellyfish galaxies show enhanced star formation activity by a 0.2 dex compared to the star-forming galaxies without RPS. Gullieuszik et al. (2020) showed that the star formation rates (SFRs) in the disks and tails of the GASP jellyfish galaxies have complex relationships with galaxy stellar mass, host cluster mass, clustercentric distance, and relative velocity to the ICM. From these results, the IFS observations, including the GASP survey, have successfully provided a comprehensive view of the star formation activity of jellyfish galaxies at low redshift ($z < 0.1$).

1.4.3 Necessity of Studying Jellyfish Galaxies in Massive Clusters

Previous IFS studies on jellyfish galaxies have been limited to relatively low-mass clusters with cluster velocity dispersion ($\sigma_{v,\mathrm{cl}}$) lower than 1000 km s^{-1}. Host clusters of the GASP jellyfish galaxies on average have low cluster velocity dispersion ($\langle\sigma_{v,\mathrm{cl}}\rangle = 730$ km s^{-1}) and low X-ray luminosity ($\log L_X < 44.5$ erg s^{-1}). This implies that most GASP jellyfish galaxies are likely to experience weak or mild RPS effects with low ICM density, so the properties of jellyfish galaxies under strong RPS effects in massive clusters remain unclear.

On the other hand, massive clusters have high velocity dispersion of member galaxies ($\sigma_{v,\mathrm{cl}} \gtrsim 1000$ km s^{-1}) and high X-ray luminosity ($\log L_X \gtrsim 44.5$ erg s^{-1}). This indicates that the hosted jellyfish galaxies are likely to move at a higher speed and be surrounded by denser ICM than in low-mass clusters. In addition, massive clusters tend to be dynamically unstable with cluster collision or major merger, exerting shocks to their member galaxies (Mann & Ebeling 2012; Owers et al. 2012). These physical conditions can lead to extreme RPS effects for jellyfish galaxies in massive clusters (Ebeling et al. 2014; McPartland et al. 2016; Ebeling & Kalita 2019).

Indeed, previous RPS simulations predicted that higher ram pressure temporarily enhances the star formation activity in jellyfish galaxies. For instance, Kapferer et al. (2009) and Steinhauser et al. (2012) suggested that a high ram-pressure environment ($P_{\mathrm{ram}} > 10^{-11}$ dyn cm^{-2}) with dense ICM ($\rho_{\mathrm{ICM}} = 10^{-27}$ g cm^{-2}) can enhance the

SFR of jellyfish galaxies by more than a magnitude compared to a low ram-pressure environment ($P_{\rm ram} < 10^{-11}$ dyn cm^{-2}). Thus, jellyfish galaxies in massive clusters are useful for investigating the relationship between their star formation activity and the strength of RPS.

Using *HST* high-resolution images, previous studies found several dramatic jellyfish galaxies in massive clusters in massive clusters at intermediate redshift ($z > 0.1$). Owen et al. (2006) and Cortese et al. (2007) found three disturbed jellyfish galaxies with blue star-forming knots in the multi-band *HST* optical images and radio images: C153 (Abell 2125; $z = 0.253$), 131124-012040 (Abell 1689; $z = 0.187$), and 235144-260358 (Abell 2667; $z = 0.227$). Owers et al. (2012) studied four jellyfish galaxies with highly asymmetric tails and very bright star-forming knots in a massive merging cluster Abell 2744, using the *HST* optical images and AAOmega spectra. Ebeling et al. (2014) and McPartland et al. (2016) performed a systematic search of jellyfish galaxies using the *HST* images of the Massive Cluster Survey (MACS; Ebeling et al. 2001, 2010) and provided a catalog of 16 jellyfish galaxies in the MACS cluster samples at $z > 0.3$ ($\langle M_{\rm tot}\rangle \sim 1.3 \times 10^{15}\ M_{\odot}$). These jellyfish galaxies in massive merging host clusters are characterized by highly asymmetric tails and very bright star-forming knots in common.

However, there have been only a few IFS observations of these jellyfish galaxies in massive clusters (Boselli et al. 2019; Kalita & Ebeling 2019; Moretti et al. 2022). Two of the three previous IFS studies could not cover the Hα emission line associated with the star formation activity due to low sensitivity or limit of wavelength coverage. Thus, more IFS observations of jellyfish galaxies in massive clusters are required to reveal the influence of strong RPS on the physical properties of the jellyfish galaxies.

1.5 Outline of the Thesis

Massive galaxy clusters are an excellent laboratory to study the relationship between the environment and the properties of UDGs and jellyfish galaxies. Since high-mass clusters more massive than the Coma cluster ($M_{200} \sim 10^{15}\ M_{\odot}$) are rare in the nearby universe, galaxy clusters at intermediate redshifts can be good targets to observe the extreme galaxies. Thus, this thesis investigates the influence of environments on the properties of UDGs and jellyfish galaxies in massive clusters at $z > 0.3$. We then compare their observational properties with those in lower-density environments such as galaxy groups or low-mass clusters in the local universe.

In this thesis, we use high-resolution images and integral-field spectroscopic data to achieve the scientific goals. For studying UDGs in massive clusters, we detect UDGs in Abell 370, a very massive cluster ($M_{200} > 2 \times 10^{15}\ M_{\odot}$) of the Hubble Frontier Fields (HFF). Combining this sample with UDGs found in the other two HFF clusters (Abell S1063 and Abell 2744), we analyze the properties of UDGs in massive clusters and compare them to those in nearby low-mass clusters. For studying jellyfish galaxies in massive clusters, we study the physical properties of five jellyfish galaxies in the MACS clusters and Abell 2744 using the IFU instrument of Gemini Multi-Object Spectrograph (GMOS) on the 8-m Gemini telescope. We analyze the ionized gas properties with strong emission lines (Hβ, [OIII], Hα, [NII], etc.) and compare them to the properties of jellyfish galaxies in low-mass clusters.

This thesis is organized as follows. In **Chapter 2**, we present the study of UDGs in the HFF clusters. We derive the color, structural parameter, radial number density profile, and total abundance of UDGs and discuss the formation scenarios of UDGs and their environmental effects. In **Chapter 3**, we present the results of GMOS/IFU observations of five jellyfish galaxies in the MACS clusters and Abell 2744. We address how SFRs, kinematics, and ionization mechanisms of jellyfish galaxies are related to their environments. The main conclusions of this thesis are summarized in **Chapter 4**.

Chapter 2

The Nature of UDGs in Massive Clusters of the Hubble Frontier Fields

(This chapter is published in *The Astrophysical Journal.*)[†]

2.1 Introduction

In the extensive photographic studies of the Virgo cluster, Sandage & Binggeli (1984) discovered a new class of dwarf galaxies which have very large diameter (~10 kpc) and low central surface brightness ($\mu_0(B) > 25$ mag arcsec^{-2}). They found about 20 such low surface brightness (LSB) galaxies, which are mainly located in the central region of the Virgo cluster. Similar LSB galaxies were found in other galaxy clusters later and they were called low-mass cluster galaxies (Conselice et al. (2003), Conselice (2018), and references therein). van Dokkum et al. (2015) found such large LSB galaxies in the Coma cluster and renamed them "ultra-diffuse galaxies (UDGs)". UDGs have exceptionally large sizes ($R_{\rm eff} > 1.5$ kpc) but low surface brightness ($\mu_0(g) > 24.0$ mag arcsec^{-2}). Thus, UDGs seem to be the extreme case of LSB dwarf galaxies.

[†] Lee, J. H., Kang, J., Lee, M. G., et al. 2020, ApJ, 894, 75. doi:10.3847/1538-4357/ab8632

UDGs have been found in various environments. In cluster environments, there are hundreds of UDGs detected in the Coma cluster (Koda et al. 2015; Yagi et al. 2016), the Fornax cluster (Caldwell & Bothun 1987; Muñoz et al. 2015; Venhola et al. 2017), the Virgo cluster (Sandage & Binggeli 1984; Impey et al. 1988; Mihos et al. 2015, 2017), eight clusters at $z = 0.044 - 0.063$ from Multi-Epoch Nearby Cluster Survey (MENeaCS) (van der Burg et al. 2016), Abell 168 (Román & Trujillo 2017a), the Perseus cluster (Conselice et al. 2003; Wittmann et al. 2017), 18 clusters from MENeaCS (Sifón et al. 2018), 8 clusters from the Kapteyn IAC WEAVE INT Clusters Survey (KIWICS) (Mancera Piña et al. 2018, 2019), Abell S1063 (Lee et al. 2017), and Abell 2744 (Janssens et al. 2017; Lee et al. 2017). In group environments, UDGs were found in the NGC 5485 group (Merritt et al. 2016), Hickson Compact Groups (HCGs) (Román & Trujillo 2017b; Shi et al. 2017), galaxy groups from the KiDS and GAMA fields (van der Burg et al. 2017), the Leo-I group (Müller et al. 2018), and galaxy groups from the Dragonfly Nearby Galaxies Survey (Cohen et al. 2018). Isolated UDGs are rare, but some have been found in wide field surveys: DGSAT-I (Martínez-Delgado et al. 2016), UGC 2162 (Trujillo et al. 2017), SdI-1 and SdI-2 (Bellazzini et al. 2017), HI-bearing ultra-diffuse sources (HUDS) (Leisman et al. 2017), low surface brightness galaxies (LSBGs) from Hyper Suprime-Cam Subaru Strategic Program (HSC-SSP) (Greco et al. 2018a), and S82-DG-1 (Román et al. 2019).

The properties of UDGs vary with their environments. Cluster UDGs generally have red colors ($g - i \sim 0.8$), round shapes (axis ratios $b/a \sim 0.8$), smooth exponential light profiles (Sèrsic indices $n \sim 1.0$), and gas-deficient properties (Koda et al. 2015; van Dokkum et al. 2015). Thus, UDGs in high density environments are composed of old stellar populations, and their star formation is considered to have been quenched at an early time by gas removal processes. In contrast, most UDGs in low density environments have bluer colors ($g - i < 0.5$), irregular shapes with star-forming knots, and relatively high HI masses ($M_{\rm HI} \sim 10^8\ M_\odot$) (Román & Trujillo 2017b; Spekkens & Karunakaran 2018). Therefore, these isolated UDGs have young stellar populations and gas-rich properties. The existence of these various types of UDGs in different environments continues to give us questions about the origin of UDGs.

A key motivation of the studies of UDGs is their formation mechanisms. There are three main scenarios proposed to explain the formation of UDGs in the literature (Amorisco & Loeb (2016); van Dokkum et al. (2016); Di Cintio et al. (2017); Bennet et al. (2018) and references therein). In the first scenario, the so-called "failed galaxies" scenario, UDGs failed to generate a typical amount of stars given their halo masses due to environmental effects. In the second scenario, the "extended dwarf galaxies" scenario, UDGs were extended from normal dwarf galaxies due to internal processes. In the third scenario, UDG progenitors were tidally extended by interactions with neighboring massive galaxies. Since diverse types of UDGs have been found in observations, recent studies have mostly suggested mixed formation mechanisms of UDGs with a combination of the above scenarios (Lee et al. 2017; Papastergis et al. 2017; Alabi et al. 2018; Ferré-Mateu et al. 2018; Lim et al. 2018; Pandya et al. 2018).

In this work, we search for UDGs in the massive galaxy cluster Abell 370 ($z = 0.375$) in the Hubble Frontier Fields (HFF) (Lotz et al. 2017), following our previous work on UDGs in Abell S1063 and Abell 2744 (Lee et al. 2017). We use very deep HFF archival images to search for UDGs in the clusters. We combine the results of this work and the previous work of Abell S1063 and Abell 2744 to understand the nature of UDGs in massive galaxy clusters. After submitting the first draft of our paper, Janssens et al. (2019) presented a study of UDGs and ultra compact galaxies in six HFF clusters including Abell 370. In this study, we cover not only UDGs but also LSB dwarfs in the clusters.

This chapter is organized as follows. We describe the data from the HFF and our data analysis in **Section 2.2**. We explain how we determined the depth of the HFF data, performed photometry, and selected UDG samples. In **Section 2.3**, we show our main results: color-magnitude diagrams (CMDs), color-color diagrams (CCDs), distribution of structural parameters of the UDGs, radial number density profiles (RDPs) of the UDGs, the abundance of UDGs, and estimation of their dynamical masses. Then, we present implications of the results and discuss the nature of UDGs in **Section 2.4**. We

Table 2.1. Physical Parameters of Abell 370 cluster

Parameter	Value	References
Redshift	$z = 0.375$	1
Distance Modulus	$(m-M)_0 = 41.44$	1
Luminosity Distance	1942 Mpc	1
Angular Distance	1028 Mpc	1
Scale	4.984 kpc arcsec^{-1}	1
Age at Redshift	9.366 Gyr	1
Virial Radius	$r_{200} = 8\overset{\prime}{.}52 \pm 0\overset{\prime}{.}36 = 2.55 \pm 0.11$ Mpc	2 (weak+strong lensing analysis)
Virial Mass	$M_{200} = (3.03 \pm 0.37) \times 10^{15}\ M_{\odot}$	2,3 (weak+strong lensing analysis)
Foreground Reddening	$E(B-V) = 0.028$ mag	4
Surface Brightness Dimming	$10 \log(1+z) = 1.38$ mag arcsec^{-2}	1

Notes.

References: (1) NASA/IPAC Extragalactic Database; (2) Umetsu et al. (2011); (3) Broadhurst et al. (2008); (4) Schlafly & Finkbeiner (2011).

present our conclusions and summary in **Section 2.5**.

We adopt the ΛCDM cosmological parameters with $H_0 = 73$ km s^{-1} Mpc^{-1}, $\Omega_M = 0.27$, and $\Omega_\Lambda = 0.73$. The luminosity distance of Abell 370 for these parameters is $d_L = 1942$ Mpc and the angular diameter distance is $d_A = 1028$ Mpc. The virial radius and mass of this cluster are adopted from a lensing analysis using deep and wide-field Suprime-Cam imaging (Broadhurst et al. 2008; Umetsu et al. 2011): $r_{200} = 2.55 \pm 0.11$ Mpc and $M_{200} = (3.03 \pm 0.37) \times 10^{15}\ M_{\odot}$. The foreground reddening value toward Abell 370 is $E(B-V) = 0.028$ (Schlafly & Finkbeiner 2011). **Table 2.1** shows the basic physical parameters of the Abell 370 cluster.

2.2 Data and Data Analysis

2.2.1 Data

We obtained deep and high-resolution images of Abell 370 from the HFF archive (Lotz et al. 2017). We chose drizzled images of ACS/WFC $F606W(V)$, $F814W(I)$, WFC3/IR $F105W(Y)$, and $F160W(H)$ for our analysis. The HFF images we used cover two fields with different clustercentric distances (r/r_{200}): the central field ($r/r_{200} < 0.2$) and the parallel field ($r/r_{200} \sim 0.6 - 0.8$) located at $6'$ southeast of the central field. We used the areas that both ACS/WFC and WFC3/IR covered: ~5.5 acrmin^2 for the central field, and ~5.0 arcmin^2 for the parallel field. The pixel scale of all the drizzled images is $0\farcs03$ per pixel, and the scale for the distance to Abell 370 is 4.984 kpc arcsec^{-1}.

Among the multi-wavelength bands of the HFF images, $F814W$ and $F105W$ images are the most useful for finding UDGs in Abell 370. This is because $F814W$ and $F105W$ have the longest exposure times among the available bands, and the spectral energy distributions (SEDs) of cluster galaxies are dominant at these wavelengths considering the cluster redshift ($z = 0.375$). The exposure times for the images of the central field are 36.3 hours ($F814W$) and 19.3 hours ($F105W$), and those of the parallel field images are 29.3 hours ($F814W$) and 20.3 hours ($F105W$). The FWHMs of point spread functions (PSFs) are $0\farcs09$ (~ 0.45 kpc) in $F814W$ and $0\farcs16$ (~ 0.80 kpc) in $F105W$. We adopted the foreground extinction values of $A_{F814W} = 0.049$ mag and $A_{F105W} = 0.031$ mag given in the HFF-DeepSpace photometric catalogs (Shipley et al. 2018) for CMDs and CCDs.

To estimate background contributions, we used ACS/WFC $F814W$ and WFC3/IR $F105W$ images of the Hubble eXtreme Deep Field (XDF) (Illingworth et al. 2013). The total exposure times are 14.1 hours in $F814W$ and 74.1 hours in $F105W$. We chose only the deepest regions of the whole XDF, the HUDF09 and the HUDF12 programs, which cover ~ 5.06 arcmin^2. Thus, the areas for the central field of Abell 370 (~ 5.50 arcmin^2), the parallel field (~ 5.00 arcmin^2), and the XDF (~ 5.06 arcmin^2) are similar. Galaxies in the XDF have a wide range of redshifts, but we assume all of them have

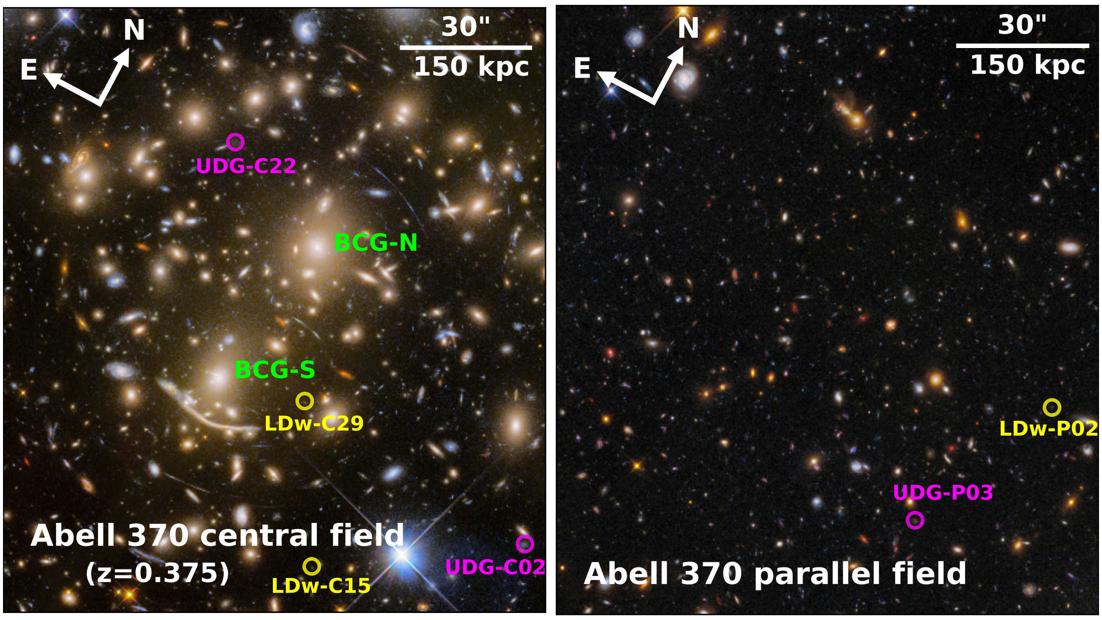

Figure 2.1. False color images of Abell 370 in the HFF: the central field (left) and the parallel field (right). These images were combined with multi-band images from optical ($F435W$, $F606W$, and $F814W$) to near-infrared ($F105W$, $F125W$, $F140W$, and $F160W$) (Lotz et al. 2017). The magenta circles are UDG examples and the yellow circles are LSB dwarf examples. Two brightest cluster galaxies, BCG-N (north) and BCG-S (south), are labeled in green. The orientation and the image scale are shown at the top. *Credit: NASA, ESA/Hubble, and HST Frontier Fields*

the same redshift as Abell 370 ($z = 0.375$) to estimate the background contamination in the sample of Abell 370.

Figure 2.1 shows the color composite images of the central field (left panel) and the parallel field (right panel) of Abell 370. In the left panel, the central field shows diverse types of galaxies: two brightest cluster galaxies (BCGs) dubbed “BCG-N” and “BCG-S”, a sequence of bright red ellipticals at the north, and a large number of gravitationally lensed galaxies. Among them, examples of LSB galaxies including UDGs and LSB dwarfs (LDws) (see the text in **Section 2.2.2**) are marked by magenta and yellow circles. ‘C’ and ‘P’ in the names of these LSB galaxies mean the central field and

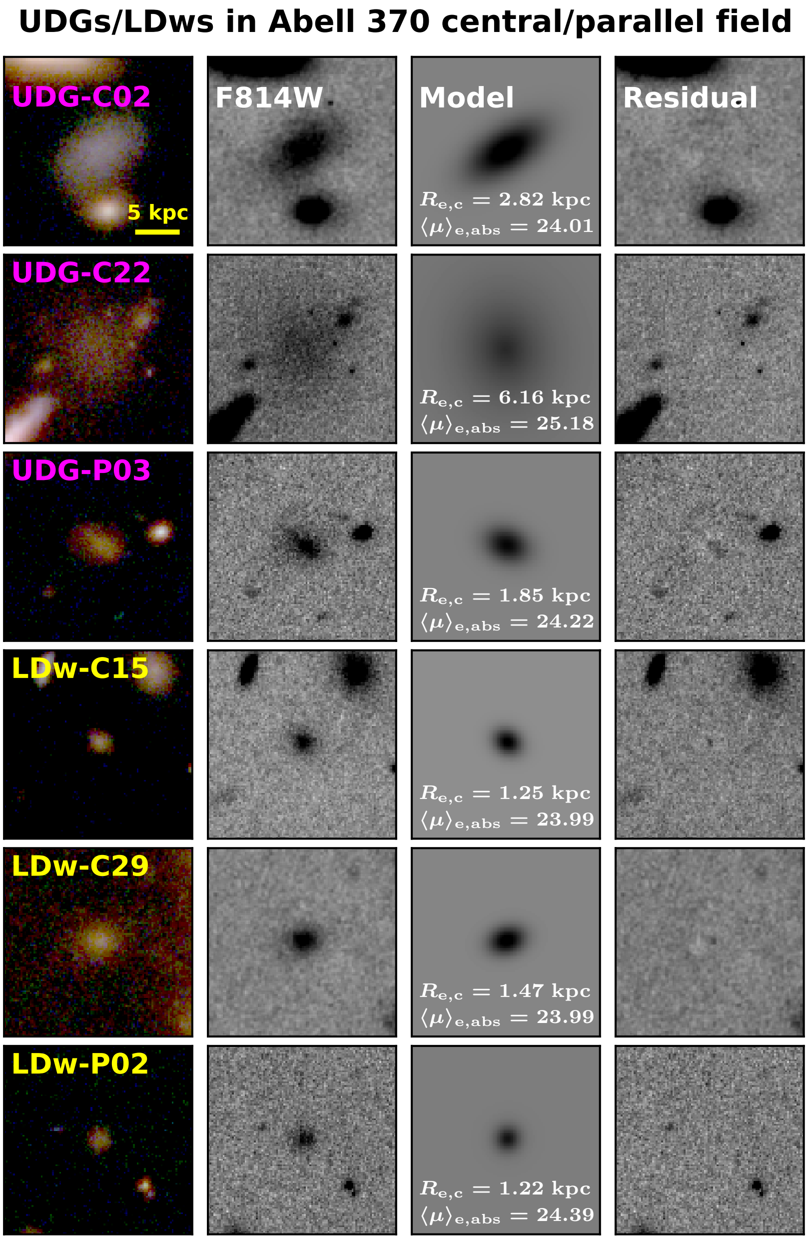

Figure 2.2. Thumbnail images ($4.''5 \times 4.''5$) of UDGs and LSB dwarfs denoted in **Figure 2.1**. The first column shows RGB color images of each sample (Blue : $F435W + F606W$ images, Green : $F814W$ images, and Red : $F105W$ images). The second column shows $F814W$ images, which were used as input images for GALFIT. The last two columns show galaxy model images and their residual images from GALFIT measurements. Derived effective radii and surface brightness are marked.

the parallel field of Abell 370. In the right panel, the parallel field seems to have a much lower number density of bright galaxies. This means that the parallel field has a fewer number of cluster member galaxies than the central field. We marked some examples of UDGs and LSB dwarfs in the parallel field with circles.

Figure 2.2 shows the zoom-in thumbnail images of the LSB galaxies marked in **Figure 2.1**. The first column is the color images, and the second is $F814W$ band images. We estimated the sizes and surface brightness of these galaxies using GALFIT version 3.0.5 (Peng et al. 2010) as described in **Section 2.2.2**. The third and fourth column show the results from GALFIT, which are galaxy model images and subtracted images, respectively. The subtracted images show little of original galaxy images, showing that GALFIT did a good job in galaxy modeling. Most of the LSB galaxies show red colors in their color composite images. However, one of them (UDG-C02) shows a much bluer color than the others. We discuss this with our CMDs and CCDs in **Section 2.3**.

2.2.2 Photometry and Initial Sample Selection

We performed dual mode photometry using SExtractor (Bertin & Arnouts 1996). We set $F814W$ images as detection images. Our configuration parameters for SExtractor photometry are summarized in **Table 2.2**. These parameters are very similar to those used in Lee et al. (2017), which are considered to be effective for detecting LSB galaxies. We used the magnitude zeropoints of the AB system for the standard calibration. In the initial output catalogs of SExtractor, 18,315 sources were extracted in the central field and 15,998 sources in the parallel field. **Table 2.3** shows the numbers of sources in each step of the sample selection. Each sample selection step is described below.

First, we selected initial galaxy candidates using the following criteria: `MAGERR_AUTO` < 1.0, `FLAGS` < 4, `CLASS_STAR` < 0.4, and $-0.5 < F814W - F105W < 1.0$. This left 3,748 objects in the central field, 2,789 objects in the parallel field, and 2,252 objects in the area of the XDF we used (the HUDF09 and the HUDF12). Next, we classified these objects into two types of galaxies, bright galaxies and LSB galaxies. We used the surface brightness and effective radii conditions: bright galaxies with `MU_MAX`$(F814W) < 22.5$

Table 2.2. Source Extractor Input Parameters Used in **Section 2.2.2**

Parameter name	Input configuration
`DETECT_MINAREA`	20 pixels
`DETECT_THRESH`	0.7
`ANALYSIS_THRESH`	0.7
`FILTER_NAME`	tophat_3.0_3x3.conv
`DEBLEND_NTHRESH`	32
`DEBLEND_MINCONT`	0.005
`PHOT_AUTOPARAMS`[a]	2.5, 3.5
`PHOT_AUTOPARAMS`[b]	1.25, 1.75
`BACK_SIZE`	32 pixels
`BACKPHOTO_TYPE`	LOCAL

Notes.

[a] These values are set to be default in SExtractor. We used these values to measure `MAG_AUTO` for aperture magnitudes.

[b] We set different values of `PHOT_AUTOPARAMS` when measuring colors of sources, because smaller aperture radii can lead to higher signal-to-noise ratio.

Table 2.3. Numbers of Selected Sources in Each Step

Sources	The Central Field	The Parallel Field	The XDF
Step 1. SExtractor photometry			
Total detected sources	18,315	15,998	12,014
Galaxy candidates	3,748	2,789	2,252
Initial bright galaxies	334	115	84
Initial LSB galaxies (UDGs + LSB dwarfs)	714	342	339
Step 2. GALFIT & visual inspection			
Bright galaxy candidates	315	106	80
UDG candidates	39	16	1
LSB dwarf candidates	87	35	18
Step 3. Color-magnitude relations			
Final bright galaxies	298	93	56
Final UDGs	34	12	1
Final LSB dwarfs	80	32	10

mag arcsec^{-2} and `FLUX_RADIUS` > 1.0 kpc, and LSB galaxies with `MU_MAX`($F814W$) > 22.5 mag arcsec^{-2} , `FLUX_RADIUS` > 1.0 kpc, and `B_IMAGE/A_IMAGE` > 0.3. We set the minimum effective radii (`FLUX_RADIUS`) to be 1.0 kpc, because we intended to select our galaxy samples with effective radii larger than $2 \times$ FWHM (~ 0.90 kpc). We also set the minimum value of the axis ratio (`B_IMAGE/A_IMAGE`) to be 0.3 in order to exclude gravitational lenses and elongated artifacts. As a result of all these processes, the numbers of selected bright galaxies are 334, 115, and 84 in the central field, the parallel field, and the XDF. The numbers of selected LSB galaxies are 714, 342, and 339 in each field.

Then, we utilized GALFIT to estimate the surface brightness and effective radii of the selected galaxies more precisely. We made input images of each galaxy trimmed with a size of $4\farcs5 \times 4\farcs5$ in order to estimate background values locally. This could minimize the effect of diffuse light from bright galaxies in background estimation. The PSF convolution size is set to be about $5\farcs4$, which is sufficient to give the PSF effect to the entire area of the input images. Other GALFIT configurations and masking methods are similar to those of Lee et al. (2017). Most galaxies were fitted by a single Sérsic law, and nucleated galaxies were fitted with their central nuclei masked.

We divided the sample of LSB galaxies into "UDGs" and "LSB dwarfs". We used the selection criteria adopted in van der Burg et al. (2016) and Lee et al. (2017): $\langle\mu\rangle_{\rm e,abs}(r')^{*} > 23.8$ mag arcsec^{-2} and $R_{\rm eff,c}{}^{\ddagger} > 1.5$ kpc for UDGs, and $\langle\mu\rangle_{\rm e,abs}(r') > 23.8$ mag arcsec^{-2} and $R_{\rm eff,c}= 1.0 - 1.5$ kpc for LSB dwarfs. In this study, these criteria are used for comparison of the Abell 370 UDGs and the UDGs found in the local universe. In addition, we selected LSB dwarfs as smaller counterparts of UDGs. We checked whether UDGs and LSB dwarfs have consistent properties in the result section. $\langle\mu\rangle_{\rm e,abs}(r')$ is the SDSS r'-band absolute mean surface brightness at the effective radii, and $R_{\rm eff,c}$ is the circularized effective radii. We transformed the $F814W$ magnitudes to SDSS r' system using simple stellar population (SSP) models derived from GALAXEV (Bruzual & Charlot 2003). We adopted an age of 12 Gyr, the Chabrier initial mass

---

[*] $\langle\mu\rangle_{\rm e,abs}(r')= \langle\mu\rangle_{\rm e}(r') - 10 \times \log(1+z) - E(z) - K(z)$ at the redshift of $z = 0.375$

[‡] $R_{\rm eff,c} = R_{\rm eff} \times \sqrt{b/a}$ for the adopted distance scale of 4.984 kpc arcsec^{-1}

function (Chabrier 2003), and $[Z/Z_{\odot}] = -0.7$ ($Z = 0.004$) for obtaining SSP models.

Finally, we performed visual inspection of all selected galaxies to get rid of artifacts, tidal structures, gravitational lenses, and blended sources. If some galaxies show unreasonable GALFIT results or residuals due to interfering light from neighboring galaxies or saturated stars, we redid manual masking and GALFIT configurations until we obtained reasonable solutions. The selected galaxies are represented in the selection diagram of the circularized effective radii vs. the SDSS r'-band absolute mean surface brightness at the effective radii, as plotted in **Figure 2.3**, and their census is summarized in “Step 2” of **Table 2.3**. Examples of selected UDGs and LSB dwarfs are displayed in **Figure 2.2**. There are 315, 106, and 80 bright galaxies in the central field, the parallel field, and the XDF. For UDGs, there are 39, 16, and 1 UDGs in each field. For LSB dwarfs, there are 87, 35, and 18 sources in each field. These initial samples are used to select the final samples in **Section 2.3.1**.

2.2.3 Artificial Galaxy Tests

We carried out artificial galaxy tests for the HFF $F814W$ images of the central field, the parallel field, and the XDF (the HUDF09 and the HUDF12) to compute the detection limits and the completeness as a function of clustercentric radius. Utilizing *artdata/gallist* task in IRAF, we generated a total of 120,000 mock galaxies with uniform distributions of $F814W$ magnitude, size, and spatial number density in each field. We set 800 bins of $F814W$ magnitude and effective radii: the magnitude bins are from 20 mag to 30 mag with an interval of 0.25 mag, and the effective radii bins are from 0.75 kpc to 8.22 kpc with a linear interval of 0.37 kpc. There are 150 mock galaxies in each magnitude-size bin. The axis ratios of mock galaxies are set to follow a Gaussian distribution with a mean value of $\langle b/a \rangle = 0.75$, which is the mean value of the axis ratios of Coma LSB galaxies (Yagi et al. 2016).

Figure 2.4 shows the results of artificial galaxy tests. The 50% surface brightness limit, which is about 27 mag arcsec^{-2} in the absolute SDSS r' magnitude, is similar in all the three fields. However, it appears that the central field of Abell 370 has slightly lower

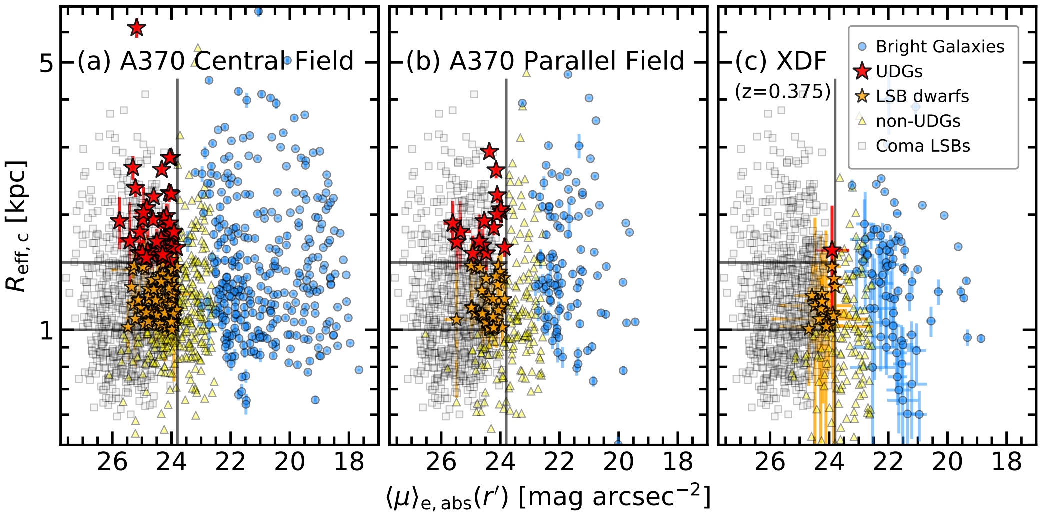

Figure 2.3. Selection diagrams with absolute mean surface brightness ($\langle\mu\rangle_{\rm e,abs}(r')$) in x-axis and circularized effective radii ($R_{\rm eff,c}$) in y-axis. Each panel includes all galaxies in the Abell 370 central field (a), the parallel field (b), and the XDF (c). Blue circles show bright galaxies selected with $\mu_0(F814W) < 22.5$ mag arcsec^{-2} and $R_{\rm eff,c} > 1.0$ kpc. Red and orange stars denote UDG candidates ($\langle\mu\rangle_{\rm e,abs}(r') > 23.8$ mag arcsec^{-2} and $R_{\rm eff,c} > 1.5$ kpc) and initial LSB dwarf candidates ($\langle\mu\rangle_{\rm e,abs}(r') > 23.8$ mag arcsec^{-2} and $R_{\rm eff,c} = 1.0 - 1.5$ kpc) selected with visual inspection. Yellow triangles named "non-UDGs" do not satisfy any selection criteria of the surface brightness and size. Gray squares are LSB galaxies ($R_{\rm eff} \gtrsim 0.7$ kpc) discovered in the Coma cluster (Yagi et al. 2016).

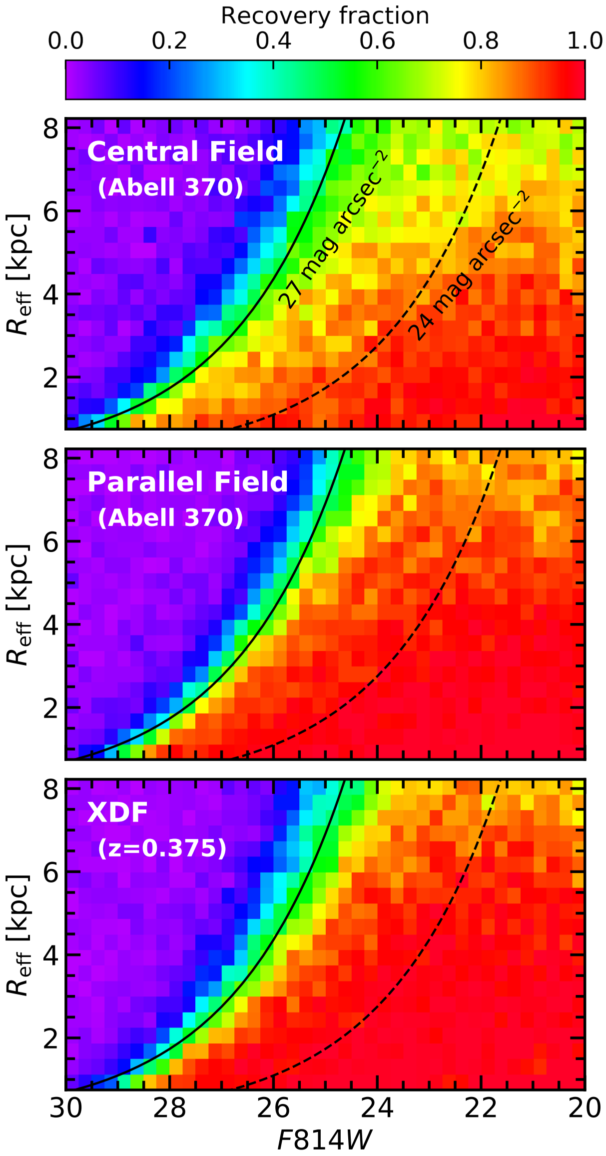

Figure 2.4. Integrated $F814W$ magnitudes of mock galaxies versus their half-light radii showing the recovery fractions from the artificial galaxy tests of the Abell 370 central field (upper panel), the parallel field (middle panel), and the XDF (the HUDF09 and the HUDF12) (lower panel). Color scale bar at the top denotes the recovery fraction. Black dashed line represents $\langle\mu\rangle_{\mathrm{e,abs}}(r') = 24$ mag arcsec^{-2}, which is close to the selection criteria for UDGs and LSB dwarfs. Black solid line denotes $\langle\mu\rangle_{\mathrm{e,abs}}(r') = 27$ mag arcsec^{-2} line, which approximates to the 50% completeness limits of the two Abell 370 fields and the XDF.

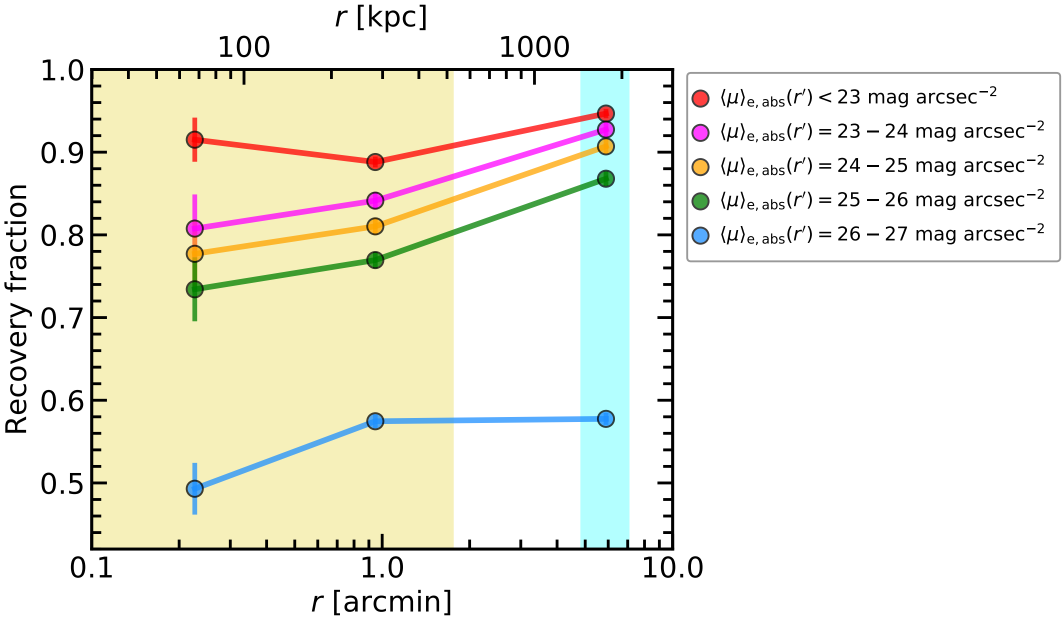

Figure 2.5. Recovery fractions obtained from artificial galaxy tests as a function of clustercentric distance. Shaded regions in yellow and cyan are the Abell 370 central field and the parallel field. Red, magenta, orange, green, and blue filled circles are for the mock galaxies with $\langle\mu\rangle_{\rm e,abs}(r') < 23$ mag arcsec^{-2}, $\langle\mu\rangle_{\rm e,abs}(r') = 23-24$ mag arcsec^{-2}, $\langle\mu\rangle_{\rm e,abs}(r') = 24-25$ mag arcsec^{-2}, $\langle\mu\rangle_{\rm e,abs}(r') = 25-26$ mag arcsec^{-2}, and $\langle\mu\rangle_{\rm e,abs}(r') = 26-27$ mag arcsec^{-2}.

completeness values for detecting LSB galaxies than the parallel field and the XDF. **Figure 2.5** displays the calculated radial completeness as a function of clustercentric distance. All the magnitude bins show lower completeness values at the Abell 370 central field than the parallel field. This is because of diffuse light and a high number density of bright galaxies in the cluster central field. These completeness values in each radial bin are applied to compute the RDPs of galaxies in **Section 2.3.4**.

2.3 Results

2.3.1 CMDs of the Galaxies

Final Sample Selection

Figure 2.6 shows the CMDs of the initially selected galaxies (**Section 2.2.2**) in the central field of Abell 370 (the left panel), its parallel field (the middle panel), and the XDF assumed to be at the same redshift of Abell 370 (the right panel). The most remarkable feature in this figure is the red sequence of galaxies in the central field. We set a boundary of the red sequence as shown by yellow shaded regions in the figure. There are a small number of galaxies redder than the boundary of the red sequence in each field. These galaxies are considered to be background galaxies. We removed these background galaxies from the initial sample, and produced the final sample of galaxies.

As a result, we identified 298, 93, and 56 bright galaxies in the three fields, 34, 12, and 1 UDGs in each field, and 80, 32, and 10 LSB dwarfs in the final sample. These numbers are summarized in “Step 3” of **Table 2.3**. In total, we detect 46 UDGs and 112 LSB dwarfs in the central and parallel field of Abell 370. Janssens et al. (2019) found 65 UDGs in both fields of Abell 370, which is 19 larger than the number in this study. The reason for this difference is not clear. It is noted that our study excluded 9 UDG candidates which are much redder than the red sequence, while it is not clear whether Janssens et al. (2019) applied this selection criterion. For the XDF, the numbers of bright galaxies (56), UDGs (1), and LSB dwarfs (10) are useful to estimate the contribution of background galaxies in the central and parallel fields.

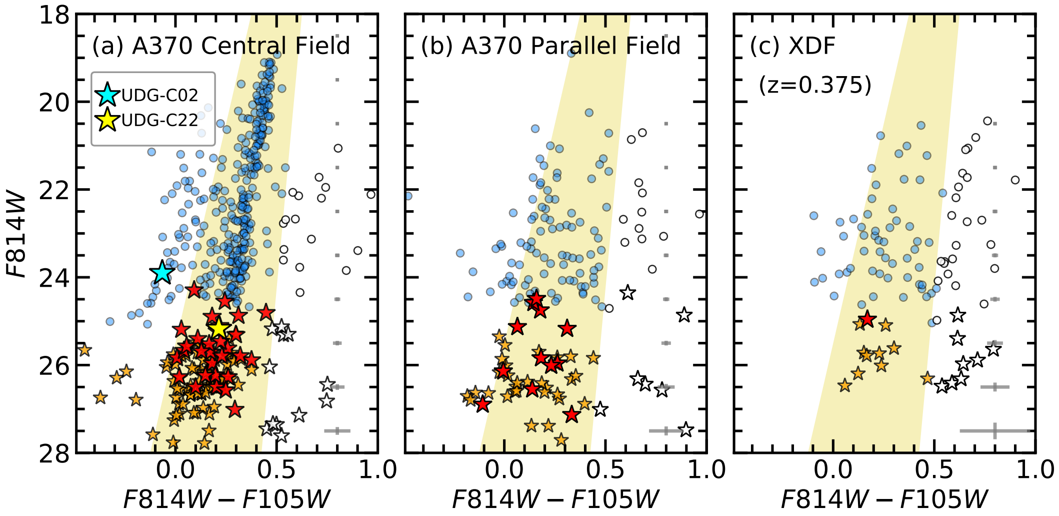

Figure 2.6. Color-magnitude diagrams (CMDs) of galaxies in the Abell 370 central field (a), the parallel field (b), and the XDF (c). Symbols are the same as **Figure 2.3**. Gray error bars on the right side of each panel indicate the mean errors of colors and magnitudes for given magnitudes. Yellow shaded regions denote the red sequence of galaxies in the cluster central field. White open symbols mark galaxies excluded from our final samples, because they are redder than the red sequence. Cyan star (UDG-C02) denotes the bluest UDG ($F814W - F105W = -0.07$), and yellow star (UDG-C22) is the largest UDG ($R_{\mathrm{eff,c}} = 6.16$ kpc) in our UDG sample.

UDGs detected in the central and parallel fields are mostly real members of Abell 370, because the corresponding number of UDGs in the background field is only one. For the UDGs and LSB dwarfs in the central and parallel fields, we provide the catalogs of their photometric properties ($F814W$ magnitudes, $F814W - F105W$ colors, effective radii $R_{\rm eff,c}$, effective surface brightness $\langle\mu\rangle_{\rm e,abs}(r')$, Sérsic indices n, and axis ratios b/a) in **Tables A.1, A.2, A.3** and **A.4**.

CMDs of Abell 370

In **Figure 2.6**, most UDGs in the central and parallel fields of Abell 370 are located at the faint end of the red sequence. Most LSB dwarfs also have colors similar to those of UDGs, but a small number of them show bluer colors. This indicates that most UDGs and LSB dwarfs are made up of an old stellar population, except for a few blue LSB galaxies.

We marked two unusual UDGs in the CMD of the central field. First, UDG-C02 (cyan star) is the bluest UDG of our sample ($F814W - F105W = -0.07 \pm 0.01$). The blue color indicates that this UDG is mainly composed of young stars. This is in strong contrast to the fact that most of cluster UDGs are located in the red sequence. Thus, this provides a rare sample of a blue UDG in a massive galaxy cluster. It is noted that a few blue and irregular UDGs were discovered in various environments (Lee et al. 2017; Román & Trujillo 2017b; Trujillo et al. 2017), but they are much fainter than UDG-C02 with $M_{r'} = -16.8$. Second, UDG-C22 (yellow star) is the largest UDG of our UDG sample with $R_{\rm eff,c} = 6.16 \pm 0.36$ kpc and $\langle\mu\rangle_{\rm e,abs}(r') = 25.18 \pm 0.08$ mag arcsec^{-2}. This UDG is significantly larger than the other UDGs in Abell 370 which have $R_{\rm eff,c} = 1.5 - 3.0$ kpc ($\langle R_{\rm eff,c}\rangle = 2.0$ kpc). This UDG is located right at the red sequence. UDG-C22 is one of the largest UDGs among the known UDGs including Coma DF17 ($R_{\rm eff} = 4.4$ kpc), Coma DF44 ($R_{\rm eff} = 4.6$ kpc), and a few Virgo UDGs ($R_{\rm eff} = 2.9 - 9.7$ kpc) (Mihos et al. 2015).

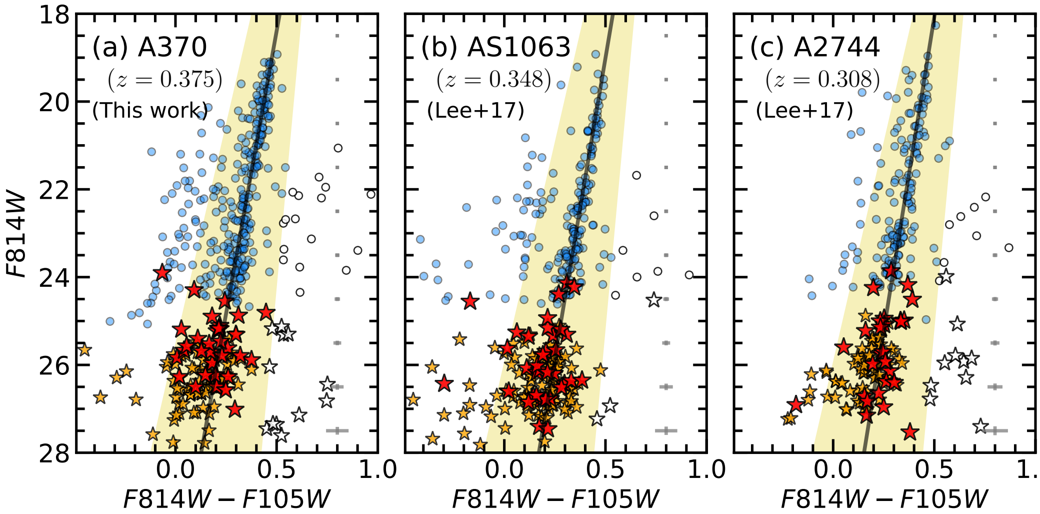

Figure 2.7. CMDs of galaxies in three HFF clusters: Abell 370 ($z = 0.375$), Abell S1063 ($z = 0.348$), and Abell 2744 ($z = 0.308$). Symbols are the same as **Figure 2.3**. Data for Abell S1063 and Abell 2744 are from Lee et al. (2017). Black solid lines denote linear fitting lines of the red sequences derived from median colors and magnitudes of galaxies brighter than $F814W < 23.5$ mag.

A Comparison of Abell 370 with Abell S1063 and Abell 2744

In **Figure 2.7**, we display the CMDs of the central fields of Abell 370 (this work) and two other HFF clusters (Abell S1063 and Abell 2744) in Lee et al. (2017). All these three HFF clusters show a prominent feature of the red sequence. The linear fits of the sequence denoted by the black solid lines show a well-defined red sequence of each cluster. The number of galaxies bluer than the red sequence in Abell 370 is larger than those in Abell S1063 and Abell 2744. This implies that there are more galaxies in transition from blue star-forming galaxies to red quiescent galaxies in Abell 370 compared to the other two HFF clusters.

In **Figure 2.8**, we display the color distributions of each galaxy population in the central fields of the three HFF clusters. For the x-axis, we calculate the color differences from the red sequences ($\Delta(F814W - F105W)$) of the three HFF clusters. The upper

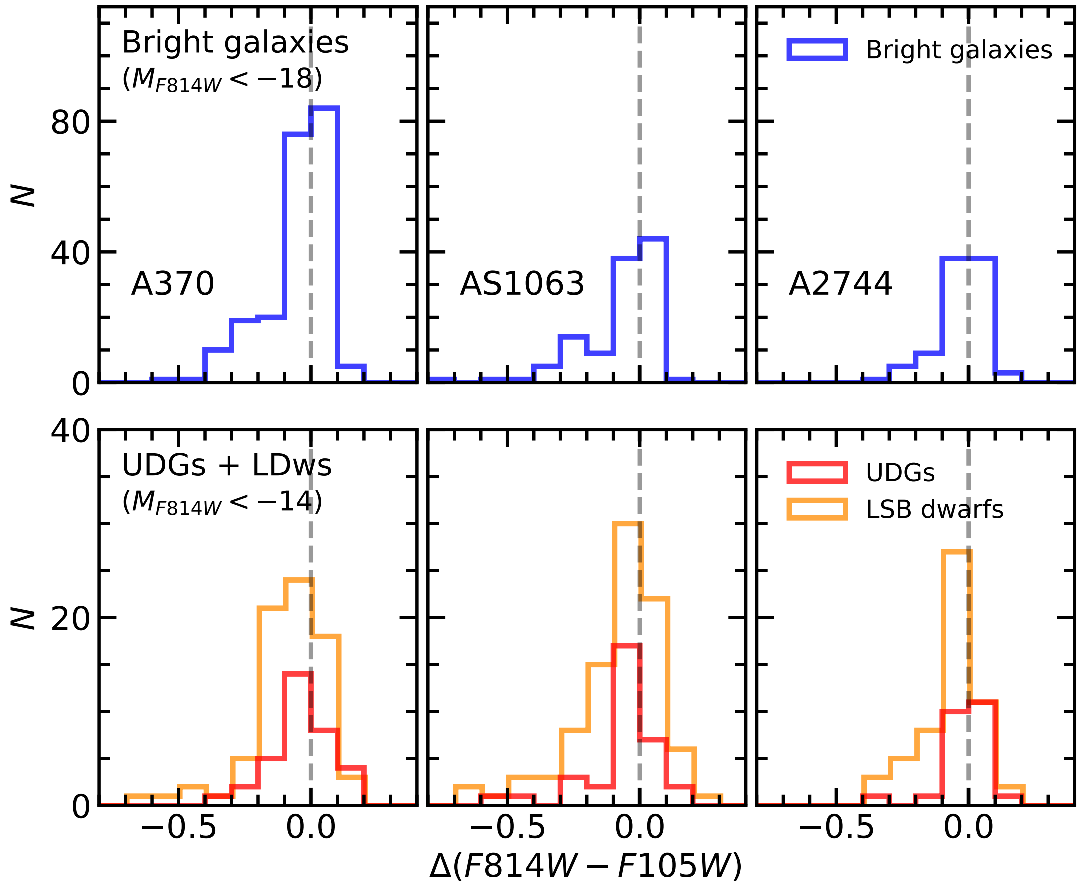

Figure 2.8. Histograms of color differences from the red sequences of the three HFF clusters (See **Figure 2.7**). Gray dashed lines denote the red sequence. The upper panels show the color distributions of bright galaxies (blue histograms), and the lower panels show those of UDGs (red histograms) and LSB dwarfs (yellow histograms). We select each galaxy population with the same absolute magnitude criteria: bright galaxies with $M_{F814W} < -18.0$ mag and LSB galaxies (UDGs and LSB dwarfs) with $-18.0 < M_{F814W} < -14.0$ mag.

panels show the color difference histograms of bright galaxies from the linear fits of the red sequences, and the lower panels show those of UDGs and LSB dwarfs. The linear fits denoted by solid lines in **Figure 2.7** show the narrow red sequence very well. The red sequence is plotted as gray dashed lines in **Figure 2.8**. Overall, the three galaxy populations are dominantly located in the red sequence. Bright galaxies show a bimodal color distribution with a large number of red galaxies and a small number of star-forming blue galaxies. In the lower panels, LSB dwarfs seem to have a higher blue fraction ($f_{\rm blue}$) than UDGs. Using blue galaxies with $\Delta(F814W - F105W) < -0.1$, we obtained $f_{\rm blue} = 0.34 \pm 0.04$ (76/223) for LSB dwarfs and $f_{\rm blue} = 0.19 \pm 0.05$ (17/91) for UDGs in the three HFF clusters. Using blue galaxies with $\Delta(F814W - F105W) < -0.2$, we obtained $f_{\rm blue} = 0.14 \pm 0.03$ (31/223) for LSB dwarfs and $f_{\rm blue} = 0.10 \pm 0.03$ (9/91) for UDGs. This indicates that UDGs could be older and more quiescent in their star formation than LSB dwarfs. However, there are a small number of blue UDGs in each galaxy cluster, implying that star formation is not quenched in all UDGs.

2.3.2 CCDs of the Galaxies

In **Figure 2.9**, we display the de-reddened CCDs ($(F606W - F814W)_0$ vs. $(F814W - F160W)_0$) of the galaxies in Abell 370 as well as those in Abell S1063 and Abell 2744. We adopted the foreground extinctions of each filter as listed in Shipley et al. (2018). We plot the number density contours of the bright galaxies in the red sequence, the UDGs, and the LSB dwarfs in these CCDs. Then, we overlay the simple stellar population (SSP) models from GALAXEV. In order to construct the SSP models, we adopt the following options: spectral templates from Bruzual & Charlot (2003), instantaneous burst star formation history (SFH), no dust, and the Chabrier initial mass function (Chabrier 2003). We set the range of ages of 0.1, 1, 3, and 9 Gyr at the redshifts of the three HFF clusters. We set the range of metallicities with $[Z/Z_\odot] = -1.7, -0.7, 0.0$ (solar), and $+0.4$.

The upper panels of **Figure 2.9** show the de-reddened CCDs of bright red sequence galaxies, UDGs, and LSB dwarfs in Abell 370. In this figure, the UDGs and the LSB

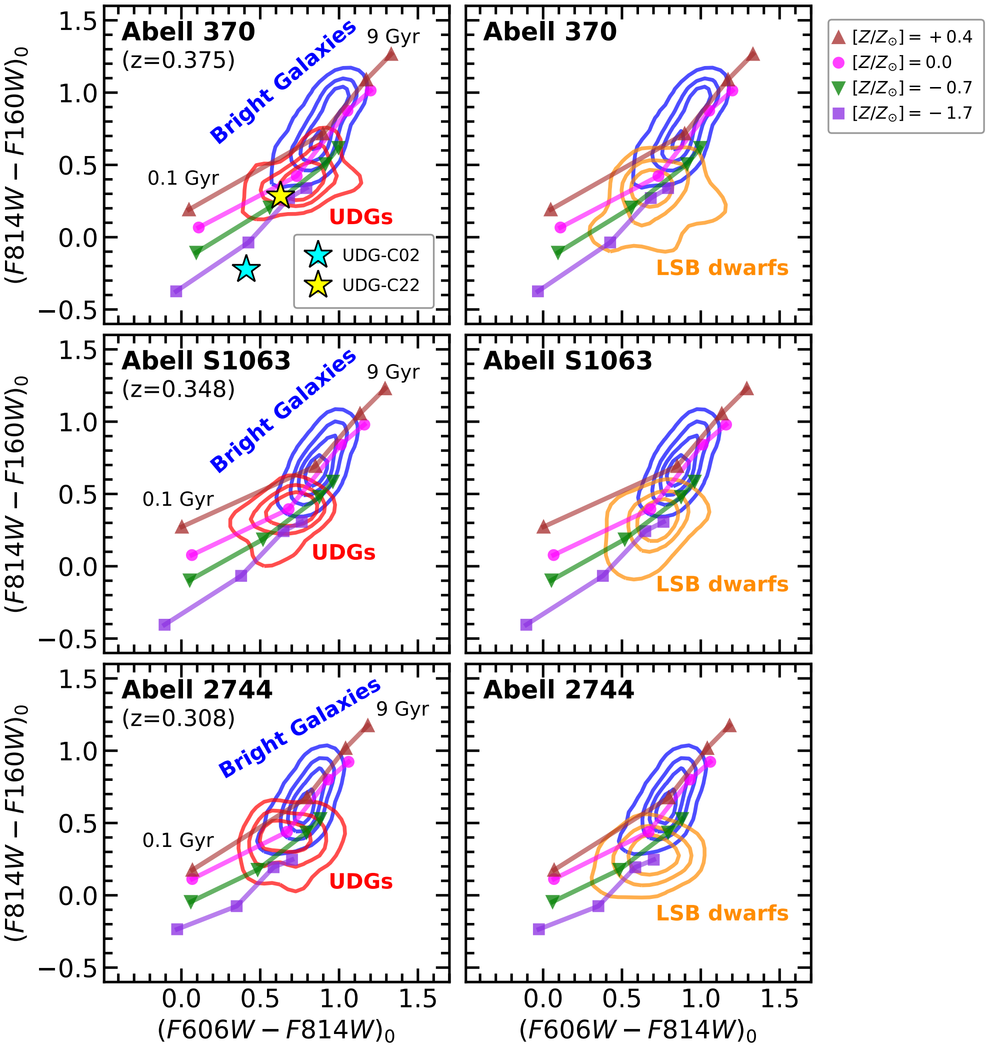

Figure 2.9. Color-color diagrams (CCDs) of bright galaxies, UDGs, and LSB dwarfs in the three HFF clusters. The left panels show the 2D color distributions of bright galaxies (blue contours) and UDGs (red contours) in each cluster. The right panels show the 2D color distributions of bright galaxies and LSB dwarfs (yellow contours). The SSP models have ages of 0.1, 1, 3, and 9 Gyr at the redshifts of the clusters and metallicities with $[Z/Z_\odot] = -1.7$ (purple squares), -0.7 (green upside-down triangles), 0.0 (magenta circles), and +0.4 (brown triangles). In the top left panel, we mark UDG-C02 (cyan star) and UDG-C22 (yellow star).

Table 2.4. Peak Values of the De-reddened Colors of Each Galaxy Population

Cluster	Galaxy population	$(F606W - F814W)_0$	$(F814W - F160W)_0$
Abell 370	Bright galaxies	$0.88^{+0.01}_{-0.01}$	$0.59^{+0.31}_{-0.01}$
	UDGs	$0.79^{+0.05}_{-0.06}$	$0.39^{+0.02}_{-0.04}$
	LSB dwarfs	$0.65^{+0.08}_{-0.02}$	$0.32^{+0.04}_{-0.03}$
Abell S1063	Bright galaxies	$0.86^{+0.01}_{-0.01}$	$0.65^{+0.03}_{-0.03}$
	UDGs	$0.75^{+0.01}_{-0.11}$	$0.39^{+0.03}_{-0.02}$
	LSB dwarfs	$0.72^{+0.01}_{-0.09}$	$0.33^{+0.03}_{-0.05}$
Abell 2744	Bright galaxies	$0.78^{+0.01}_{-0.01}$	$0.56^{+0.09}_{-0.03}$
	UDGs	$0.74^{+0.01}_{-0.19}$	$0.39^{+0.04}_{-0.03}$
	LSB dwarfs	$0.69^{+0.03}_{-0.10}$	$0.21^{+0.14}_{-0.01}$

Note.

In this table, we obtained 1σ (68.3%) error values from bootstrap resampling.

dwarfs show a similar range of colors. For Abell 370, the peak values of the color distribution of the UDGs ($(F606W-F814W)_0 = 0.79$ and $(F814W-F160W)_0 = 0.39$) and the LSB dwarfs ($(F606W-F814W)_0 = 0.65$ and $(F814W-F160W)_0 = 0.32$) are bluer than those of the bright red sequence galaxies ($(F606W-F814W)_0 = 0.88$ and $(F814W-F160W)_0 = 0.59$), as listed in **Table 2.4**. These color ranges of the UDGs and the LSB dwarfs are consistent with the old-age SSP models for low metallicity ($[Z/Z_\odot] \lesssim -0.7$). On the other hand, the colors of bright red sequence galaxies are better matched with the SSP models with higher metallicity ($[Z/Z_\odot] \gtrsim 0.0$). These trends of Abell 370 are similarly seen in the other HFF clusters, Abell S1063 and Abell 2744.

In the upper left panel of this figure, we mark UDG-C02 (the bluest UDG) and UDG-C22 (the largest UDG) of Abell 370. UDG-C02 seems to have an age younger than the other UDGs by a few Gyr. This implies that UDG-C02 includes recently formed stars. In contrast, UDG-C22 shows red colors close to the mean values of the UDGs. This means that UDG-C22 is made of old stars, which is similar to most UDGs in Abell

370. These SSP models presume oversimplied SFHs and dust contents of galaxies, but they are still useful to compare the relative difference of ages and metallicities between bright galaxies and LSB galaxies.

2.3.3 Structural Parameters of the UDGs

We estimate the structural parameters of the galaxies in Abell 370 such as Sérsic indices (n), and axis ratios (b/a) using GALFIT. We compare these structural parameters of Abell 370 UDGs with those of the known UDGs in the Coma cluster. The Coma cluster is known to host a large number of LSB galaxies (Yagi et al. 2016), so that it serves as a very useful reference. We select 193 Coma UDGs out of the whole sample of Coma LSBs given by Yagi et al. (2016), using the same size criteria as used in this work ($R_{\rm eff,c} > 1.5$ kpc).

Figure 2.10 shows the comparison of the structural parameters of Abell 370 UDGs with Coma UDGs. The upper panels of **Figure 2.10** compare the Sérsic indices n of UDGs in the two clusters. Overall, the Sérsic indices of UDGs in the two clusters have similar distributions with $\langle n \rangle \lesssim 1$. These results are consistent with those of UDGs and dwarf galaxies in other clusters such as Fornax and Abell 168 ($\langle n \rangle \sim 0.7$) (Muñoz et al. 2015; Román & Trujillo 2017a). In Lee et al. (2017), the mean values of the Sérsic indices of UDGs in Abell S1063 and Abell 2744 are also $\langle n \rangle \simeq 1.0$. UDGs with $n > 2$ are rare in these galaxy clusters. Note that these Sérsic indices were obtained by masking the central region of UDGs with the nuclei. This indicates that most cluster UDGs have exponential light profiles regardless of their host cluster.

The lower panels of **Figure 2.10** describe the distribution of axis ratios b/a of UDGs in the two clusters. In the Coma cluster, there are no UDGs with $b/a < 0.3$, although Yagi et al. (2016) did not use any selection criterion of $b/a > 0.3$. The axis ratios of UDGs in these two clusters also have consistent distributions with the mean values of $\langle b/a \rangle \sim 0.7$. These mean values are similar to those of UDGs in Abell S1063 ($\langle b/a \rangle = 0.66$) and Abell 2744 ($\langle b/a \rangle = 0.68$). This means the morphology of cluster UDGs is closer to round shapes rather than to elongated shapes.

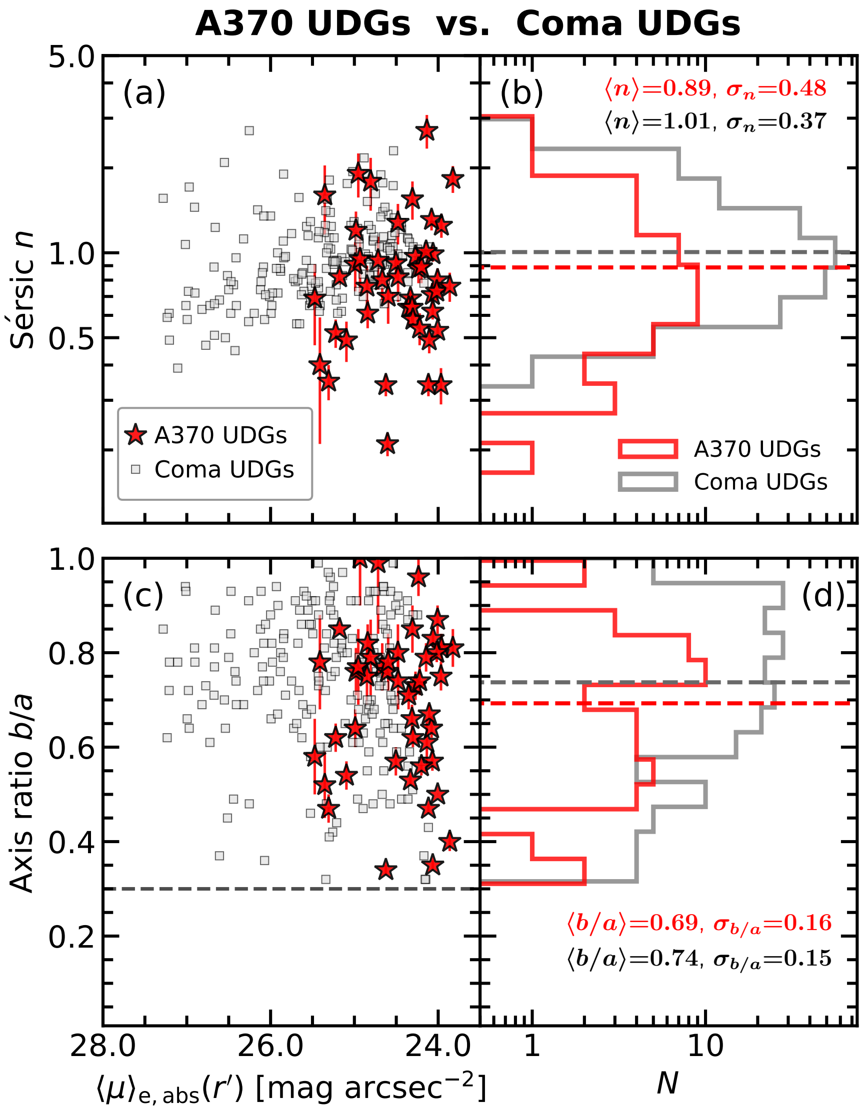

Figure 2.10. Comparison of structural parameters for UDGs in Abell 370 (red stars) and the Coma cluster (gray squares). The upper panels plot Sérsic indices n of Abell 370 UDGs and Coma UDGs as a function of $\langle\mu\rangle_{\rm e,abs}(r')$ (a) and the corresponding histograms (b). The lower panels plot their axis ratios as a function of $\langle\mu\rangle_{\rm e,abs}(r')$ (c) and the histograms (d). The mean and standard deviation values are marked in the right panels. In the lower left panel, gray dashed line denotes our selection criteria of axis ratios with $b/a > 0.3$.

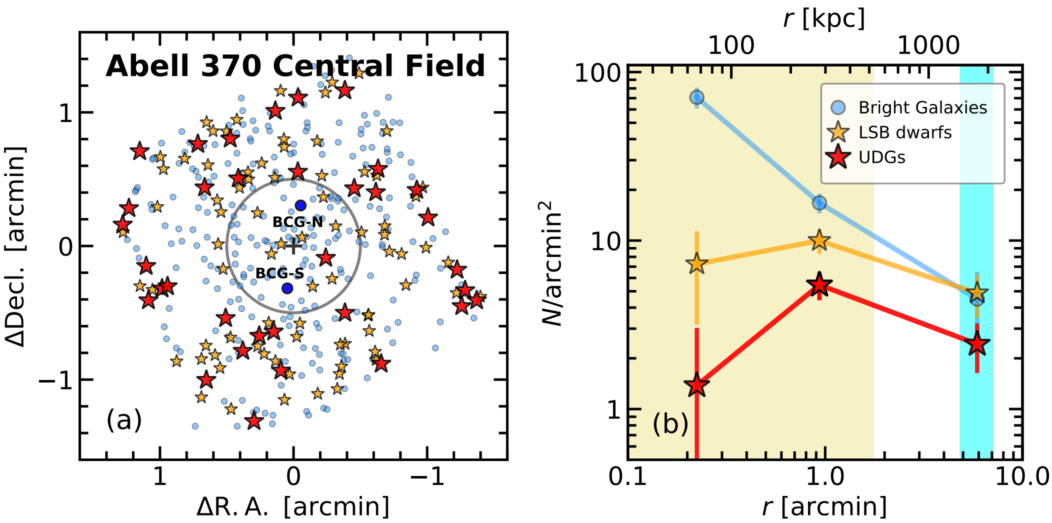

Figure 2.11. (a) Spatial distribution of galaxies in the central field of Abell 370. Symbols of galaxies are the same as in **Figure 2.3**, but here we plot only bright red sequence galaxies. Black crossmark denotes the center of Abell 370, and two large blue circles denote BCG-N and BCG-S. Gray circle with radius of $0\farcm5$ ($\sim$150 kpc) represents the boundary we used to divide the cluster central field. (b) Radial number density profiles (RDPs) of galaxies in the Abell 370 cluster. Blue circles, yellow stars, and red stars are the RDPs of the bright galaxies, LSB dwarfs, and UDGs. Yellow and cyan shaded regions represent the cluster central field and the parallel field.

2.3.4 Spatial Distribution and RDPs of the UDGs

In the left panel of **Figure 2.11**, we plot the spatial distributions of bright galaxies in the red sequence, UDGs, and LSB dwarfs in the central field of Abell 370. The center of the Abell 370 cluster is set to be at the middle point between BCG-N and BCG-S (R.A. (2000)$=2^{\rm h}39^{\rm m}52\fs94$, Decl.(2000)$=-1^\circ34'37\farcs0$), as adopted by Lagattuta et al. (2017). We divide this field into two radial bins based on the clustercentric radius of $0\farcm5$ ($\sim$ 150 kpc) (the gray circle). Bright galaxies seem to be more centrally concentrated in the inner region ($r < 0\farcm5$) than LSB galaxies. It is noted that only one UDG is found in the inner region ($r < 0\farcm5$), while most UDGs are seen in the outer region ($r > 0\farcm5$).

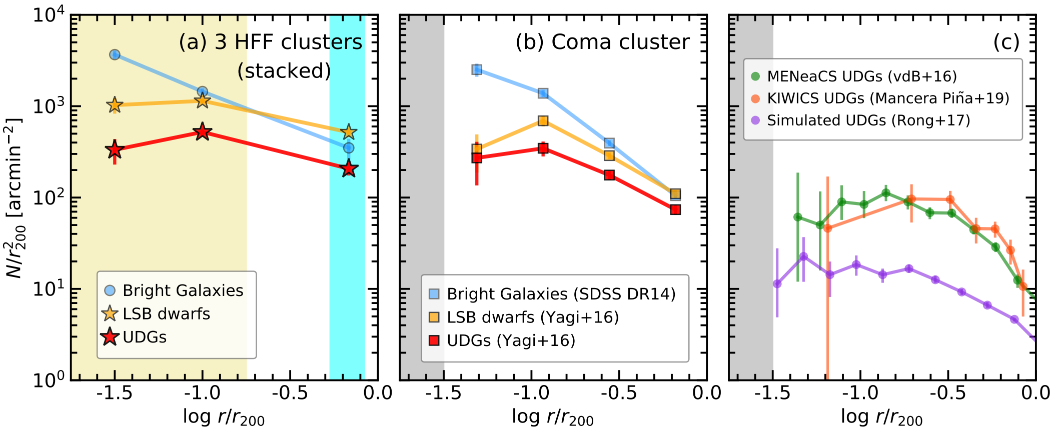

Figure 2.12. RDPs of cluster galaxies from observation and simulation results. (a) The stacked number density profiles for three HFF clusters (Abell 370, Abell S1063, and Abell 2744). Three galaxy populations are indicated: bright galaxies (blue circles), LSB dwarfs (yellow stars), and UDGs (red stars). (b) Same as (a), but for the Coma cluster. The bright galaxy samples (blue squares) are taken from SDSS DR14 (see texts for details). UDGs and LSB dwarfs are selected from Yagi et al. (2016) with the same selection criteria as used in this work. (c) The RDPs of UDGs in eight MENeaCS clusters (van der Burg et al. 2016) (green circles), eight KIWICS clusters (Mancera Piña et al. 2019) (orange circles), and simulated clusters (Rong et al. 2017) (purple circles).

We derive the RDPs of the bright red sequence galaxies, UDGs, and LSB dwarfs, using the data from the central field and the parallel field. We estimate their background number density using the data for the XDF, and subtract them from the results of Abell 370. We correct the resulting number density profiles using the completeness values derived from artificial galaxy tests (as described in **Section 2.2.3** and **Figure 2.5**).

The right panel of **Figure 2.11** shows the RDPs for Abell 370. The RDP of the bright red sequence galaxies shows a clear central concentration. In contrast, the central concentration of the UDGs and LSB dwarfs is much weaker than that of the bright red sequence galaxies. It is noted that the RDPs of the UDGs and LSB dwarfs show a drop or flattening in the innermost bin ($r < 0\overset{\prime}{.}5$), while that of the bright red sequence galaxies keeps increasing as clustercentric distances decrease.

These features of RDPs for Abell 370 are similar to those of Abell S1063 and Abell 2744 (see Figure 7 in Lee et al. (2017)). However, the numbers of UDGs and LSB dwarfs in the inner region of each cluster are too small to obtain statistically meaningful conclusions. Therefore, we stack the RDPs of the three HFF clusters: Abell 370 (this work), Abell S1063, and Abell 2744. Before stacking we normalized the clustercentric distance with respect to the virial radius (r_{200}) of each cluster: $r_{200} = 8\overset{\prime}{.}52$ for Abell 370, $8\overset{\prime}{.}64$ for Abell S1063, and $9\overset{\prime}{.}16$ for Abell 2744. In **Figure 2.12** (left panel), we display the stacked RDPs of the bright red sequence galaxies, UDGs, and LSB dwarfs. Again, the stacked RDPs of the UDGs and LSB dwarfs show a flattening or drop in the inner region ($\log r/r_{200} < -1.0$), in contrast to the RDP of the bright red sequence galaxies which rises as clustercentric distances decrease. Janssens et al. (2019) also found similar central depletion or flattening of the RDPs of UDGs in all the six HFF clusters.

In addition, we compare the RDPs of the HFF clusters with those of other clusters. The middle panel of **Figure 2.12** shows the RDPs of the three galaxy populations in the Coma cluster. We select bright red sequence galaxies in the Coma cluster from SDSS DR14 (Abolfathi et al. 2018) by using the following criteria: magnitude ($r' < 18$ mag), color ($(g' - r')$ color for the red sequence of the Coma cluster), clustercentric distance ($r_{\rm cl} < r_{200} = 97\overset{\prime}{.}92$ (Kubo et al. 2007)), and radial velocity ($v_r(\text{Coma}) - v_r(r_{\rm cl}) < v_r <$

$v_r(\mathrm{Coma}) + v_r(r_{\mathrm{cl}})$), where $v_r(\mathrm{Coma})$ is the systematic velocity of the Coma cluster ($v_r(\mathrm{Coma}) = 6925.0$ km s^{-1} in Struble & Rood (1999)) and $v_r(r_{\mathrm{cl}}) = (GM_{200}r_{\mathrm{cl}}^{-1})^{1/2}$. We divide Coma LSB galaxies in Yagi et al. (2016) into UDGs ($R_{\mathrm{eff,c}} > 1.5$ kpc) and LSB dwarfs ($R_{\mathrm{eff,c}} = 1.0 - 1.5$ kpc), applying the same criteria as in this study. The RDPs of the bright red sequence galaxies, UDGs, and LSBs in Coma show very similar trends to those of the three HFF clusters.

In the right panel, we display the RDPs of UDGs in nearby low-mass clusters in the literature: 8 MENeaCS clusters ($z = 0.044 - 0.063$) with median virial mass of $M_{200} = 5.55 \times 10^{14}\ M_\odot$ in van der Burg et al. (2016), and 8 KIWICS clusters ($z = 0.02 - 0.03$) with median virial mass of $M_{200} = 3.35 \times 10^{13}\ M_\odot$ in Mancera Piña et al. (2019). The RDPs of UDGs in these low-mass clusters show a trend consistent with those of the HFF clusters and the Coma cluster.

In the same figure, we overlay the RDP of the UDGs in simulated clusters given by Rong et al. (2017). These simulated clusters also have low masses of $M_{200} = 10^{13} - 10^{14}\ M_\odot$. The RDP of the simulated UDGs similarly shows a flattening in the inner region. The flattening or dropping features of the RDPs of UDGs appear to be universal in galaxy clusters regardless of virial masses or redshifts of their host clusters. From the comparison of the RDPs of UDGs from low to high mass clusters and in simulated clusters, we conclude that the RDPs of UDGs (as well as LSB dwarfs) show a flattening in the inner region of the clusters. We discuss this aspect further in **Section 2.4.1**.

2.3.5 The Abundance of UDGs and the Virial Masses of Host Systems

The abundance (total number) of galaxies inside the virial radii (r_{200}) of their host systems can help us understand the correlation between the number of galaxies and their environments. The abundance of UDGs ($N(\mathrm{UDG})$) is known to have a power-law relation with the virial masses (M_{200}) of their host systems: $N(\mathrm{UDG}) \propto M_{200}^{\alpha}$ (van der Burg et al. 2016; Lee et al. 2017; Román & Trujillo 2017b; van der Burg et al. 2017; Mancera Piña et al. 2018). In this relation, the α-value is a key parameter to determine how efficiently galaxies are formed and survive in their environments. If $\alpha < 1$, galaxies

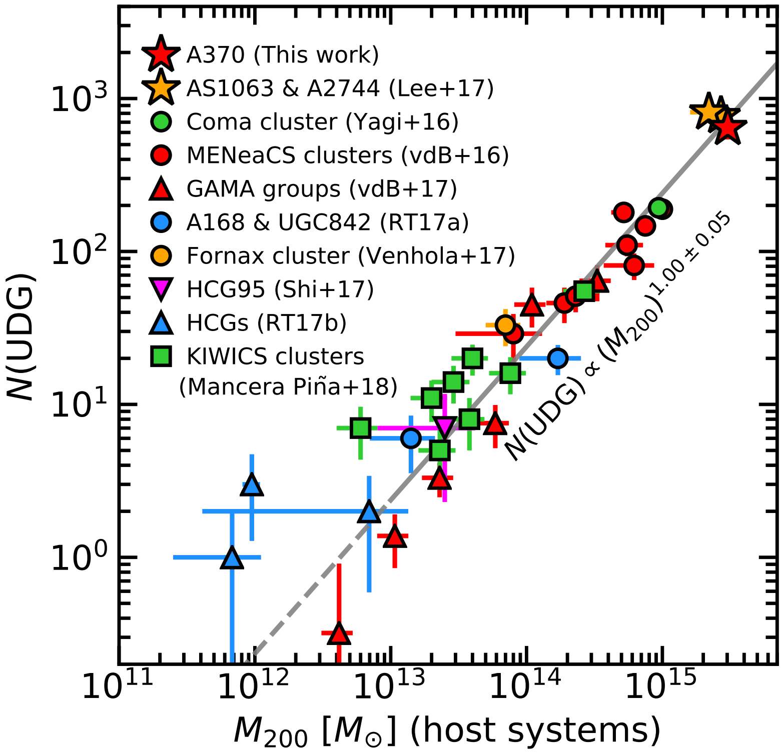

Figure 2.13. The UDG abundance versus virial mass of their host system (M_{200}) for Abell 370 (red star) in comparison with other systems in the previous studies. Gray solid line shows a power-law fit for the UDGs in the host systems with $M_{200} > 10^{13}$ $M_{\odot}$: $\log N(\mathrm{UDG}) = (1.00 \pm 0.05) \times \log M_{200} + (-12.67 \pm 0.74)$.

in low density environments have relatively higher number densities per mass of their host systems. This implies that the galaxies are preferentially formed and survive in fields or galaxy groups rather than in massive galaxy clusters. In contrast, $\alpha > 1$ means that galaxies are formed more efficiently or survive longer in high density environments. $\alpha = 1$ means that the number of galaxies simply depends on the masses of their host systems. These galaxies do not strongly depend on environmental effects.

Table 2.5. The Abundance of UDGs in Galaxy Groups and Clusters

Host system	$\log M_{200}/M_\odot$ (host system)	$N(\mathrm{UDG})^a$	References
A370	15.48	644 ± 104	This study
AS1063	15.43	770 ± 114	Lee et al. (2017)
A2744	15.34	814 ± 122	Lee et al. (2017)
Coma	14.97	193 ± 14	Yagi et al. (2016)
A85	15.00	189 ± 21	van der Burg et al. (2016)
A119	14.88	147 ± 17	van der Burg et al. (2016)
A133	14.74	110 ± 17	van der Burg et al. (2016)
A780	14.79	81 ± 16	van der Burg et al. (2016)
A1781	13.90	29 ± 10	van der Burg et al. (2016)
A1795	14.72	180 ± 20	van der Burg et al. (2016)
A1991	14.28	46 ± 12	van der Burg et al. (2016)
MKW3S	14.36	51 ± 11	van der Burg et al. (2016)
GAMA groups (bin 1)	12.62	0.3 ± 0.6	van der Burg et al. (2017)
GAMA groups (bin 2)	13.03	1.4 ± 0.5	van der Burg et al. (2017)
GAMA groups (bin 3)	13.36	3.3 ± 0.8	van der Burg et al. (2017)
GAMA groups (bin 4)	13.77	7.5 ± 2.4	van der Burg et al. (2017)
GAMA groups (bin 5)	14.04	45 ± 13	van der Burg et al. (2017)
GAMA groups (bin 6)	14.52	64 ± 17	van der Burg et al. (2017)
A168	14.23	20 ± 4.5	Román & Trujillo (2017a)
UGC842	13.15	6.0 ± 2.5	Román & Trujillo (2017a)
Fornax	13.85	33 ± 9	Venhola et al. (2017)
HCG95	13.40	7.0 ± 4.7	Shi et al. (2017)
HCG07	11.98	3.0 ± 1.7	Román & Trujillo (2017b)
HCG25	11.83	1.0 ± 1.0	Román & Trujillo (2017b)
HCG98	12.84	2.0 ± 1.4	Román & Trujillo (2017b)
RXCJ1204.4+0154	13.46	14 ± 3.9	Mancera Piña et al. (2018)
A779	13.69	20 ± 4.6	Mancera Piña et al. (2018)
RXCJ1223.1+1037	13.30	11 ± 3.3	Mancera Piña et al. (2018)
MKW4S	13.36	5.0 ± 2.2	Mancera Piña et al. (2018)

Table 2.5 (cont'd)

Host system	log $M_{200}/M_\odot$ (host system)	N(UDG)[a]	References
RXCJ1714.3+4341	12.78	7.0 ± 2.7	Mancera Piña et al. (2018)
A2634	14.42	55 ± 7.8	Mancera Piña et al. (2018)
A1177	13.58	8.0 ± 3.0	Mancera Piña et al. (2018)
A1314	13.88	16 ± 4.4	Mancera Piña et al. (2018)

Note.

[a] UDGs were selected using the same selection criteria as in this study.

We estimate the abundance of UDGs (N(UDG)) within the virial radius of Abell 370, by integrating the RDPs from the inner region to the outskirts at its virial radius. We obtained a value of N(UDG)$= 644 \pm 104$. This value is consistent, within the error, with the value given by Janssens et al. (2019), N(UDG)$= 711^{+213}_{-210}$ for Abell 370.

We counted UDGs in other host systems from previous studies, using the same criterion as used in this study. **Table 2.5** provides a list of N(UDG) and M_{200} of the host systems. In **Figure 2.13**, we show the relation between N(UDG) and M_{200} of Abell 370, in comparison with those of UDGs in other host systems in the literature: massive galaxy clusters (Yagi et al. 2016; Lee et al. 2017), low-mass clusters (van der Burg et al. 2016; Román & Trujillo 2017a; Venhola et al. 2017; Mancera Piña et al. 2019), galaxy groups (van der Burg et al. 2017), and compact galaxy groups (Román & Trujillo 2017b; Shi et al. 2017).

In the figure, N(UDG) and M_{200} show a tight correlation, but the scatter increases at low-mass host systems. This scatter is significantly large for the mass of $M_{200} < 10^{13}$ $M_\odot$, because low-mass host systems have only a small number of UDG. Fitting the data for $M_{200} > 10^{13} M_\odot$, we obtain $\log N(\mathrm{UDG}) = (1.00\pm0.05)\times\log M_{200} + (-12.67\pm0.74)$ with a root mean square (RMS) of 0.19 dex, where the value of α is basically one. Similarly, we derive $\alpha = 0.97 \pm 0.05$ for $M_{200} > 10^{12} M_\odot$. If we use the entire range of the virial mass for fitting, we obtain $\alpha = 0.91 \pm 0.05$. Thus, the α-value is close to one. This indicates that the efficiency of the formation or survival of UDGs is little dependent on their environments.

If we fit the virial mass in terms of UDG abundance for $M_{200} > 10^{13} M_{\odot}$, we obtain log $M_{200} = (1.00 \pm 0.05) \times \log N(\mathrm{UDG}) + (12.63 \pm 0.10)$ with an RMS value of 0.19 dex. This relation can be used to estimate the virial masses of the host systems using the abundance of UDGs.

2.3.6 Dynamical Mass of the UDGs

Dynamical mass of UDGs is a critical parameter to understand the nature of UDGs. Various methods have been applied to estimate dynamical masses of UDGs in the literature. First, direct measurements of velocity dispersions of UDGs with spectroscopy can be used to estimate their virial masses under the assumption that UDGs are pressure-supported systems. For example, Martín-Navarro et al. (2019) obtained $\sigma_v = 56^{+10}_{-10}$ km s$^{-1}, and \mathrm{M}_{200} \sim 5 \times 10^{11}\ M_{\odot}$ for DGSAT-I. Second, the total number of GCs is useful for mass estimation of their hosts. There are well-known relations between the number of GCs (N_{GC}) and halo masses (M_{halo}) (Harris et al. (2017) and references therein). Since this method is easier than spectroscopy, a number of studies applied this method to the sample of Coma UDGs including DF17 ($N_{\mathrm{GC}} = 25 \pm 11$ and $M_{\mathrm{halo}} \sim 9 \times 10^{10}\ M_{\odot}$), DF44 ($N_{\mathrm{GC}} = 76 \pm 18$ and $M_{\mathrm{halo}} \sim 8 \times 10^{11}\ M_{\odot}$), and DFX1 ($N_{\mathrm{GC}} = 63 \pm 17$ and $M_{\mathrm{halo}} \sim 5 \times 10^{11}\ M_{\odot}$) (Beasley & Trujillo 2016; Peng & Lim 2016; van Dokkum et al. 2016, 2017; Amorisco et al. 2018; Lim et al. 2018). Third, HI line widths can be used to estimate the dynamical mass of gas-rich UDGs. Trujillo et al. (2017) measured the HI line width of UGC 2162, a blue isolated gas-rich UDG, to be $W(\mathrm{HI}) = 126$ km s^{-1} and derived a virial mass of $M_{200} \sim 8 \times 10^{10}\ M_{\odot}$. Fourth, weak lensing analysis can be used to estimate virial mass of UDGs. Sifón et al. (2018) used this method and constrained the maximum virial mass range of UDGs in the MENeaCS clusters: $M_{200} < 6.3 \times 10^{11}\ M_{\odot}$ with the 95% confidence level.

In the case of Abell 370 UDGs/LSB dwarfs, none of the above methods can be used. We estimate dynamical masses of UDGs/LSB dwarfs approximately, using the fundamental manifold method based on photometric parameters as suggested by Zaritsky (2017). Zaritsky et al. (2008) suggested a fundamental manifold of galaxies, with which we can derive kinematic terms from their sizes and surface brightness. The kinetic term is defined by $V = \sqrt{\sigma_v^2 + v_{\rm rot}^2/2}$, where σ_v is the velocity dispersion and $v_{\rm rot}$ is the rotation velocity. Zaritsky et al. (2008) used 1,925 galaxies from bright ellipticals ($-22.0 < M_{r'} < -18.5$) to low-mass disk galaxies ($-16.0 < M_{r'} < -13.5$) (Geha et al. 2006; Zaritsky et al. 2006a,b; Pizagno et al. 2007; Simon & Geha 2007; Springob et al. 2007) in order to empirically calibrate the scaling relations. They suggested that the derived relations can be applied to any types of galaxies regardless of their morphology. Zaritsky (2017) applied this method to estimate the kinetic terms of LSB galaxies including UDGs after performing an observational correction (see the equations (1), (2) in Zaritsky (2017)). Then, they estimated the virial masses of the UDGs using these derived kinetic terms. Lee et al. (2017) and Chan et al. (2018) also used this method to estimate dynamical masses of UDGs in massive clusters and simulations. We estimate dynamical masses of UDGs and LSB galaxies in Abell 370, assuming that these galaxies are pressure-supported systems and their halo mass profiles follow the NFW profiles (see the equation (3) in Lee et al. (2017) and the related text).

However, Zaritsky (2017) used only two UDGs with spectroscopic measurements (DF44 and VCC 1287) to check the validity of applying the fundamental manifold method to UDGs. Here we check it again using an increased sample of 13 UDGs/LSB dwarfs which have velocity dispersion measurements: 9 Coma UDGs in Chilingarian et al. (2019), Coma DF44 (van Dokkum et al. 2019), Coma DFX1 (van Dokkum et al. 2017), DGSAT-1 (Martín-Navarro et al. 2019), and VCC 1287 (Beasley et al. 2016). 6 of the 9 Coma UDGs in Chilingarian et al. (2019) have effective radii smaller than 1.5 kpc, so they correspond to LSB dwarfs in this study.

In **Figure 2.14**, we plotted estimated kinetic terms ($V_{\rm est}$) versus observed kinetic terms ($V_{\rm obs}$) for these 13 UDGs/LSB dwarfs (it is an updated version of Fig. 1 in Zaritsky (2017)). For comparison, we plotted also the sample of GCs (McLaughlin & van der Marel 2005), ultra-compact dwarfs (UCDs) (Mieske et al. 2008; Chilingarian

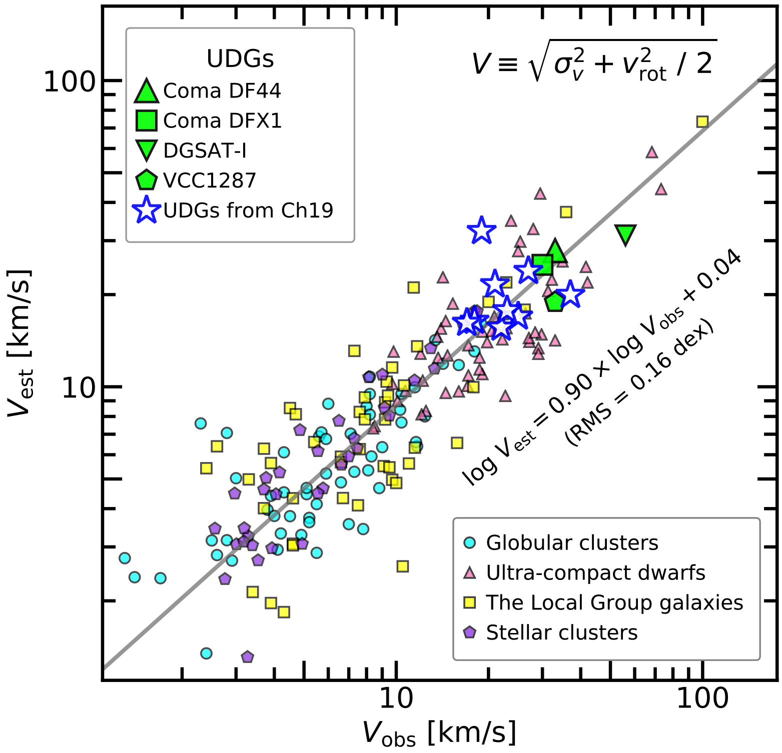

Figure 2.14. Comparison of the kinetic terms ($V \equiv \sqrt{\sigma_v^2 + v_{\mathrm{rot}}^2/2}$, $V = \sigma_v$ for $v_{\mathrm{rot}} = 0$) of passive stellar systems derived from the spectroscopic measurement (V_{obs}, x-axis) and the fundamental manifolds (V_{est}, y-axis). We plot the data of 13 UDGs/LSB dwarfs with spectroscopic measurements of their velocity dispersions: Coma DF44 (van Dokkum et al. 2019), Coma DFX1 (van Dokkum et al. 2017), DGSAT-I (Martín-Navarro et al. 2019), VCC 1287 (Beasley et al. 2016), and 9 Coma UDGs from Chilingarian et al. (2019) (noted as ‘Ch19’ in the figure). For comparison, we added the sample of globular clusters (McLaughlin & van der Marel 2005), ultra-compact dwarfs (UCDs) (Mieske et al. 2008; Chilingarian et al. 2011; Seth et al. 2014; Ahn et al. 2017, 2018; Afanasiev et al. 2018), satellite galaxies in the Local Group (McConnachie 2012), and stellar clusters (Zaritsky et al. 2012, 2013, 2014). The gray solid line shows the power-law fitting result of the relation between V_{obs} and V_{est}: log $V_{\mathrm{est}} = 0.90 \times \log V_{\mathrm{obs}} + 0.04$ with an RMS value of 0.16 dex.

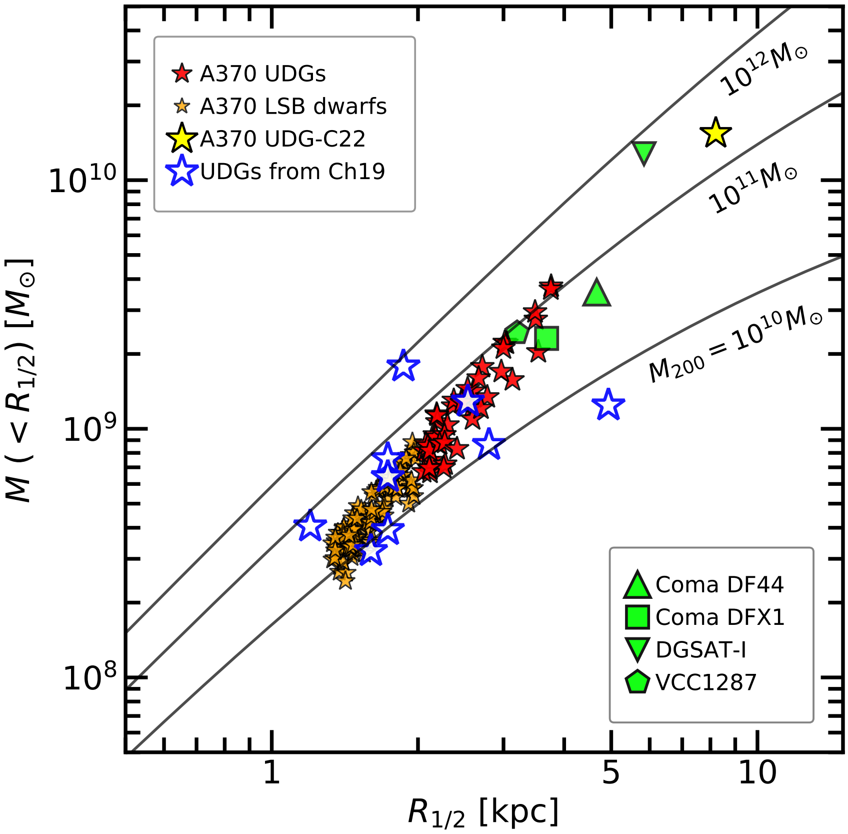

Figure 2.15. Enclosed masses ($M(< R_{1/2})$) vs. 3D half-light radii ($R_{1/2} = 4/3\ R_{\rm eff,c}$) for Abell 370 UDGs (red star symbols) and LSB dwarfs (orange star symbols) in comparison with other galaxies in the literature (green and blue symbols as in **Figure 2.14**). Enclosed masses are derived from the scaling relations in Zaritsky et al. (2008) and Zaritsky (2017). Black solid line curves denote virial masses of M_{200}= 10^{10}, 10^{11}, and 10^{12} $M_\odot$ derived from the NFW mass density profiles. The large cyan star symbol is Abell 370 UDG-C22, the largest one.

et al. 2011; Seth et al. 2014; Ahn et al. 2017; Afanasiev et al. 2018; Ahn et al. 2018), satellite galaxies in the Local Group (McConnachie 2012), and stellar clusters (Zaritsky et al. 2012, 2013, 2014). We assumed $v_{\rm rot} = 0$ except for a few dwarf galaxies in the Local Group and UCDs. This figure shows that the 13 UDGs/LSB dwarfs follow very well the relation of other passive stellar systems. We fit the data for all stellar systems including UDGs/LSB dwarfs with a power law, obtaining $\log V_{\rm est} = 0.90 \times \log V_{\rm obs} + 0.04$ with an RMS value of 0.16 dex. This relation is very similar to the relation for the non-UDG sample given by Zaritsky (2017), $\log V_{\rm est} = 0.88 \times \log V_{\rm obs} + 0.07$. This indicates that the fundamental manifold method can be applied to the UDG/LSB dwarf regime.

Figure 2.15 displays the dynamical mass distributions of UDGs and LSB dwarfs in Abell 370 derived from the fundamental manifold method in this study. We marked UDG-C22, the largest one, by a yellow star symbol. The x-axis is the 3D half-light radius ($R_{1/2} = 4R_{\rm eff,c}/3$), and the y-axis is the enclosed dynamical mass within $R_{1/2}$. The curved solid lines denote the virial masses (M_{200}) of 10^{10}, 10^{11}, and 10^{12} $M_\odot$ derived from the NFW mass profiles. For comparison, we also plotted other known UDGs/LSB dwarfs with spectroscopic measurements in the literature (Beasley et al. 2016; van Dokkum et al. 2016, 2017; Chilingarian et al. 2019; Martín-Navarro et al. 2019) as in **Figure 2.14**.

Several features are noted in **Figure 2.15**. First, the locations of Abell 370 UDGs/LSB dwarfs are overlapped with those of other UDGs with spectroscopic measurements. This implies that the dynamical mass range of Abell 370 UDGs/LSB dwarfs is similar to that of the other UDGs/LSB dwarfs. Second, UDGs have relatively larger enclosed masses than LSB dwarfs. Thus, UDGs are larger and more massive than LSB dwarfs. Third, most UDGs and LSB dwarfs have virial masses with $M_{200} = 10^{10} - 10^{11}$ $M_\odot$. This implies that a majority of UDGs are dwarf-like galaxies. Fourth, a few UDGs in Abell 370 have larger virial masses, $10^{11} < M_{200} < 10^{12}$ $M_\odot$. Among them, UDG-C22, the largest one in Abell 370, has the largest mass. Interestingly DGSAT-I, the largest in the other UDG sample, has a mass similar to that of UDG-C22.

2.3.7 The Size-Luminosity Relation of UDGs and LSB Dwarfs

We display the size-luminosity relation of UDGs and LSB dwarfs of Abell 370 in **Figure 2.16**. For comparison, we also plotted other passive stellar systems: giant ellipticals and bulges in spirals (Bender et al. 1993), Coma LSBs (Yagi et al. 2016), Fornax dwarfs (Muñoz et al. 2015; Ordenes-Briceño et al. 2018), UCDs (Pandya et al. 2016), dwarf galaxies in the Local Group (McConnachie 2012), and GCs in the Milky Way (MW) and M31 (Harris 2010; Peacock et al. 2010). Ultra-faint dwarfs (UFDs, $M_V > -7.7$ mag) in the Local Group are marked by thin diamonds. In the figure, we added the loci of surface brightness for $\langle\mu\rangle_{\rm e,abs}(V) = 20 - 30$ mag arcsec^{-2} with an interval of 2 magnitude.

Figure 2.16 shows following features. First, UDGs/LSB dwarfs in Abell 370 occupy the larger and brighter side of UDGs/LSB dwarfs in Coma, Fornax, and the Local Group. Second, UDGs in Abell 370 are just a larger and brighter version of LSB dwarfs, not showing any clear distinction between the two types. Third, UDGs/LSB dwarfs are obviously separated from the high surface bright objects such as giant elliptical galaxies and spiral bulges, UCDs, and globular clusters.

2.4 Discussion

2.4.1 Implications of RDPs of the UDGs

In **Section 2.3.4**, we find that the RDPs of UDGs show a flattening (or a slight drop) in the inner region of their host systems, while the RDPs of bright red sequence galaxies do not. This can be seen from low-mass clusters to high mass clusters. The RDPs of UDGs and LSB dwarfs in the three HFF clusters also show a similar trend.

Most previous studies interpreted that tidal disruptions of UDGs contributed to their low number densities in the central region. van der Burg et al. (2016) and Lee et al. (2017) suggested that some UDGs were disrupted by the strong gravitational potential near the center of clusters. They noted that most UDGs could be easily disrupted because of their low masses. In addition, Venhola et al. (2017) and Wittmann

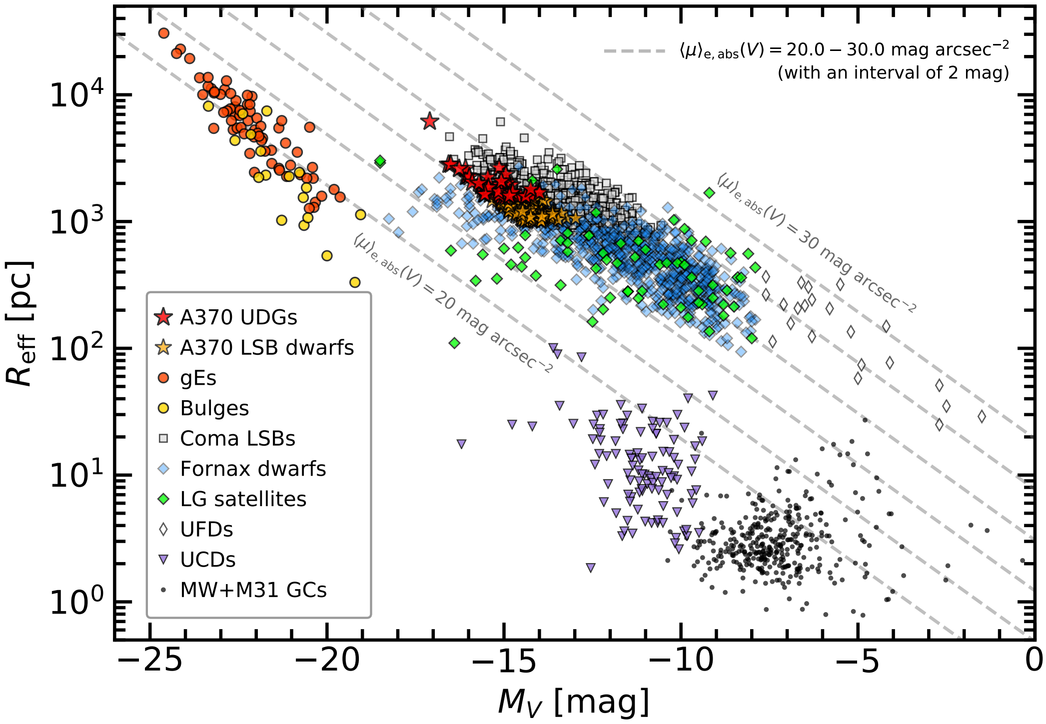

Figure 2.16. The size-luminosity relation diagram for Abell 370 UDGs (red star symbols) and LSB dwarfs (orange star symbols) in comparison with other passive stellar systems: giant ellipticals (gEs) and bulges in spirals (red and yellow circles) (Bender et al. 1993), Coma LSBs (gray squares) (Yagi et al. 2016), Fornax dwarfs (blue diamonds) (Muñoz et al. 2015; Ordenes-Briceño et al. 2018), the Local Group satellites (green diagmonds) (McConnachie 2012), ultra-compact dwarfs (purple upside-down triangles) (Pandya et al. 2016), and GCs in the MW and M31 (black dots) (Harris 2010; Peacock et al. 2010). Ultra-faint dwarfs (UFDs, white diamonds) are selected with $M_V > -7.7$ from the sample of dwarf galaxies. Gray dashed lines denote the surface brightness of $\langle\mu\rangle_{\rm e,abs}(V) = 20$, 22, 24, 26, 28, and 30 mag arcsec^{-2} from left to right.

et al. (2017) also found that the number densities of UDGs in the central region of the Fornax cluster and the Perseus cluster are lower than in the outer region. These studies pointed out that it is difficult for UDGs to survive in the strong tidal interactions of the cluster central regions. Note that the tidal disruption of UDGs means not that UDGs are completely destroyed, but the outskirts of UDGs are stripped away so that the UDGs cannot be diffuse galaxies anymore.

Observationally, tidally disrupted UDGs are frequently found from the local Universe to distant galaxy clusters. UDGs around massive galaxies such as And XIX (near M31) (Collins et al. 2013, 2019), CenA-MM-Dw3 (near NGC 5128) (Crnojević et al. 2016), and Scl-MM-Dw2 (near NGC 253) (Toloba et al. 2016) show tidal features toward their neighboring massive galaxies. In cluster environments, several UDGs in the Virgo cluster (Mihos et al. 2015; Toloba et al. 2018) and the HFF clusters (Lee et al. 2017) also have tidally disrupted features near bright galaxies in the clusters. Thus, our results support the tidal disruption scenario for low number densities of UDGs as well as LSB dwarfs in the central regions of their host systems.

2.4.2 Comparison of the Relation between UDG Abundance and Virial Mass of Their Host Systems

In this study, we find that the relation between UDG abundance and the virial mass of their host systems is described well by a simple power-law relation with an index of $\alpha = 1.00 \pm 0.05$ for $M_{200} > 10^{13}\ M_\odot$, and $\alpha = 0.97 \pm 0.05$ for $M_{200} > 10^{12}\ M_\odot$. If we include two Hickson compact groups (HCGs) with lower mass ($5 \times 10^{11}\ M_\odot < M_{200} < 10^{12}\ M_\odot$), we derive a slightly smaller value, $\alpha = 0.91 \pm 0.05$. It is noted that we selected UDGs in the literature samples using the same selection criteria as used in this study.

We compare our results with those in the previous studies, as shown in **Figure 2.13** in the following. van der Burg et al. (2016) suggested $\alpha = 0.93 \pm 0.16$ from UDGs in eight MENeaCS galaxy clusters at $z = 0.044-0.063$. Later, adding the stacked numbers of UDGs in galaxy groups from KiDS+GAMA fields, van der Burg et al. (2017) derived

$\alpha = 1.11 \pm 0.07$. Lee et al. (2017) added the data for UDGs in two massive clusters (Abell S1063 and Abell 2744) to the previous sample, and obtained $\alpha = 1.05 \pm 0.09$ for the systems with $M_{200} > 10^{13} M_\odot$. Recently, Mancera Piña et al. (2018) suggested $\alpha = 0.96 \pm 0.11$ for $M_{200} = 10^{12} - 5 \times 10^{14}\ M_\odot$, using the samples in 8 clusters from the KIWICS and applying homogeneous selection criteria of UDGs. These values are all close to one, being consistent with the results in this study.

On the other hand, a few studies presented slightly lower values of α. Román & Trujillo (2017b) added UDGs in HCGs ($5 \times 10^{11} M_\odot < M_{200} < 10^{13} M_\odot$) to the sample and derived $\alpha = 0.85 \pm 0.05$. Mancera Piña et al. (2018) also presented $\alpha = 0.77 \pm 0.06$, if they include two Hickson compact groups with lower mass ($10^{11}\ M_\odot < M_{200} < 10^{12}\ M_\odot$). Our value for the sample including lower mass systems, $\alpha = 0.91 \pm 0.05$, is larger than these values. However, it is noted that the upper virial mass limit for the samples in Román & Trujillo (2017b) and Mancera Piña et al. (2018), $M_{200} = 5 \times 10^{14}\ M_\odot$, is much smaller than the value in this study ($M_{200} = 3 \times 10^{15}\ M_\odot$).

2.4.3 The Mixed Formation Scenarios of UDGs

There are three main scenarios proposed to explain the formation of UDGs in the literature: 1) the failed galaxies scenario, 2) the extended dwarf galaxies scenario, and 3) the interaction scenario (Amorisco & Loeb 2016; van Dokkum et al. 2016; Di Cintio et al. 2017; Bennet et al. 2018).

The first scenario is applicable to UDG progenitors undergoing early accretion to galaxy clusters. Yozin & Bekki (2015) used N-body simulation to show how star formation in UDG progenitors could be quenched by ram-pressure stripping in cluster environments. There are two variations of this scenario depending on the range of halo masses: a "failed L^* galaxies" scenario and a "failed dwarf galaxies" scenario. UDGs from "failed L^* galaxies" have comparable halo masses to that of the MW ($M_{200} > 10^{11}\ M_\odot$), whereas "failed dwarf galaxies" have halo masses less than those of the Large Magellanic Cloud ($M_{200} < 10^{11}\ M_\odot$). Observationally, some Coma UDGs like DF44 or DFX1, which have red colors and massive dark matter (DM) halos ($M_{200} > 10^{11}\ M_\odot$), are consistent with the “failed L^* galaxies” scenario (van Dokkum et al. 2016, 2017). On the other hand, less massive UDGs with red colors such as DF17 or VCC 1287 ($M_{200} < 10^{11}\ M_\odot$) can be explained by the “failed dwarf galaxies” scenario (Beasley et al. 2016; Beasley & Trujillo 2016; Peng & Lim 2016).

In the “extended dwarf galaxies” scenario, UDG progenitors could be extended by internal processes. This scenario does not require high density environments or massive DM halos to produce UDGs. Amorisco & Loeb (2016) and Rong et al. (2017) suggested that the high spin parameters of DM halos of UDGs could produce extended dwarf galaxies, and concluded that UDGs are the high-spin tails of normal dwarf galaxies. In contrast, Di Cintio et al. (2017) and Chan et al. (2018) suggested that strong gas outflows from stellar feedback could affect the gravitational potential of the DM halo and eventually extend the stellar content of UDG progenitors. Blue isolated UDGs such as UGC 2162 (Trujillo et al. 2017), LSBG-750 (Greco et al. 2018b), and the UDGs in HCGs (Román & Trujillo 2017b; Spekkens & Karunakaran 2018) have lower virial masses of $M_{\rm vir} \lesssim 10^{11}\ M_\odot$, which can be explained by this scenario. Moreover, Leisman et al. (2017) used HI observations and showed that UDGs in low-density environments tend to have relatively higher spin parameters than normal gas-rich galaxies.

In the third scenario, UDGs are created by tidal interactions with neighboring massive galaxies. This scenario is supported by the presence of UDGs close to massive galaxies. Several studies of UDG morphology provided observational evidence supporting this scenario: CenA-MM-Dw3 (Crnojević et al. 2016), DF4 near NGC 5485 (Merritt et al. 2016), Scl-MM-Dw2 near NGC 253 (Toloba et al. 2016), VLSB-A and VLSB-D in the Virgo cluster (Mihos et al. 2015; Toloba et al. 2018), NGC 2708-Dw1, and NGC 5631-Dw1 (Bennet et al. 2018). Baushev (2018) suggested that UDGs could be also generated via head-on collisions between two gas-rich galaxies which remove a large amount of gas in UDG progenitors.

Recent studies tend to suggest mixed formation scenarios to explain the diversity in the UDG populations in various environments by combining the individual scenarios (Lee et al. 2017; Papastergis et al. 2017; Alabi et al. 2018; Ferré-Mateu et al. 2018; Lim et al. 2018; Pandya et al. 2018). These studies revealed the presence of diverse UDGs through various methods: 1) the total number of GCs in UDGs, 2) optical spectroscopy, 3) SED fitting, and 4) HI observation.

First, the total number of GCs in UDGs has been used as a proxy to estimate the UDG halo mass. van Dokkum et al. (2017) presented that UDGs have, on average, a significantly larger number of GCs (by a factor of ~ 7) than other galaxies with similar luminosity and stellar mass, using HST/ACS data of 16 Coma UDGs. In their work, DF44 and DFX1 in Coma are good examples of UDGs with rich GC populations. This implies that those UDGs are hosted by massive halos like the MW, but they failed to form as many stars as bright galaxies with similar dynamical masses. From this, van Dokkum et al. (2017) concluded that their results support the failed L^* galaxy scenario. However, Amorisco et al. (2018) presented the opposite conclusion, using GCs in 54 Coma LSBs including 18 UDGs ($R_{\rm eff} > 1.5$ kpc). They found that most of Coma UDGs in their sample have dwarf-like halos with $M_{\rm vir} < 10^{11}\ M_\odot$ with the 90% confidence level, and only three UDGs are hosted by massive halos ($M_{\rm vir} > 10^{11}\ M_\odot$). Later, Lim et al. (2018) studied the GC populations of 48 Coma UDGs. They divided their UDG samples into two populations according to their GC specific frequency (S_N): high-S_N UDGs and low-S_N UDGs. They revealed that high-S_N UDGs (27 in total) have $M_{\rm halo} \sim 10^{11}\ M_\odot$ on average, whereas the remaining low-S_N UDGs have significantly lower halo mass ($< 10^{11}\ M_\odot$). This result is intermediate between van Dokkum et al. (2017) and Amorisco et al. (2018) and implies that UDGs have two populations generated by multiple formation routes. Lim et al. (2018) concluded that UDGs have two populations formed by different routes. Likewise, Toloba et al. (2018) applied a similar method to three Virgo UDGs. They suggested that there are two types of UDGs: one is a smooth and DM-dominated system with a massive halo ($M_{200} \sim 10^{12}\ M_\odot$), and the other is a tidally perturbed system with significant rotation and a less massive halo ($M_{200} < 10^{11}\ M_\odot$).

Second, optical spectroscopy has been used to study kinematics and stellar populations of UDGs. Alabi et al. (2018) obtained spectra of Coma UDGs using Keck/DEIMOS and derived the clustercentric radial velocities of the UDGs. They suggested that Coma UDGs are divided into two different types in their velocity phase-space diagram (Fig 9. in their study). One is 'recent infall' UDGs (~ 2 Gyr ago) with high relative line-of-sight velocities and relatively bluer colors, and the other is early accreted 'primordial' UDGs (~ 8 Gyr ago) with low relative line-of-sight velocities and redder colors. Ferré-Mateu et al. (2018) presented the results of stellar population analysis based on the same spectra as used in Alabi et al. (2018). They derived the stellar parameters such as age, metallicity, and SFH, and showed that most UDGs have similar SFH, mass-age, and mass-metallicity relations to those of dwarf galaxies rather than to those of bright galaxies. This supports that most UDGs have a dwarf-like nature. However, a few UDGs like DF07 and DF44 in Coma show a 'primordial' nature with low metallicities, old ages, and early quenching SFHs (Kadowaki et al. 2017; Gu et al. 2018). Chilingarian et al. (2019) derived kinematic and stellar parameters of 9 Coma UDGs/LSB dwarfs, using the MMT/Binospec spectrograph. They suggested that UDGs and LSB dwarfs are of the same population and they have a wide range of age and metallicity due to a diversity of formation scenarios. All these spectroscopic results imply that UDGs have multiple populations originated from different formation processes.

Third, SED fitting is also useful to reveal the multiple nature of UDGs. Applying `prospector` (a fully Bayesian SED fitting package) to optical-NIR SEDs, Pandya et al. (2018) studied two UDGs residing in different environments: VCC 1287 in the Virgo cluster, and DGSAT-I in the field environment. They found that VCC 1287 shows a redder color ($g - i \sim 0.7$), an older age (~ 8 Gyr), a lower metallicity ($[Z/Z_\odot] \sim -1.0$), and a less extended SFH than DGSAT-I. In contrast, DGSAT-I has a bluer color ($V - I \sim 0.3$), a younger age (~ 3 Gyr), a relatively metal-rich SED ($[Z/Z_\odot] \sim -0.6$), and an extended SFH. Although there have been not many studies of SEDs of UDGs, this implies that UDGs have a multiple formation scenario.

Fourth, recent HI observations of UDGs provided evidence of multiple populations of UDGs. Papastergis et al. (2017) presented the HI properties of four isolated UDGs. Three UDGs (DGSAT I, R-127-1, and M161-1) are gas-deficient ($M_{\rm HI}/M_* \lesssim 0.6$) and quiescent galaxies, while one UDG (SdI-2) is a gas-rich ($M_{\rm HI}/M_* > 20$) dwarf galaxy. Considering that isolated UDGs such as UGC 2162 (Trujillo et al. 2017) and SdI-1 (Bellazzini et al. 2017) have high gas fractions ($M_{\rm HI}/M_* > 10$), UDGs in the low density environment can be distinguished as two types according to their gas fractions.

In a similar context, our study of UDGs in massive clusters shows diverse types of UDGs. A majority of UDGs are dwarf galaxies in terms of thier RDPs and dynamical masses. Considering most UDGs have red colors and no star-forming features, they can be failed dwarf galaxies. However, UDG-C22 in Abell 370 is so large ($R_{\rm eff,c} = 6.16$ kpc) and massive ($M_{200} > 10^{11}\ M_\odot$) that it can be considered as an example of a primodal failed L^* galaxy. Interestingly, UDG-C02 in Abell 370 can be an extended dwarf galaxy due to its remarkably blue color. There are also a few tidally interacting UDGs. This diversity of UDGs is consistently shown in the UDGs in other HFF clusters. Thus, we conclude that UDGs in massive HFF clusters can be explained by multiple formation scenarios.

2.5 Summary and Conclusion

We used the HST archival images of Abell 370, a massive galaxy cluster in the HFF, to find and study UDGs and LSB dwarfs. We investigated the properties of the UDGs and LSB dwarfs in Abell 370 in comparison with those in two other massive HFF clusters, Abell 2744 and Abell S1063. The main results are summarized as follows.

1. In the central and parallel HST fields of Abell 370, we found a total of 46 UDGs and 112 LSB dwarfs. There are 34 UDGs and 80 LSB dwarfs in the central field, and 12 UDGs and 32 LSB dwarfs in the parallel field.

2. The CMDs of Abell 370 show that most UDGs are located in the red sequence of the cluster. This means that most UDGs are quiescent galaxies with no star formation. However, one UDG, UDG-C02, shows a much bluer color ($F814W - F105W = -0.07$), implying that this galaxy hosts a very young stellar population.

3. Abell 370 UDGs mostly have exponential light profiles and round shapes. Their structural parameters (Sérsic indices (n) and axis ratios (b/a)) are, on average, similar to those of UDGs in the Coma cluster and other HFF clusters.

4. The RDPs of the galaxies in Abell 370 show a similar feature to those of Abell S1063 and Abell 2744. The mean RDPs of UDGs and bright galaxies in the combined sample of the three HFF clusters show a significant discrepancy in the central region of the clusters. The profiles of UDGs and LSB dwarfs show a flattening as the clustercentric distance decreases, while that of bright galaxies shows a continuous increase. This implies that UDGs and LSB dwarfs in the central regions of the clusters might have been tidally disrupted.

5. We estimate the abundance of UDGs in Abell 370 from the RDP, obtaining $N(\mathrm{UDG}) = 644 \pm 104$. This value is similar to those of Abell S1063 and Abell 2744. Combining our results on UDGs with those in the literature, we investigated the relation between the number of UDGs and the virial mass of their host systems. This relation for the host mass range of $M_{200} > 10^{13}\ M_{\odot}$ is fitted very well by a power law with an index value close to one: $N(\mathrm{UDG}) \propto M_{200}^{1.00\pm0.05}$. This indicates that UDGs are formed with similar efficiency regardless of the virial mass of their host systems.

6. Adding updated data of 13 UDG/LSB dwarfs, we derived a relation in the fundamental manifold method, $\log V_{\mathrm{est}} = 0.90 \times \log V_{\mathrm{obs}} + 0.04$ with an RMS value of 0.16 dex, which is similar to Zaritsky (2017)'s. This shows that the fundamental manifold method can be applied to the UDG/LSB dwarf regime.

7. We estimate the virial masses (M_{200}) of galaxies in Abell 370 with the fundamental manifold method, assuming that these galaxies are pressure-supported systems. Most UDGs have masses of $M_{200} = 10^{10} - 10^{11}\ M_{\odot}$. However, a few UDGs such as UDG-C22 are more massive than $M_{200} > 10^{11}\ M_{\odot}$. This implies that most UDGs are hosted in dwarf halos, but a few of them are hosted in MW-like halos.

8. UDGs and LSB dwarf galaxies do not show any significant distinction in their properties (size, luminosity, color, age, RDPs, and dynamical mass). This implies that UDGs are just a larger and more massive version of LSB dwarfs.

9. In conclusion, our results support multiple formation scenarios of UDGs as suggested in the previous studies: Most UDGs have dwarf-like origins, while a few UDGs can be failed L^* galaxies.

Chapter 3

A GMOS/IFU Study of Five Jellyfish Galaxies in the MACS Clusters and Abell 2744

(This chapter has been submitted to *The Astrophysical Journal.*)

3.1 Introduction

Environmental effects play an important role in galaxy transformation in high-density environments. Most gas-rich galaxies in galaxy groups or clusters evolve by losing their gas content due to various mechanisms: galaxy mergers (Toomre & Toomre 1972), ram-pressure stripping (RPS; Gunn & Gott 1972), galaxy harassment (Moore et al. 1996), and starvation (Larson et al. 1980). These external processes remove the gas ingredients for star formation from galaxies and transform late-type galaxies into early-type galaxies in dense environments.

RPS is the interaction between the intracluster medium (ICM) and the interstellar medium (ISM) in galaxies. It has been known as the most efficient mechanism of gas removal from galaxies in cluster environments. When a galaxy moves through the intergalactic space that is filled with hot and diffuse gas, ram pressure applies a force to the gas component in the galaxy towards the opposite direction to the galaxy motion. RPS eventually quenches star formation activity by sweeping out the gas content in galaxies. Since diffuse ICM with X-ray emission is frequently observed in galaxy clusters, RPS seems to significantly contribute to the passive evolution of cluster galaxies (Dressler 1980).

However, some late-type galaxies undergoing RPS are not quiescent but rather show local star-forming regions. Several late-type galaxies under the effect of RPS in Virgo and Coma were found to have a large number of blue and UV-emitting knots or "spur clusters" throughout their disks (Hester et al. 2010; Smith et al. 2010; Yoshida et al. 2012; Lee & Jang 2016). Interestingly, a post-merger elliptical galaxy in Abell 2670 was revealed to be undergoing RPS and exhibits compact star-forming blobs outside the main body of the galaxy (Sheen et al. 2017). Cluster galaxies with remarkable RPS features like one-sided tails and bright star-forming knots are often called "jellyfish galaxies" (Bekki 2009; Chung et al. 2009). The presence of young stellar systems in jellyfish galaxies implies that RPS can locally boost the star formation activity in gas-rich galaxies before removing gas completely. Thus, jellyfish galaxies are very interesting and useful targets to investigate the relationship between star formation activity and RPS.

Recently, observational studies on jellyfish galaxies have utilized integral field spectroscopy (IFS). IFS observations are able to provide both spatial and spectral information, so they are optimal to investigate various physical properties of jellyfish galaxies. For instance, the GAs Stripping Phenomena (GASP) survey observed a large sample of jellyfish galaxies in nearby galaxy clusters using the Multi Unit Spectroscopic Explorer (MUSE) on the Very Large Telescope (VLT) (Poggianti et al. 2017). Studies from the GASP survey found that star-forming knots in jellyfish galaxies are formed in situ with stellar ages younger than 10 Myr, are dynamically cold ($\sigma_{v,\mathrm{gas}} < 40$ km s^{-1}), and are mostly excited by photoionization (Bellazzini et al. 2017; Bellhouse et al. 2019). They obtained a mean star formation rate (SFR) of $\sim 1.8\ M_\odot$ yr^{-1} in the disks and ~ 0.13 $M_\odot$ yr^{-1} in the tails of the jellyfish galaxies (Poggianti et al. 2019; Gullieuszik et al.

Table 3.1. Examples of Jellyfish Galaxies (JFGs) Observed at $z > 0.1$

Reference	JFGs (Host System)	Redshift	Observing Instruments
Owen et al. (2006)	C153 (A2125)	0.253	*HST*/WFPC2, KPNO 4m, Gemini/GMOS longslit VLA, *Chandra*
Cortese et al. (2007)	131124−012040 (A1689) 235144−260358 (A2667)	0.187 0.227	*HST*/WFPC2, *HST*/ACS, VLT/ISAAC, *Spitzer*/IRAC, *Spitzer*/MIPS, VLA, VLT/VIMOS, Keck/LRIS
Owers et al. (2012)	4 JFGs (A2744)	0.29 – 0.31	*HST*/ACS AAT/AAOmega
Ebeling et al. (2014)	6 JFGs (37 MACS clusters)	0.3 – 0.5	*HST*/ACS
McPartland et al. (2016)	16 JFGs (63 MACS clusters)	0.3 – 0.5	*HST*/ACS, Keck/DEIMOS
Ebeling et al. (2017)	MACSJ0553-JFG1 (MACSJ0553−3342)	0.442	*HST*/ACS, *HST*/WFC3, Keck/LRIS, Keck/DEIMOS, *Chandra*, GMRT
Boselli et al. (2019)	ID 345 and ID 473 (CGr32)	0.73	**VLT/MUSE**[a], *XMM-Newton*, *HST*/ACS, Subaru/Suprime-Cam
Kalita & Ebeling (2019)	A1758N_JFG1 (A1758N)	0.273	**Keck/KCWI**[a], Keck/DEIMOS, *HST*/ACS, *Chandra*
Román et al. (2019)	70 JFGs (A901/2)	0.165	GTC/OSIRIS, *HST*/ACS, *XMM-Newton*
Durret et al. (2021)	81 JFGs (MACS0717.5+3745) 97 JFGs (22 clusters)	0.546 0.2 – 0.9	*HST*/ACS
Moretti et al. (2022)	13 JFGs (A2744 and A370)	0.3 – 0.4	*HST*/ACS, **VLT/MUSE**[a]

Note.

[a] Integral field spectroscopic (IFS) observations.

2020). As a result, the GASP survey has successfully provided a comprehensive view of the star formation activity of jellyfish galaxies in the local universe ($z < 0.1$).

However, most IFS studies have been limited to jellyfish galaxies in low-mass clusters ($\sigma_{v,\mathrm{cl}} \lesssim 1000$ km s^{-1}) in the local universe ($z < 0.1$). Since massive clusters are rare in the nearby universe, jellyfish galaxies in massive clusters have been mostly found at intermediate redshift ($z > 0.1$) and studied by deep images from the Hubble Space Telescope (*HST*). **Table 3.1** lists the jellyfish galaxies that have been mainly observed at $z > 0.1$ so far. All the observations used *HST* optical images because such high-resolution images show the dramatic features of jellyfish galaxies very well. Owen et al. (2006) and Cortese et al. (2007) found three disturbed jellyfish galaxies with blue star-forming knots in the multi-band *HST* optical images and radio images: C153 (Abell 2125; $z = 0.253$), 131124-012040 (Abell 1689; $z = 0.187$), and 235144-260358 (Abell 2667; $z = 0.227$). Owers et al. (2012) studied four jellyfish galaxies with highly asymmetric tails and very bright star-forming knots in the merging cluster Abell 2744, using the *HST* optical images and AAOmega spectra. Ebeling et al. (2014) and McPartland et al. (2016) performed a systematic search of jellyfish galaxies using the *HST* images of the Massive Cluster Survey (MACS; Ebeling et al. 2001, 2010) and provided a catalog of 16 jellyfish galaxies in the MACS cluster samples at $z > 0.3$ ($\langle M_{\mathrm{tot}} \rangle \sim 1.3 \times 10^{15}\ M_{\odot}$). Román et al. (2019) presented the characteristics of 70 jellyfish galaxies using the OMEGA-OSIRIS survey of a multi-cluster system A901/2. Similarly, Durret et al. (2021) found a total of 178 jellyfish galaxy candidates in 23 clusters from the DAFT/FADA and CLASH surveys.

Among the studies described by **Table 3.1**, the IFS observations of jellyfish galaxies at $z > 0.1$ have been rare except for the three cases. Boselli et al. (2019) detected two massive star-forming galaxies with long gaseous tails in the COSMOS cluster CGr32 ($z = 0.73$) using VLT/MUSE. Kalita & Ebeling (2019) studied an extreme jellyfish galaxy, A1758N-JFG1, in the colliding galaxy cluster Abell 1758N ($z = 0.28$) with the Keck Cosmic Web Imager (KCWI). These two studies focused on the resolved kinematics of jellyfish galaxies based on the [O II]$\lambda\lambda 3727, 3729$ doublet emission line because their IFS data did not cover the Hα emission line. Recently, Moretti et al. (2022) presented the properties of 13 jellyfish galaxies in the inner regions of Abell 2744 ($z = 0.306$) and Abell 370 ($z = 0.375$) using the emission lines of Hα and [O II]$\lambda\lambda 3727, 3729$. Their study suggested that the [O II]/Hα ratio in the tails of their sample is much higher than those of local jellyfish galaxies, which implies that the stripped gas might have low gas density or interact with the ICM.

In this chapter, we investigate the physical properties of jellyfish galaxies in massive clusters using the integral field unit (IFU) instrument on the Gemini Multi-Object Spectrograph (GMOS). The 8-m Gemini telescope is suitable for observing jellyfish galaxies at intermediate redshift in terms of its light-gathering power and field-of-view (FOV). We carry out emission line analyses of the GMOS/IFU data of jellyfish galaxies, which includes the Hα line. We then compare our results with those from the GASP survey.

This chapter is organized as follows. In **Section 3.2.1**, we explain our target selection and their properties. Then, we describe our GMOS/IFU observations and data reduction in **Section 3.2.2**, and we describe the multi-wavelength archival images in **Section 3.2.3**. We explain our analysis of the GMOS/IFU data cube to derive the physical quantities in **Section 3.3**. In **Section 3.4**, we illustrate the maps of the gas ionization mechanisms, the kinematics, the star formation activity, and the dynamical states for our targets. In **Section 3.5**, we discuss the star formation activity of jellyfish galaxies when combining our sample and the GASP sample using phase-space diagrams. We present our conclusions and summarize the results in **Section 3.6**. We adopt the cosmological parameters with $H_0 = 70$ km s^{-1} Mpc^{-1}, $\Omega_M = 0.3$, and $\Omega_\Lambda = 0.7$.

3.2 Sample and Data

3.2.1 Jellyfish Galaxy Sample

We selected five jellyfish galaxies in the MACS clusters and Abell 2744 for our IFS observations: MACSJ0916-JFG1 ($z = 0.330$; McPartland et al. 2016), MACSJ1752-

Table 3.2. Properties of the Host Clusters of the Jellyfish Galaxies

Cluster Name	R.A.	Decl.	z	Angular scale	$E(B-V)$	$\sigma_{v,\mathrm{cl}}$	M_{200}	r_{200}	L_X
	(J2000)	(J2000)		(kpc arcsec^{-1})	(mag)	(km s^{-1})	(10^{14} $M_\odot$)	(Mpc)	(10^{44} erg s^{-1})
(1)	(2)	(3)	(4)	(5)	(6)	(7)	(8)	(9)	(10)
MACSJ0916.1−0023	09:16:13.9	−00:24:42	0.320	4.655	0.027	1066*	11.6	1.9	5.9
MACSJ1752.0+4440	17:52:01.5	+44:40:46	0.365	5.073	0.027	1186	15.5*	2.1	6.3
Abell 2744	00:14:18.9	−30:23:22	0.306	4.519	0.012	1301	22.0	2.4	16
MACSJ1258.0+4702	12:58:02.1	+47:02:54	0.331	4.762	0.012	872*	6.3	1.6	3.5
MACSJ1720.2+3536	17:20:16.8	+35:36:26	0.387	5.265	0.034	1068*	11.2	1.9	16

Notes.

Columns are: (1) Name of host cluster of jellyfish galaxy; (2) Right Ascension of the cluster center; (3) Declination of the cluster center; (4) Systematic redshift; (5) Angular scale based on the cosmological parameters of $H_0 = 70$ km s^{-1} Mpc^{-1}, $\Omega_M = 0.3$, $\Omega_\Lambda = 0.7$, and $T_{\mathrm{CMB}} = 2.73$ K; (6) Foreground reddening from Schlafly & Finkbeiner (2011); (7) Cluster velocity dispersion from the following literature: Golovich et al. (2019a) for MACSJ1752+4440, Boschin et al. (2006) for the main clump of Abell 2744, and the scaling relation from Evrard et al. (2008) for the other clusters marked by asterisks; (8), (9) Virial mass and virial radius from the following literature: Medezinski et al. (2018) and Osato et al. (2020) for MACSJ0916−0023, Golovich et al. (2019a) for MACSJ1752.0+4440, and Boschin et al. (2006) for Abell 2744, Sereno & Ettori (2017) for MACSJ1258.0+4702, and Umetsu et al. (2018) for MACSJ1720.2+3536; (10) X-ray luminosity from the ROSAT all-sky survey ($0.1-2.4$ keV; Voges et al. 1999).

JFG2 (z = 0.353; McPartland et al. 2016), A2744-F0083 (z = 0.303; Owers et al. 2012), MACSJ1258-JFG1 ($z = 0.342$; McPartland et al. 2016), and MACSJ1720-JFG1 (z = 0.383; McPartland et al. 2016). Among these five galaxies, A2744-F0083 and MACSJ1258-JFG1 host type I active galactic nuclei (AGN) in their center. We will describe this again with the BPT diagrams (Baldwin et al. 1981) in **Section 3.4.1**. The properties of the host clusters are summarized in **Table 3.2**.

Figure 3.1 shows the *HST*/ACS color composite images of the selected jellyfish galaxies and their host clusters. We display the locations of the brightest cluster galaxies (BCGs) and jellyfish galaxies in the host clusters. In this study, we set the marked BCGs as the center of each cluster. **Figure 3.2** shows the zoom-in thumbnail images of the five jellyfish galaxies. We mark the FOV of the GMOS/IFU 2-slit mode (green boxes; $5'' \times 7''$) and the direction to the cluster center (magenta arrows). In these *HST* optical images, all the jellyfish galaxies show disturbed and asymmetric morphology with blue tails and bright star-forming knots. MACSJ0916-JFG1 has a short ($\sim$ 5 kpc) tail at the eastern side of the galactic center and a few star-forming knots in the disk and tail. MACSJ1752-JFG2 shows not only an extended ($\sim$ 25 kpc) tail towards the southern direction, but also large bright knots with ongoing star formation around the disk. A2744-F0083 is the most spectacular object exhibiting large and bright star-forming knots and multiple stripped tails towards the southwestern direction. MACSJ1258-JFG1 has a bright tail towards the northern direction with a length of $\sim$ 10 kpc and small blue extraplanar knots outside the disk. MACSJ1720-JFG1 is the most distant galaxy in this study. This galaxy shows a star-forming tail in the northern region and a bright compressed region at its head. The FOV of the GMOS/IFU is wide enough to cover the substructures of the jellyfish galaxies except for a few faint tails at the western side of A2744-F0083.

For these jellyfish galaxies, there seems to be no trends between the direction of the tails and their direction towards the cluster center. Tails of MACSJ0916-JFG1 and MACSJ1752-JFG2 are extended in a direction nearly tangential to the cluster center. In contrast, tails of MACSJ1258-JFG1 and MACSJ1720-JFG1 are extended towards the

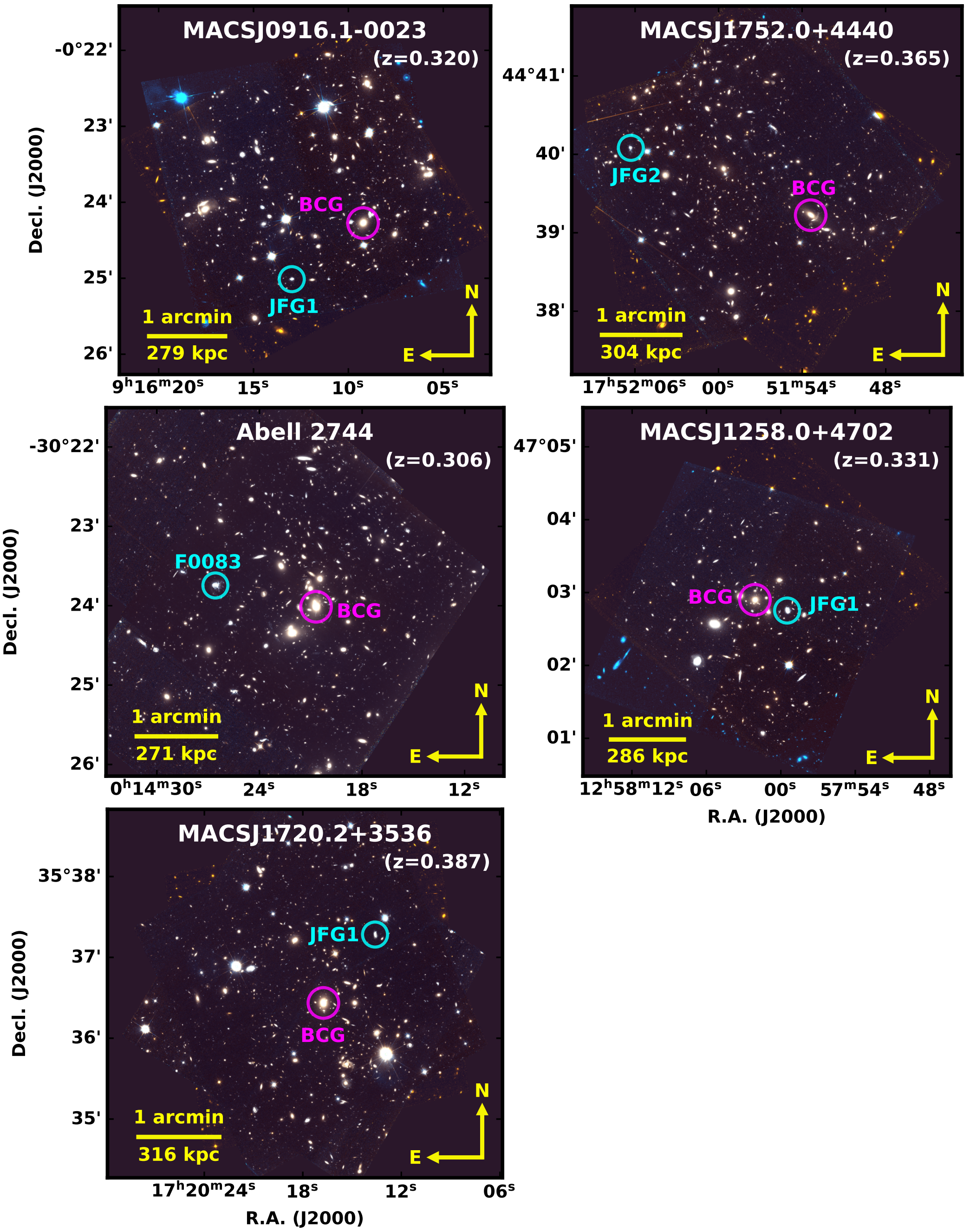

Figure 3.1. *HST* color images of the host clusters of the jellyfish galaxies in this study. These images are combined with the two bands of *HST*/ACS $F606W$ and $F814W$. Cyan circles denote the location of each jellyfish galaxy. Magenta circles denote the brightest cluster galaxy (BCG), which is set to be the center of each cluster. The orientations and the angular scales are marked.

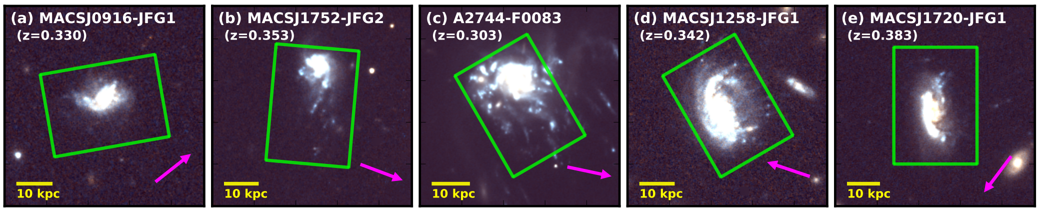

Figure 3.2. The zoom-in *HST* images of the five jellyfish galaxies with the size of $12'' \times 12''$. Green boxes show the field-of-view of the GMOS/IFU 2-slit mode ($5'' \times 7''$). Magenta arrows represent the directions to the cluster center (BCGs). The orientations are same as **Figure 3.1**.

opposite direction to the cluster center. Interestingly, A2744-F0083 has multiple tails extending towards the BCGs in the cluster center. This misalignment of the direction of tails and the direction to the cluster center has been also shown by the jellyfish galaxies in the GASP survey (Poggianti et al. 2016) and those in the IllustrisTNG simulation (Yun et al. 2019). This indicates that these jellyfish galaxies travel in various orbital trajectories within their host clusters, and do not necessarily travel in a radial direction.

3.2.2 Gemini GMOS/IFU Data

Observation

Table 3.3 summarizes our GMOS/IFU observation programs. The five jellyfish galaxies were observed in the 2019A/B and 2021A seasons (PI: Jeong Hwan Lee): MACSJ0916-JFG1 (PID: GS-2019A-Q-214), MACSJ1752-JFG2 (PID: GN-2019A-Q-215), A2744-F0083 (PID: GS-2019B-Q-219), MACSJ1258-JFG1, and MACSJ1720-JFG1 (PID: GN-2021A-Q-205). We obtained the IFU data of MACSJ1752-JFG2, MACSJ1258-JFG1, and MACSJ1720-JFG1 from the site of GMOS-North (GMOS-N) and two other targets (MACSJ0916-JFG1 and A2744-F0083) from GMOS-South (GMOS-S). All the observations used the GMOS/IFU 2-slit mode with an FOV of $5'' \times 7''$.

We observed all galaxies with the exception of A2744-F0083 with the R150 grating and GG455 blocking filter, which securely covers a wide range of wavelengths from

Table 3.3. Gemini GMOS/IFU Observations of the Jellyfish Galaxies in This Study

Galaxy Name	PID	Grating & Filter	λ_{rest}	R	t_{exp}	Date	Airmass	Standard star	Seeing
			(Å)		(sec)	(UT)			(arcsec)
(1)	(2)	(3)	(4)	(5)	(6)	(7)	(8)	(9)	(10)
MACSJ0916-JFG1	GS-2019A-Q-214	R150+GG455	3420 – 7180	1230	4320	2019-03-04	1.29	GD108	0.88
MACSJ1752-JFG2	GN-2019A-Q-215	R150+GG455	3470 – 7090	1260	15040	2019-06-11	1.25	Wolf1346	0.50
A2744-F0083	GS-2019B-Q-219	R400+CaT	6000 – 7110	2440	10320	2019-08-09	1.19	VMa2	1.14
MACSJ1258-JFG1	GN-2021A-Q-205	R150+GG455	3490 – 6910	1200	9900	2021-05-17	1.23	Feige34	0.71
MACSJ1720-JFG1	GN-2021A-Q-205	R150+GG455	3430 – 7080	1270	14400	2021-06-21	1.18	Feige34	0.56

Note.

Columns are: (1) Name of jellyfish galaxy; (2) Program ID; (3) Combination of grating and filter; (4) Rest-frame wavelength coverage; (5) Spectral resolution $R = \lambda/\Delta\lambda_{\mathrm{FWHM}}$ at the wavelength of Hα; (6) Total exposure time; (7) Starting date of the observation; (8) Mean airmass of the observation program; (9) Name of standard star; (10) Seeing FWHM derived from the median FWHMs of stars detected in the following GMOS acquisition images: MACSJ0916-JFG1 (r-band, 60 sec), MACSJ1752-JFG2 (r-band, 15 sec), A2744-F0083 (i-band, 30 sec), MACSJ1258-JFG1 (r-band, 15 sec), and MACSJ1720-JFG1 (r-band, 15 sec).

4700Å to 9200Å in the observer frame ($\sim 3500-6900$Å in the rest frame). This coverage includes strong emission lines from [O II]$\lambda\lambda 3727, 3729$ to [S II]$\lambda\lambda 6717, 6731$. We derived the spectral resolution of the spectra from the telluric emission lines obtained by the sky fibers. The configuration of R150+GG455 has a low spectral resolution of $R \sim 1200$ at the wavelength of the Hα line. For A2744-F0083, the R400 grating and CaT filter were applied with the central wavelength of 8600Å. This combination had limited wavelength coverage from 7820Å to 9260Å (6000-7110Å in the rest frame) but had better spectral resolution ($R \sim 2400$). As a result, the data of A2744-F0083 only covered emission lines from [O I]$\lambda 6300$ to [S II]$\lambda\lambda 6717, 6731$.

MACSJ0916-JFG1 was observed by GMOS-South with an exposure time of 4×1080 s (total 1.2 hr) on the 2019-03-04 (UT). MACSJ1752-JFG2 was observed with the exposure time of 16×900 s + 640 s (total 4.2 hr) during three nights starting from 2019-06-11 (UT). A2744-F0083 was observed with 12×860 s (total 2.9 hr) on the UT dates from 2019-08-09 to 2019-08-30. In the 2021A season, MACSJ1258-JFG1 and MACSJ1720-JFG1 were observed with 11×900 s (total 2.8 hr) and 16×900 s (total 4.0 hr), respectively. The mean airmass of the data ranged from 1.2 to 1.3 for all targets. The median full widths at half maximum (FWHMs) of the seeing in our observations were measured from the acquisition images, ranging about $0\farcs5 - 0\farcs7$ at the GMOS-N and $0\farcs9 - 1\farcs2$ at the GMOS-S.

Data Reduction

We reduced the GMOS/IFU data using the `GEMINI` package in `PyRAF`. We used the tasks of `GBIAS`, `GFREDUCE`, and `GFRESPONSE` for bias subtraction and flat fielding with the Gemini Facility Calibration Unit (GCAL) flat. Since there were some missing fibers that the `PyRAF/Gemini` tasks could not find, we developed our own codes to correct the IFU mask definition file (MDF) for proper flat fielding. We performed the interactive tasks of `GSWAVELENGTH` to obtain the wavelength solution from the CuAr arcs. The scattered light interfering in the fiber gaps was removed by the 2-D surface model with the order of 3 in the `GFSCATSUB` task. After the preprocessing of the science frames, the cosmic rays and the sky lines were removed by `GEMCRSPEC` and `GFSKYSUB` tasks. Four standard stars were used for flux calibrations of our sample: GD108 (MACSJ0916-JFG1), Wolf1346 (MACSJ1752-JFG2), VMa2 (A2744-F0083), and Feige34 (MACSJ1258-JFG1 and MACSJ1720-JFG1). We carried out the flux calibrations by using `GSCALIBRATE` with the Chebyshev polynomials with an order of 11. These reduction processes created individual IFU data cubes with dispersions of 1.95 Å pixel^{-1} for the R150 grating and 0.75 Å pixel^{-1} for the R400. The spatial pixel scale of all cubes is $0\farcs1$ pixel^{-1}. We then carried out the spectral and spatial alignments of the cubes and combined them into one final cube for each target. We used these final data cubes for the analysis of the five jellyfish galaxies in this study.

3.2.3 Archival Images

We used optical and near-infrared (NIR) images of our targets to observe the stellar continuum. This is because the signal-to-noise ratios (S/N) of the GMOS/IFU spectra were not high enough to observe their stellar continuum. We collected the images from archives of the *HST* for optical views and Wide-field Infrared Survey Explorer (*WISE*) and *Spitzer* for NIR views. With these multi-wavelength images, we compared the morphology of the stellar emission with that of the gas emission observed by the GMOS/IFU spectral maps. In addition, we derived stellar masses of the jellyfish galaxies using these images. **Table 3.4** lists the information of the archival images we used for analysis.

HST Optical Images

We retrieved the *HST*/ACS images of the five jellyfish galaxies from the Mikulski Archive for Space Telescopes (MAST). We obtained the individual calibrated images (`flc.fits` or `flt.fits`) and drizzled them by using the `TweakReg` and `AstroDrizzle` tasks in `DrizzlePac`. We combined all the images with a pixel scale of $0\farcs05$ pixel^{-1}.

MACSJ0916-JFG1 and MACSJ1258-JFG1 were covered by 2 optical bands of ACS/$F606W$ and ACS/$F814W$. Both bands were observed by the *HST* program of the snapshot

Table 3.4. Optical and Near-infrared Archival Images of the Jellyfish Galaxies

Galaxy Name	Instrument	Filters	Survey[a]
MACSJ0916-JFG1	*HST*/ACS	$F606W$, $F814W$	PID: 10491, 12166
	WISE	W1 (3.4 μm), W2 (4.6 μm)	All-Sky Data Release
MACSJ1752-JFG2	*HST*/ACS	$F435W$, $F606W$, $F814W$	PID: 12166, 12884, 13343
	Spitzer/IRAC	3.6 μm, 4.5 μm	PID: 12095
A2744-F0083	*HST*/ACS	$F435W$, $F606W$, $F814W$	PID: 13495, 15117
	Spitzer/IRAC	3.6 μm, 4.5 μm	PID: 83, 90257
MACSJ1258-JFG1	*HST*/ACS	$F606W$, $F814W$	PID: 10491, 12166
	Spitzer/IRAC	3.6 μm, 4.5 μm	PID: 12095
MACSJ1720-JFG1	*HST*/ACS	$F435W$, $F606W$, $F814W$	PID: 12455
	Spitzer/IRAC	3.6 μm, 4.5 μm	PID: 545, 90213, 90233

Note.

[a] *HST* - PIs: H. Ebeling (PID 10491, 12166, 12884), D. Wittmann (PID 13343), B. Siana (PID 13389), J. Lotz (PID 13495), C. Steinhardt (PID 15117), and M. Postman (PID 12455), *Spitzer* - PIs: E. Egami (PID 545, 12095), G. Rieke (PID 83), T. Soifer (PID 90257), R. Bouwens (PID 90213), C.Lawrence (PID 90233)

survey of the massive galaxy clusters (PI: H. Ebeling). The drizzled *HST* images had exposure times of 1200 sec for $F606W$ and 1440 sec for $F814W$.

For MACSJ1752-JFG2, we utilized 3 ACS optical bands ($F435W$, $F606W$, and $F814W$). These images were observed by a snapshot survey (PI: H. Ebeling) and a program for weak lensing analysis (PI: D. Wittmann). The exposure times of the final images were 2526 sec ($F435W$), 3734 sec ($F606W$), and 6273 sec ($F814W$).

A2744-F0083 was covered by the HFF (Lotz et al. 2017) and the Buffalo *HST* survey (Steinhardt et al. 2020). We utilized 3 ACS optical bands ($F435W$, $F606W$, and $F814W$) from the surveys. These drizzled images had the longest exposure times among our targets: 45747 sec ($F435W$), 26258 sec ($F606W$), and 108984 sec ($F814W$).

MACSJ1720-JFG1 was observed by a multi-wavelength observation program for the lensing analysis of massive clusters (PI: M. Postman). We utilized 3 ACS optical bands ($F435W$, $F606W$, and $F814W$). The images had exposure times of 2040 sec ($F435W$), 2020 sec ($F606W$), and 3988 sec ($F814W$), respectively.

***Spitzer* and *WISE* NIR Images**

We obtained archival NIR images taken by *Spitzer*/IRAC from the *Spitzer* Heritage Archive (SHA) for all galaxies with the exception of MACSJ0916-JFG1, which was not observed by *Spitzer*. For MACSJ0916-JFG1, we retrieved the *WISE* images from the NASA/IPAC Infrared Science Archive (IRSA). The images were taken from the *WISE* All-Sky Data Release and had exposure times of 7.7 sec for W1 (3.4 μm) and W2 (4.6 μm) bands. As the sensitivity of the W3 (12 μm) and W4 (22 μm) bands are too low, we only used the W1 and W2 images for analysis. MACSJ1752-JFG2 and MACSJ1258-JFG1 were observed by an IRAC snapshot imaging survey of massive clusters (PID: 12095, PI: Egami) with exposure times of 94 sec (3.6 μm) and 97 sec (4.5 μm). As for A2744-F0083, we combined a total of 20 IRAC exposures from two science programs: PID 83 (2 exposures; PI: Rieke) and PID 90257 (18 exposures; PI: Soifer). The exposure times of the combined images were 1878 sec (3.6 μm) and 1936 sec (4.5 μm). MACSJ1720-JFG1 had 6 IRAC exposures from three programs: PID 545

(2 exposures), PID 90213 (3 exposures), and PID 90233 (1 exposure). After combining these images, we obtained the images with exposure times of 374 sec (3.6 μm) and 387 sec (4.5 μm).

3.3 Analysis

3.3.1 Emission Line Fitting

In this study, we focused on analyzing strong emission lines such as Hα, Hβ, [O III], [N II], and [S II] given the low S/N of the spectral continuum in the GMOS/IFU data. First, we removed the background spectral noise from the combined IFU cubes. We took the median value of the spaxels at the edge of the cubes, which has no object signal, as background noise in each cube. We subtracted these noise patterns from all the pixels in the IFU cubes. This process cleaned the unnecessary instrumental noise pattern of the spectra. Next, we carried out Voronoi binning with the Python `vorbin` package (Cappellari & Copin 2003) to obtain high S/N for emission line analysis in each bin. The S/N in the Voronoi bins ranged from 30 to 60 at the Hα+[N II] regions for the jellyfish galaxies, depending on the exposure time and the quality of the data. The numbers of the final Voronoi bins in the IFU cubes were 42 (MACSJ0916-JFG1), 147 (MACSJ1752-JFG2), 175 (A2744-F0083), 215 (MACSJ1258-JFG1), and 166 (MACSJ1720-JFG1). Then, we subtracted the continuum from the spectra of all the Voronoi bins. To estimate the spectral continuum, we applied Gaussian smoothing with a kernel width of 10Å after masking the emission lines.

We then fitted strong emission lines (Hβ, [O III]$\lambda\lambda4959, 5007$, Hα, [N II]$\lambda\lambda6548, 6584$, and [S II]$\lambda\lambda6717, 6731$) with the Markov chain Monte Carlo (MCMC) method using the Python `emcee` package (Foreman-Mackey et al. 2013). For A2744-F0083, we fitted only the Hα+[N II] doublet and [S II] doublet lines. We applied multiple Gaussian functions for fitting the line profiles. For the narrow components of the emission lines, we used three Gaussian profiles for the Hβ+[O III] and Hα+[N II] regions and two for the [S II] doublet. In the case of AGN host galaxies (A2744-F0083 and MACSJ1258-JFG1), more

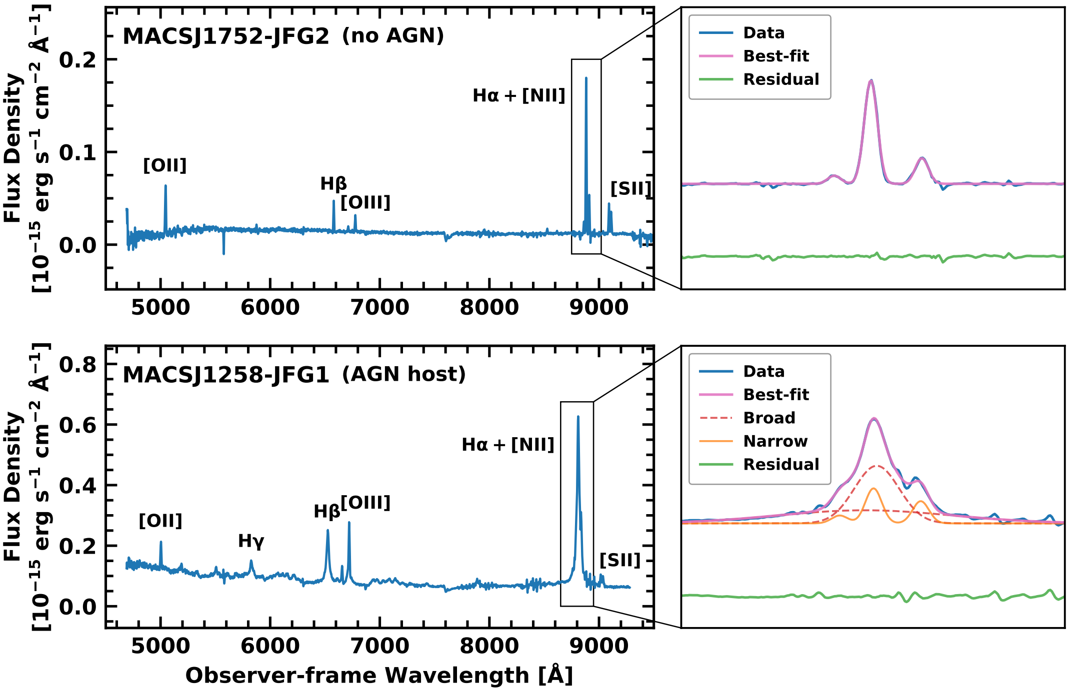

Figure 3.3. Two examples of the integrated spectrum within a radius of $0\farcs4$ from the galactic center of jellyfish galaxies without an AGN (upper panel; MACSJ1752-JFG2) and with an AGN (lower panel; MACSJ1258-JFG1). Several strong emission lines are marked in each spectrum. The right zoom-in panels show the Hα+[N II] region of each galaxy. We plot the observed spectra (blue solid curves), our best-fit models (pink solid curves), and residuals (green solid curves). In the case of an AGN host galaxy, we plot narrow and broad components of the emission lines with orange solid curves and red dashed curves, respectively.

profiles were added for fitting the broad components of the Hβ+[O III] and Hα+[N II] regions.

We initially fitted the emission lines from the central spaxels with high S/N. We then used the initial solutions to run the MCMC process for all the bins. We defined the prior distributions of parameters as Gaussian functions centered on the initial solutions. We implemented the MCMC process in `emcee` with 50 walkers and 2000 steps. After finishing all the MCMC steps of walkers, we measured the skewness and kurtosis of the posterior distributions of parameters to check the reliability of our parameter estimation. We rejected solutions from Voronoi bins with values of skewness and kurtosis higher than 0.5 or lower than −0.5. We took the median values of the posterior distributions as the burn-in solutions of the MCMC process.

In **Figure 3.3**, we plot the GMOS/IFU spectra in the central regions (within a radius of $0\farcs4$) of a non-AGN host galaxy (MACSJ1752-JFG2) and an AGN host galaxy (MACSJ1258-JFG1). We used these integrated spectra for obtaining the initial solutions of the line fitting in all the Voronoi bins. The right panels show the zoom-in spectra at the Hα+[N II] regions overlaid with the best-fit models (pink solid lines). For MACSJ1258-JFG1, we added two more profiles (red dashed lines) for broad components of this region. Residuals (green solid lines) show that the best-fit models represent the spectra well.

3.3.2 Measurements of SFRs, Gas Velocity Dispersion, and Stellar Masses

$H\alpha$-derived SFRs

In this section, we describe how we estimated the SFRs based on the emission line analysis. We derived the SFRs of jellyfish galaxies from their Hα luminosity that was corrected for stellar absorption, extinction, and AGN contamination.

Stellar absorption affects the observed fluxes of the Balmer lines such as Hα and Hβ. Since the S/N of stellar continuum in our GMOS/IFU data is too low to do the full spectrum fitting, we took a simple approach for absorption correction by assuming constant equivalent widths (EWs) of the Balmer absorption lines (Hopkins et al. 2003; Gunawardhana et al. 2011). We used the following formula for the absorption correction,

$$S_{\mathrm{H}\alpha} = F_{\mathrm{H}\alpha} \times \frac{\mathrm{EW}_{\mathrm{H}\alpha} + \mathrm{EW}_c}{\mathrm{EW}_{\mathrm{H}\alpha}}, \tag{3.1}$$

where $S_{\mathrm{H}\alpha}$ is the absorption-corrected Hα flux, $F_{\mathrm{H}\alpha}$ is the observed Hα flux, $\mathrm{EW}_{\mathrm{H}\alpha}$ is the observed Hα EW, and EW_c is the EW for stellar absorption. Hopkins et al. (2003) suggested that the median intrinsic value of EW_c is 2.6Å for the SDSS sample of star-forming galaxies but this value would be reduced to 1.3Å in the real SDSS spectra. This is because SDSS spectra have sufficient spectral resolution ($R \sim 2000$) to resolve broad stellar absorption profiles (see Figure 7 in Hopkins et al. (2003)). Therefore, we adopted $\mathrm{EW}_c = 1.3$Å for A2744-F0083 observed by the R400 grating with a similar resolution ($R \sim 2400$) to the SDSS and $\mathrm{EW}_c = 2.6$Å for the remaining targets observed with the R150 grating ($R \sim 1200$). We applied the same EWs to correct the absorption of Hβ line.

We subsequently corrected for internal dust extinction and foreground extinction. For the dust extinction correction, we used the absorption-corrected flux ratio of the Hα and Hβ lines, otherwise known as the Balmer decrement. We assumed an intrinsic Hα to Hβ flux ratio of 2.86 for the case B recombination with $T_e = 10000$ K and adopted the Cardelli et al. (1989) extinction law. The equations for extinction correction are given as below,

$$A_{\mathrm{H}\alpha} = k_{\mathrm{H}\alpha} \times E(B-V), \tag{3.2}$$

where $A_{\mathrm{H}\alpha}$ is the extinction magnitude of the Hα flux, $k_{\mathrm{H}\alpha}$ is the extinction coefficient for Hα, and $E(B-V)$ is the color excess. We adopted $k_{\mathrm{H}\alpha} = 2.53$ from Cardelli et al. (1989). The color excess can be derived from the equation (3.3).

$$E(B-V) = 2.33 \times \log\left[\frac{S_{\mathrm{H}\alpha}/S_{\mathrm{H}\beta}}{2.86}\right], \tag{3.3}$$

where $S_{\mathrm{H}\alpha}/S_{\mathrm{H}\beta}$ is the absorption-corrected Hα to Hβ flux ratio. We also corrected for foreground extinction using the reddening magnitudes from Schlafly & Finkbeiner (2011) (see **Table 3.2**).

From the corrected Hα flux, we derived the SFRs using the following relation given by Kennicutt (1998) assuming the Chabrier (2003) initial mass function (IMF),

$$\mathrm{SFR}_{\mathrm{H}\alpha} = 4.6 \times 10^{-42} L_{\mathrm{H}\alpha}, \tag{3.4}$$

where $\mathrm{SFR}_{\mathrm{H}\alpha}$ is the Hα-based SFR with unit of $M_\odot$ yr^{-1} and $L_{\mathrm{H}\alpha}$ is the Hα luminosity corrected for stellar absorption and extinction.

Throughout these processes, we rejected the spaxels with S/N (Hα) lower than 3. In addition, we excluded the spaxels classified as AGN and low-ionization nuclear emission-line regions (LINERs) in the BPT diagram, as shown in **Figures 3.4** and **3.5** (see **Section 3.4.1**). For spaxels with S/N $<$ 3 in Hβ and [O III], we used the log([N II]λ6584/Hα) ratio for the classification instead. We classified spaxels with log([N II]λ6584/Hα) > -0.4 as AGN and excluded them from consideration. We also included spaxels with S/N (Hα) $>$ 3 but weak S/N ($<$ 3) of Hβ and the BPT forbidden lines ([O III] and [N II]) for computing the SFR, as done in Medling et al. (2018).

Gas Velocity Dispersion

We derived the gas velocity dispersion ($\sigma_{v,\mathrm{gas}}$) using the standard deviation of Hα emission line corrected for beam-smearing and instrumental dispersion. Beam-smearing occurs when the observed line in an IFU spaxel is blended with the lines from the neighboring spaxels, which makes a broader line profile. Since the seeing FWHM in our observations ranged from $0\farcs5$ to $1\farcs1$, which corresponds from 5 to 11 spaxels for the GMOS/IFU, this effect significantly contributes to the velocity dispersion. Instrumental dispersion is another line-broadening element from the spectral resolution of a spectrograph.

To correct for beam-smearing, we followed the method described in Appendix A in Stott et al. (2016). Using the artificial VLT/KMOS data cube with similar seeing and pixel scale to our GMOS/IFU data, they suggested that a linear subtraction of velocity gradient ($\Delta v/\Delta r$) from the observed velocity dispersion can effectively correct for beam-smearing. This method is described with the equation below,

$$\sigma_{v,\mathrm{cor}} = \sigma_{v,\mathrm{obs}} - \frac{\Delta v}{\Delta r}, \tag{3.5}$$

where $\sigma_{v,\mathrm{cor}}$ is the beam-smearing corrected velocity dispersion, $\sigma_{v,\mathrm{obs}}$ is the observed velocity dispersion, and $\Delta v/\Delta r$ is the maximum velocity gradient at a distance equivalent to the seeing FWHM from the center of a galaxy. Our data cubes showed maximum velocity gradients of $\Delta v/\Delta r = 4.9$ km s^{-1} spaxel^{-1} for MACSJ0916-JFG1, 8.2 km s^{-1} spaxel^{-1} for MACSJ1752-JFG2, 10.6 km s^{-1} spaxel^{-1} for A2744-F0083, 10.5 km s^{-1} spaxel^{-1} for MACSJ1258-JFG1, and 14.8 km s^{-1} spaxel^{-1} for MACSJ1720-JFG1. For comparison, Stott et al. (2016) measured $\Delta v/\Delta r = 13.4$ km s^{-1} spaxel^{-1}.

Then, we subtracted the GMOS/IFU instrumental dispersion from the beam-smearing corrected dispersion. The instrumental velocity dispersion was derived from a single Gaussian fitting of the sky emission lines which were extracted during the data reduction process. We obtained the instrumental velocity dispersion at the wavelength of Hα for our GMOS/IFU data: $\sigma_{v,\mathrm{inst}} = 103.1$ km s^{-1} (MACSJ0916-JFG1), 101.4 km s^{-1} (MACSJ1752-JFG2), 52.2 km s^{-1} (A2744-F0083), 106.1 km s^{-1} (MACSJ1258-JFG1), and 100.1 km s^{-1} (MACSJ1720-JFG1). We used a quadrature removal of instrumental dispersion,

$$\sigma^2_{v,\mathrm{gas}} = \sigma^2_{v,\mathrm{cor}} - \sigma^2_{v,\mathrm{inst}}, \tag{3.6}$$

where $\sigma_{v,\mathrm{gas}}$ is the corrected gas velocity dispersion and $\sigma_{v,\mathrm{inst}}$ is the instrumental velocity dispersion.

Stellar Masses

We estimated the stellar masses (M_*) of our jellyfish galaxies using the NIR images described in **Section 3.2.3**. The GASP studies derived the stellar masses from the spectral continuum fitting (Poggianti et al. 2017). However, our GMOS/IFU data showed too low S/N of the continuum to apply the same method as the GASP studies. Instead, we converted the NIR fluxes of the *Spitzer*/IRAC 3.6 μm and 4.5 μm (W1 and W2 in the case of *WISE* data) to stellar masses following the relation from Eskew et al.

(2012).

$$M_* = \xi \times 10^{5.65} \times S_{3.6\mu\mathrm{m}}^{2.85} S_{4.5\mu\mathrm{m}}^{-1.85} \times (d_L/0.05)^2 \ M_\odot, \tag{3.7}$$

where ξ is the conversion factor from the Salpeter IMF (Salpeter 1955) to other IMFs, $S_{3.6\mu\mathrm{m}}$ and $S_{4.5\mu\mathrm{m}}$ are the NIR fluxes of 3.6 μm and 4.5 μm in Jy, and d_L is the luminosity distance in Mpc. We applied $\xi = 0.54$ for the Chabrier IMF (Chabrier 2003) with a mass range from 0.1 to 100 $M_\odot$. This method has been used for estimating the stellar masses of star-forming galaxies in Abell 2744 (Rawle et al. 2014).

We utilized `photutils v1.0.2` (Bradley et al. 2021) to measure the NIR fluxes of the jellyfish galaxies. We performed aperture photometry using rectangular apertures with the size of the GMOS/IFU FOV ($5'' \times 7''$) for all targets except for MACSJ0916-JFG1. Since MACSJ0916-JFG1 was only observed by *WISE* with poor spatial resolution (FWHM $\sim 6\overset{''}{.}4$ in W1 and W2; Wright et al. 2010), we increased the aperture size to twice the FWHM of the *WISE* images. The derived stellar masses are listed in **Table 3.5**, ranging from log $M_*/M_\odot$ = 9.84 to 10.90.This stellar mass range is also consistent with that of the GASP jellyfish galaxies.

3.3.3 Definition of Disk and Tail

In this study, we spatially divided a jellyfish galaxy into two components – "disk" and "tail". The disk corresponds to main body of the galaxy, and the tail is the extraplanar region composed of ram-pressure stripped ISM outside the disk. To compare our results with the GASP studies, we used the definition of the galaxy boundary between the disk and tail as described in Poggianti et al. (2019) and Gullieuszik et al. (2020). We made use of the emission line maps of the Hα+[N II] region from the GMOS/IFU data. Although the GASP studies used continuum maps of the Hα+[N II] region, it was difficult for this study to use continuum maps due to low S/N. The background level and standard deviation (1σ) were estimated using the DAOPHOT MMM algorithm on the 3σ-clipped data in the emission line maps. We then manually masked the disturbed region of the galaxy, removing tails and extraplanar clumps. With the masked map, we carried out elliptical isophote fitting using `PyRAF/Ellipse`. The galaxy boundary

Table 3.5. Properties of the Jellyfish Galaxies in This Study

Galaxy Name (1)	$\log M_*$ ($M_\odot$) (2)	Hα/Hβ (3)	Total SFR ($M_\odot$ yr^{-1}) (4)	Tail SFR ($M_\odot$ yr^{-1}) (5)	$\lvert\Delta v\rvert_{\rm disk}$ (km s^{-1}) (6)	$\sigma_{v,\rm gas}$ (km s^{-1}) (7)	$P_{\rm ram}$ (dyn cm^{-2}) (8)
MACSJ0916-JFG1	10.18	3.16	7.12	0.56	45.1	30.0	2.0×10^{-10}
MACSJ1752-JFG2	9.84	4.78	30.43	6.76	83.6	43.1	9.8×10^{-11}
A2744-F0083*	10.59	4.29	23.82	8.15	123.1	45.3	2.5×10^{-11}
MACSJ1258-JFG1*	10.90	4.64	35.71	16.80	143.8	100.5	5.4×10^{-10}
MACSJ1720-JFG1	10.64	4.05	17.37	3.28	122.0	104.5	2.8×10^{-11}

Notes.

Columns are: (1) Name of jellyfish galaxy; (2) NIR-derived stellar mass within the GMOS/IFU FOV; (3) Mean flux ratio of Hα to Hβ derived from the integrated spectra; (4) Total SFR value estimated when (3) is uniformly applied; (6) SFR in the tail region; (7) The tail SFR fraction of total SFR ($f_{\rm SFR}$ = SFR(tail)/SFR(total)); (8) The maximum rotational velocity at a radius of disk; (9) Flux-weighted mean value of gas velocity dispersion.

Asterisks (*) marks AGN host galaxies.

between the disk and tail was defined as an elliptical isophote with a surface brightness of 1σ above the background level. The upper right panels of **Figures 3.6-3.10** display the defined boundaries in the five jellyfish galaxies with red dashed ellipses.

3.4 Ionized Gas Properties of the Jellyfish Galaxies

3.4.1 BPT Diagnostics

In **Figure 3.4**, we display the BPT diagram ([O III]λ5007/Hβ vs. [N II]λ6584/Hα) of the five jellyfish galaxies using the narrow components of the emission lines from their integrated spectra. All data used except for A2744-F0083 were taken with the GMOS/IFU. For the BPT diagram of A2744-F0083, we derived their flux ratios from the AAOmega spectra (Owers et al. 2012) because the GMOS/IFU spectra of this galaxy did not cover the Hβ and [O III] region. To determine the gas ionization mechanisms of each galaxy, we classify galaxies into four regions (star-forming, composite, AGN, and LINER) by adopting the well-known boundaries from Kewley et al. (2001), Kauffmann et al. (2003), and Sharp & Bland-Hawthorn (2010), as done in the GASP studies.

MACSJ0916-JFG1 (a) and MACSJ1752-JFG1 (b) are located in the star-forming region, showing the lowest flux ratios of among our sample. A2744-F0083 (c) and MACSJ1258-JFG1 (d) are genuine AGN host galaxies with log([O III]λ5007/Hβ) > 0.5. These galaxies also show broad components of the Balmer emission lines (Hα and Hβ) in their spectra, indicating that they are type I AGNs. MACSJ1720-JFG1 (e) is located in the composite region, showing a higher ratio of log([N II]λ6584/Hα) ~ -0.3 than those from the two star-forming galaxies (log([N II]λ6584/Hα) ~ -0.6). This indicates that the gas ionization in MACSJ1720-JFG1 cannot be solely explained by star formation. However, it is difficult to say that this galaxy hosts a type I AGN in its center, considering that its Balmer emission lines did not show any broad components in our GMOS/IFU spectra. It seems that other excitation mechanisms such as shocks (Rich et al. 2011) or heat conduction (Boselli et al. 2016) could be responsible for ionizing

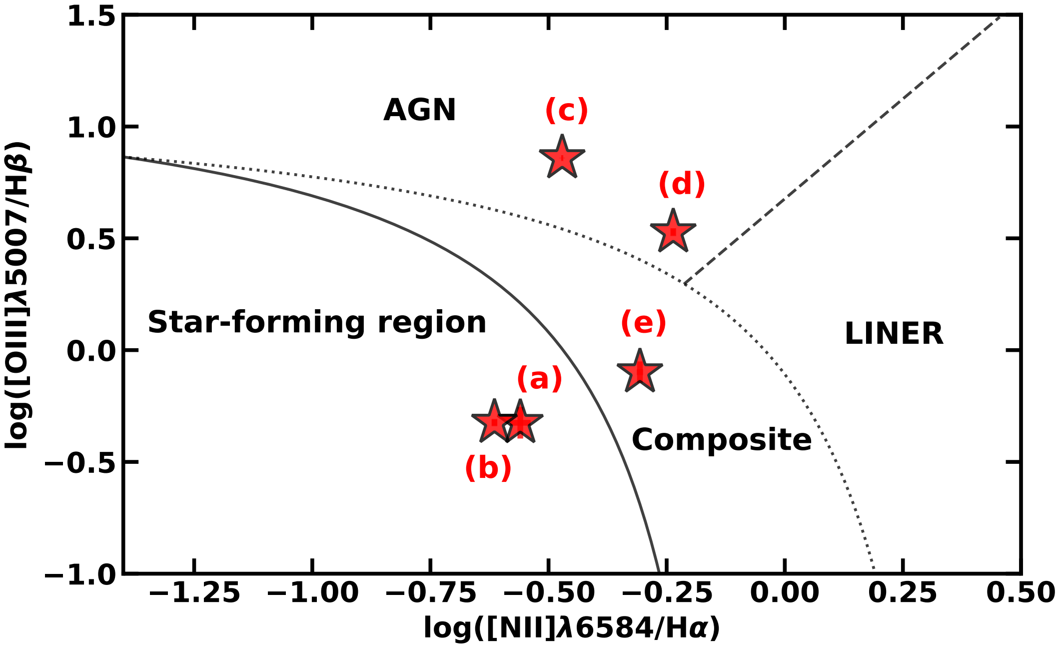

Figure 3.4. A BPT diagram of the integrated spectra of the five jellyfish galaxies. Each galaxy is marked with the same order of **Figure 3.2**: (a) MACSJ0916-JFG1, (b) MACSJ1752-JFG2, (c) A2744-F0083, (d) MACSJ1258-JFG1, and (e) MACSJ1720-JFG1. We plot a solid line from Kauffmann et al. (2003), a dotted line from Kewley et al. (2001), and a dashed line from Sharp & Bland-Hawthorn (2010) to divide star-forming, composite, AGN, and LINER regions in this diagram.

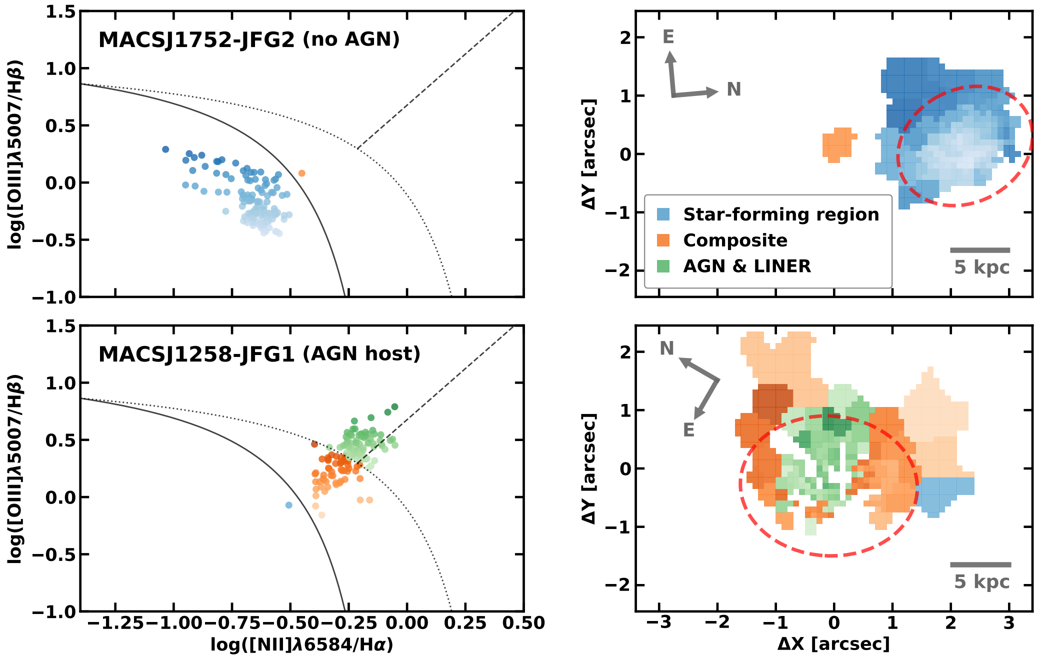

Figure 3.5. *Left panels:* BPT diagrams of the Voronoi bins with S/N $>$ 3 in MACSJ1752-JFG2 (upper; a non-AGN host galaxy) and MACSJ1258-JFG1 (lower; an AGN host galaxy). The colors of the circle symbols represent the BPT classifications: star-forming (blue), composite (orange), and AGN+LINER regions (green). We color-code each symbol with the value of log([O III]λ5007/Hβ). *Right panels:* Spatial maps of the regions classified in the BPT diagrams. Here we exclude the spaxels with lower S/N than 3. Red dashed ellipse represents the boundary of the disk and tail of this galaxy. The orientation and distance scale are marked in the figure.

photons in this galaxy.

Figure 3.5 shows the BPT diagrams of Voronoi bins (left) and their spatial maps (right) of the two jellyfish galaxies as examples of a non-AGN host galaxy (MACSJ1752-JFG2) and an AGN host galaxy (MACSJ1258-JFG1). We only plot the bins with S/N higher than 3 for all the BPT emission lines. In the spatial map, we display all bins with BPT classifications of star-forming (blue), composite (orange), and AGN+LINER (green). For the remaining three galaxies, the GMOS/IFU spaxels show very low S/N of Hβ and [O III] lines (MACSJ0916-JFG1 and MACSJ1720-JFG1) or do not cover the wavelength range of the Hβ and [O III] lines (A2744-F0083). We also plot the boundary between the disk and tail of each galaxy (red dashed ellipse) as obtained from the method described in **Section 3.3.3**.

For MACSJ1752-JFG2, almost all bins belong to the star-forming region except for one bin in the tail region. The central region shows log([N II]λ6584/Hα) ~ -0.6 and log([O III]λ5007/Hβ) ~ -0.3, which are consistent with typical star-forming galaxies. It is also remarkable that the eastern tail region exhibits a higher [O III]/Hβ ratio (log([O III]λ5007/Hβ) > 0) and a lower [N II]/Hα ratio (log([N II]λ6584/Hα) < -0.75) than the central region. The "composite" bin in the southern tail has marginally low S/N, such that the gas ionization source is not clear.

MACSJ1258-JFG1 has high flux ratios of [O III]λ5007/Hβ and [N II]λ6584/Hα, indicating that it hosts an AGN. In this figure, several spaxels in the central region and the head region in the east show low S/N of Hβ and [O III] lines. However, the spaxels with S/N > 3 show that there is a clear radial gradient of the BPT line ratios from the center to the outer region. The outer disk and tail regions on the western side are classified as composite regions, implying that both photoionization and shock-heating contribute to gas ionization there.

3.4.2 SFRs, Gas Kinematics, and Dynamical States

We mainly analyze the ionized gas properties of each jellyfish galaxy using Hα emission lines. From **Figures 3.6** to **3.10**, we map the distributions of the Hα flux, the SFR surface density ($\Sigma_{\rm SFR}$), the radial velocity, and the gas velocity dispersion. We select the Voronoi bins with S/N (Hα) > 3 for the analysis. **Table 3.5** lists the stellar masses, dust extinction, SFRs, tail SFR fraction of total SFR ($f_{\rm SFR}$ = SFR(tail)/SFR(total)), and gas kinematics of the jellyfish galaxies.

To compute and correct the SFRs, we derive dust extinction magnitudes from the flux-weighted mean Balmer decrement (Hα/Hβ). While the Balmer decrement and the extinction magnitude can slightly decrease from the center to the outskirts (a median decrease of ~ 0.25 mag reported in Poggianti et al. (2017)), we choose to assume a constant value throughout the galaxy due to the poor S/N of the Hβ emission lines in the outer regions. As a result, the five jellyfish galaxies in this study shows a median total SFR of 23.8 $M_\odot$ yr^{-1} and a median tail SFR of 6.8 $M_\odot$ yr^{-1}. These SFRs are much higher than those of the GASP sample, with a median total SFR of 1.1 $M_\odot$ yr^{-1} and a median tail SFR of 0.03 $M_\odot$ yr^{-1}. In addition, the median SFR fraction in the tail is also much higher in this study ($f_{\rm SFR} = 22\%$) than in the GASP studies ($f_{\rm SFR} = 3\%$). Lee et al. (2022, submitted) presented a detailed comparison of the star formation activity of the five jellyfish galaxies with that of other known jellyfish galaxies including the GASP sample, considering galaxy stellar mass, redshift, and jellyfish morphology.

For ionized gas kinematics, we derive radial velocities using the peak wavelength measured from fitting. We show line-of-sight radial velocity maps measured with respect to the central spaxels. We calculate the maximum rotational velocity gradient at a circularized radius of the disk ($R_{\rm disk,c} = \sqrt{ab}$, where a and b are the galactocentric radii of the semi-major and semi-minor axis) as an indicator of the rotational speed of ionized gas within the disk.

In addition, we derive gas velocity dispersions as described in **Section 3.3.2** to investigate the dynamical states of the ionized gas in each jellyfish galaxy. The median Hα velocity dispersion obtained by the GASP studies is 27 km s^{-1}, suggesting that the Hα-emitting clumps are dynamically cold (Bellhouse et al. 2019; Poggianti et al. 2019). With this information, we compare the distribution of the gas velocity dispersions in our sample with that of the GASP jellyfish galaxies.

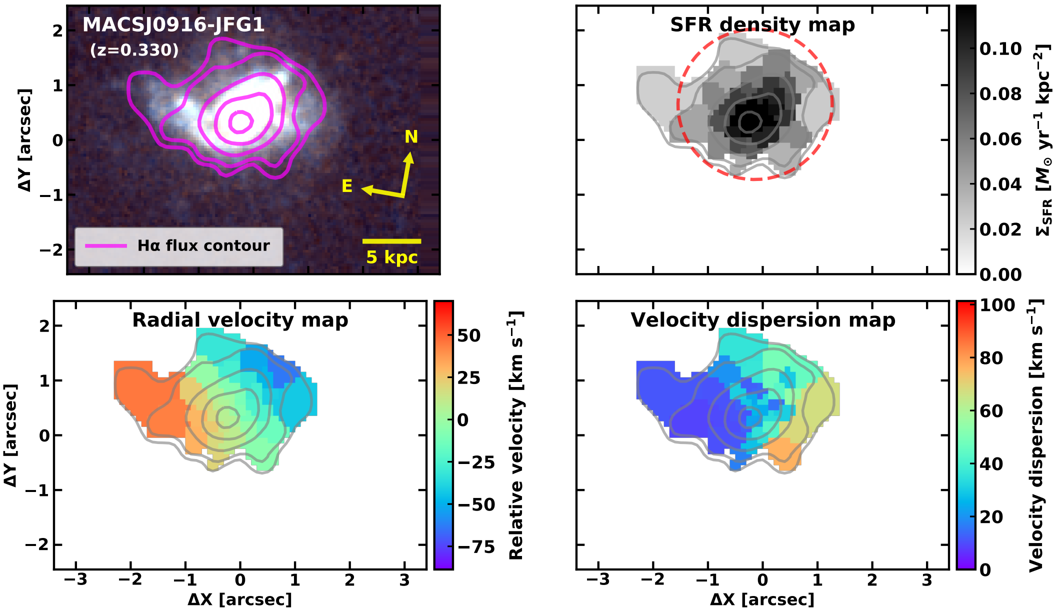

Figure 3.6. *Upper left: HST* color image of MACSJ0916-JFG1 overlaid with the Hα flux contour (magenta solid lines) derived from the GMOS/IFU data. We mark the orientation, distance scale, and redshift of this galaxy. *Upper right:* The SFR density ($\Sigma_{\rm SFR}$) map estimated by the Hα luminosity. Red dashed ellipse represents the boundary of the disk and tail of this galaxy. Gray contours denote the spatial distribution of Hα flux. Right color bar shows the scale and range of the values. *Lower left:* The radial velocity map derived from the peak wavelength of Hα emission line. We display the relative velocity of each bin with respect to the central spaxel with the highest Hα flux. *Lower right:* The gas velocity dispersion map derived from the width of Hα emission line.

MACSJ0916-JFG1

In **Figure 3.6**, it is clear that the Hα flux distribution of MACSJ0916-JFG1 is well-matched with its optical light distribution. The asymmetric feature of the Hα flux perfectly reproduces the eastern tail in the optical image. The Hα flux contours confirm that recent star formation has occurred in the blue knots in the disk and tail.

In the SFR surface density map, we distinguish the disk and tail regions as described in **Section 3.3.3**. The disk region within the 1σ boundary (red dashed ellipse) includes most of the Voronoi bins except for those in the eastern tail. The SFR surface density is highly concentrated in the central region. The flux-weighted mean of the Balmer decrement is 3.16, corresponding to a V-band extinction magnitude of 0.31 mag, which is the lowest value among our sample. The total SFR is estimated to be 7.12 $M_{\odot}$ yr^{-1}, with 6.55 $M_{\odot}$ yr^{-1} for the disk and 0.56 $M_{\odot}$ yr^{-1} for the tail. The tail SFR fraction of total SFR is $f_{\rm SFR} = 7.9\%$, which is the lowest value out of the five jellyfish galaxies.

This galaxy shows a weak rotation of ionized gas in its disk. The line-of-sight velocity relative to the galactic center is -63.7 km s^{-1} (towards the observer) in the northern star-forming knots and 45.1 km s^{-1} (away from the observer) in the eastern tail. In the disk region, the maximum rotational velocity gradient is estimated to be 45.1 km s^{-1} at a disk radius of $R_{\rm disk,c} \sim 1''.4$. The star-forming knots follow the disk rotation well, which is consistently shown in our sample.

The flux-weighted mean of the gas velocity dispersion is $\langle\sigma_{v,\rm gas}\rangle = 30.0$ km s^{-1}, with $\langle\sigma_{v,\rm gas}\rangle = 31$ km s^{-1} for the disk and $\langle\sigma_{v,\rm gas}\rangle = 15$ km s^{-1} for the tail region. In particular, the eastern tail region shows a very low gas velocity dispersion. The low gas velocity dispersion of this galaxy implies that the star-forming regions are dynamically cold, which is consistent with star-forming regions in normal disk galaxies and the jellyfish galaxies of the GASP studies.

MACSJ1752-JFG2

In **Figure 3.7**, MACSJ1752-JFG2 shows a long tail extending ~ 25 kpc ($\sim 5''$ in the angular scale) from the galactic center towards the southern direction. In the Hα flux distribution, our GMOS/IFU data successfully covers the southern tail except for a few faint blue knots in the outer region. This galaxy also shows two disturbed regions at a galactocentric distance of ~ 5 kpc towards the south and east directions, exhibiting luminous blue knots. The Hα flux distribution reproduces these peculiar substructures very well, which is indicative of ongoing star formation in the substructures.

In the SFR surface density map, the "tail" region outside the 1σ boundary (red dashed ellipse) includes the southern tail and some star-forming knots in the east. This galaxy shows the highest Hα to Hβ ratio among our sample (Hα/H$\beta = 4.78$), corresponding to a dust extinction magnitude of 1.61 mag. Correcting for dust extinction, we obtain a total SFR of 30.43 $M_\odot$ yr^{-1} (23.67 $M_\odot$ yr^{-1} in the disk and 6.76 $M_\odot$ yr^{-1} in the tail) with a tail SFR fraction of $f_{\rm SFR} = 22.2\%$. This indicates that the star formation activity is very strong in both the disk and the tail of this object.

MACSJ1752-JFG2 shows a disk rotation with a maximum rotational velocity of 83.6 km s^{-1}. It seems that the substructures follow the disk rotation well, but the southern tail shows a high relative velocity of ~ 100 km s^{-1}. This can be a sign of ongoing RPS, indicating that the tail is stripped away from the center of the galaxy.

We obtain the flux-weighted mean of gas velocity dispersion of $\langle\sigma_{v,\rm gas}\rangle = 43.1$ km s^{-1}, indicating that this galaxy is dynamically cold as well. The mean velocity dispersions of the disk ($\langle\sigma_{v,\rm gas}\rangle = 42$ km s^{-1}) and tail ($\langle\sigma_{v,\rm gas}\rangle = 47$ km s^{-1}) do not show a significant difference. However, there is some difference in the velocity dispersion between the two bright knots in the south and east ~ 5 kpc from the center. The southern large knot shows lower velocity dispersion ($\langle\sigma_{v,\rm gas}\rangle \sim 25$ km s^{-1}) than the eastern one ($\langle\sigma_{v,\rm gas}\rangle \sim 50$ km s^{-1}). This implies that these two knots have different dynamical states, suggesting that ionized gas in the eastern knot is more turbulent than that in the southern one.

A2744-F0083

A2744-F0083 is the most spectacular galaxy, exhibiting numerous star-forming knots outside the main disk and non-ordered tails. There are very bright star-forming knots at

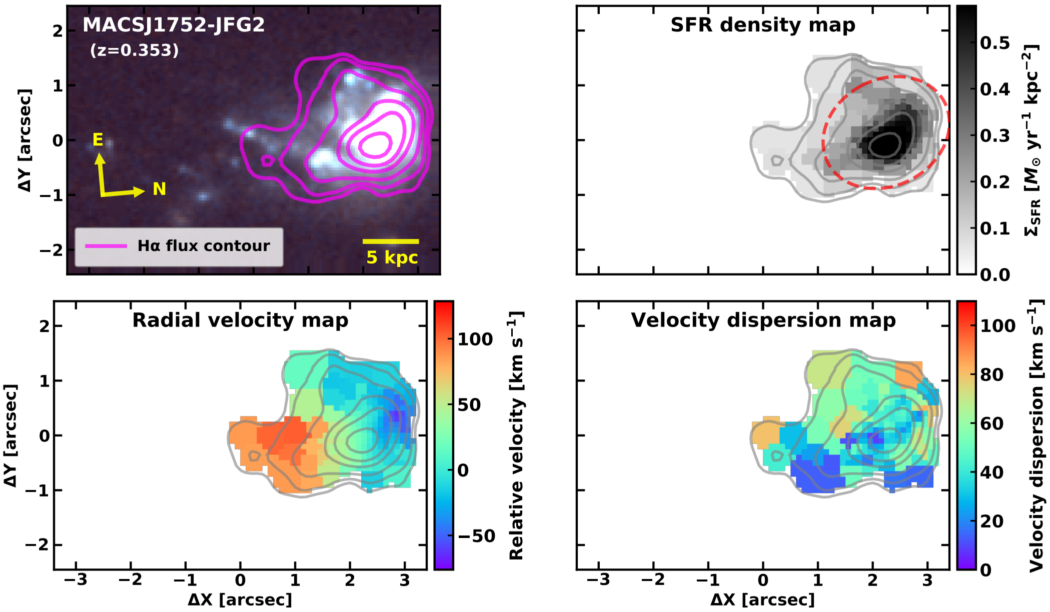

Figure 3.7. Same figure as **Figure 3.6** for MACSJ1752-JFG2.

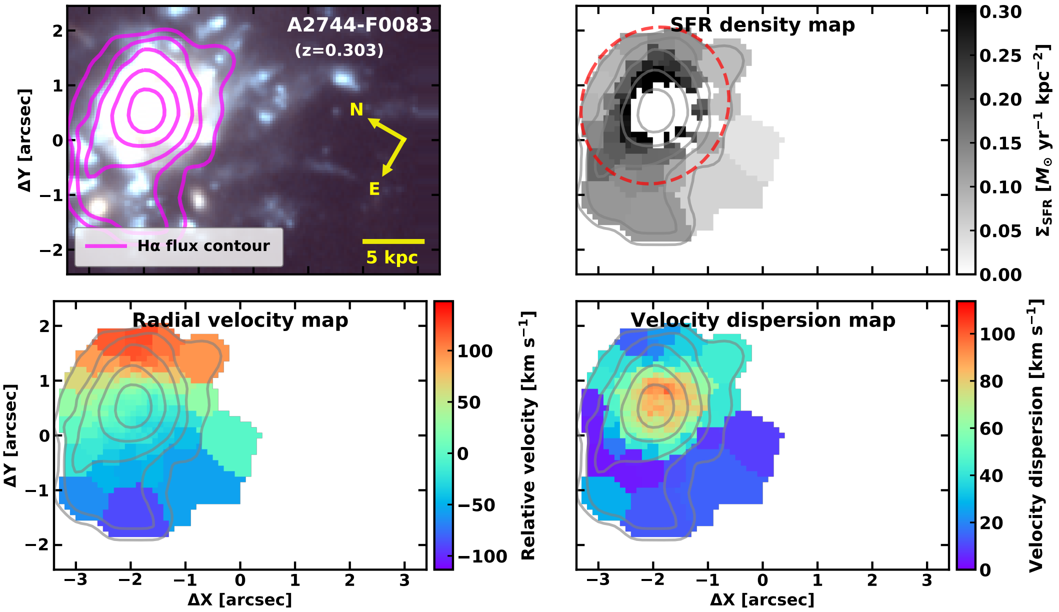

Figure 3.8. Same figure as **Figure 3.6** for A2744-F0083.

both the eastern and western sides of the disk. These knots have comparable sizes and luminosities to compact dwarf galaxies (Owers et al. 2012). The Hα flux distribution is highly asymmetric, peaking in the eastern region. There are also long tails and extraplanar knots to $\sim$ 25 kpc ($\sim$ 5$''\!.$5) towards the southwestern direction from the center, but the Hα S/N of our GMOS/IFU data is very low in these regions. This is because the observation program of A2744-F0083 used the R400 grating with higher spectral resolution and lower S/N for this galaxy. Thus, we mainly analyze the ionized gas properties of the region within $\sim$ 10 kpc ($\sim$ 2$''\!.$2) from the center for this galaxy.

The SFR surface density map shows very strong star formation activity in the disk and in the eastern tail region. Since we remove the AGN contribution to the SFR by subtracting the spaxels with log([N II]λ6584/Hα) > -0.4, several bins in the central region are excluded in the map. For dust correction, we obtain a Hα/Hβ ratio of 4.29 from the AAOmega fiber spectra. The total SFR is 23.82 $M_\odot$ yr^{-1} with a disk SFR of 15.67 $M_\odot$ yr^{-1} and a tail SFR of 8.15 $M_\odot$ yr^{-1} ($f_{\rm SFR}$ = 34.2%). The high SFR ratio in the tail indicates that the blue knots in the east undergo vigorous star formation. For comparison, Rawle et al. (2014) estimated the SFR of this galaxy to be 34.2 $M_\odot$ yr^{-1} based on the sum of the UV and IR luminosities. Different SFR indicators could result in this difference of SFRs because the Hα luminosity used in this study traces more recent star formation than the UV and IR luminosities (Kennicutt & Evans 2012).

The radial velocity map shows a clear disk rotation. The maximum rotational velocity is 123.1 km s^{-1}in the disk ($R_{\rm disk,c} \sim 1''\!.4$). Outside the disk, the star-forming knots in the eastern region show a radial velocity of -88 km s^{-1}. The symmetric feature of the radial velocity distribution indicates that the star-forming regions follow the disk rotation well.

In the gas velocity dispersion map, we observe a clear radial gradient from the central disk ($\langle\sigma_{v,\rm gas}\rangle$ = 54 km s^{-1}) to the tail region ($\langle\sigma_{v,\rm gas}\rangle$ = 18 km s^{-1}). This is because the Hα emission lines from the central disk are contaminated by the AGN activity, which broadens the line profiles. This feature has been also shown in the

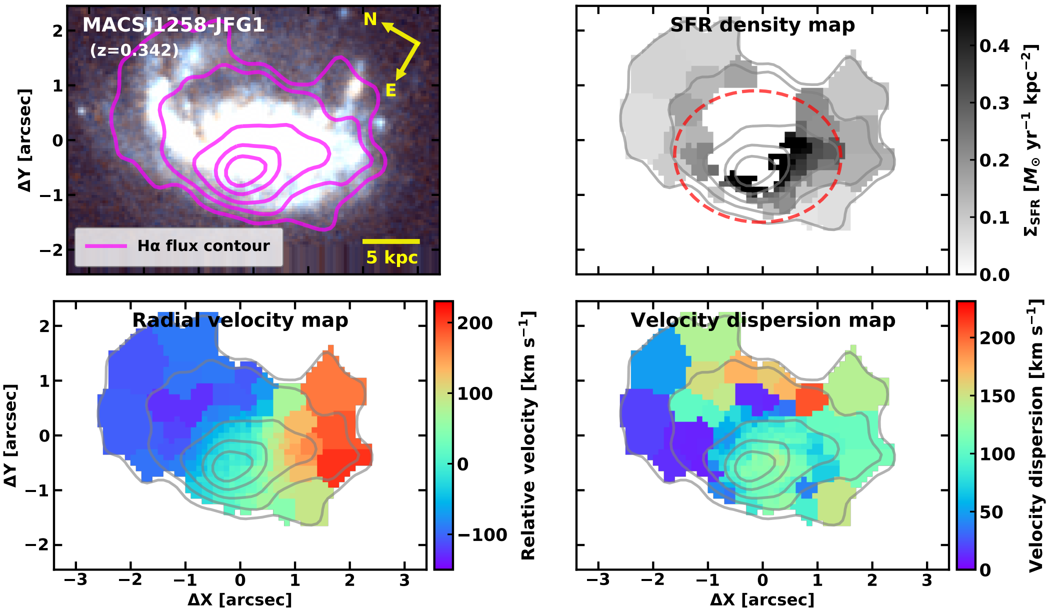

Figure 3.9. Same figure as **Figure 3.6** for MACSJ1258-JFG1.

GASP jellyfish galaxies hosting AGNs (Poggianti et al. 2019). Star-forming knots in the tail region are dynamically cold, which is similar to those in MACSJ0916-JFG1 and MACSJ1752-JFG2.

MACSJ1258-JFG1

MACSJ1258-JFG1 is the most massive galaxy ($\log M_*/M_\odot = 10.90$) among our sample and hosts a type I AGN. In addition, it has a luminous tail as long as ~ 10 kpc ($\sim 2''.1$) in the northern region and plenty of blue knots are distributed around the disk. There is also an asymmetric tail feature in the southwestern region of the galaxy. Overall, these substructures seem to be consistent with the Hα flux distribution of this galaxy.

Like A2744-F0083, the SFR surface density map excludes the central region with the BPT classification of AGN or LINER. We obtain a mean Balmer decrement of 4.64, which corresponds to a V-band extinction magnitude of 1.52 mag. We measure a total SFR of 35.71 $M_\odot$ yr^{-1}, with a disk SFR of 18.91 $M_\odot$ yr^{-1}and a tail SFR of 16.80 $M_\odot$ yr^{-1} ($f_{\rm SFR} = 47\%$). The $f_{\rm SFR}$ value is the highest among our targets. This

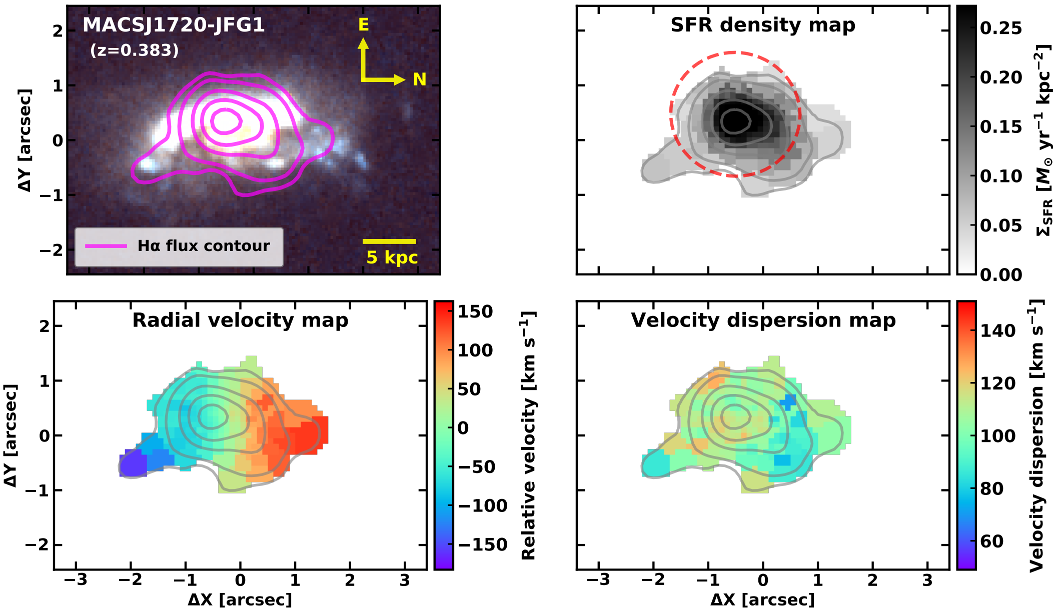

Figure 3.10. Same figure as **Figure 3.6** for MACSJ1720-JFG1.

high fraction of the tail SFR might result from strong star formation activity in the substructures in the northern and the southwestern regions ($\sim$ 10 kpc from the center of the galaxy).

The radial velocity map shows a strong rotation with a maximum rotation velocity of 143.8 km s^{-1} in the disk. The northern tail shows a radial velocity of ~ -100 km s^{-1} and the southern region shows a radial velocity of $\sim$ 150 km s^{-1}. These substructures follow the disk rotation well.

The mean gas velocity dispersion of this galaxy is estimated to be $\langle \sigma_{v,\rm gas} \rangle =$ 100.5 km s^{-1}, which is higher than those of MACSJ0916-JFG1 and MACSJ1752-JFG2. The mean gas velocity dispersion within the disk is $\langle \sigma_{v,\rm gas} \rangle = 93.5$ km s^{-1}, which might be affected by AGN activity like A2744-F0083. The northern tail shows a lower mean velocity dispersion with $\langle \sigma_{v,\rm gas} \rangle \sim$ 50 km s^{-1}, whereas the southern region shows a mean gas velocity dispersion of $\langle \sigma_{v,\rm gas} \rangle \sim$ 90 km s^{-1}. This indicates that ionized gas in the northern tail is dynamically cold and that in the southern region is more turbulent than the northern region.

MACSJ1720-JFG1

MACSJ1720-JFG1 exhibits interesting substructures such as a bright arc-shaped region at the head of the disk and several blue extraplanar knots in the tail region. The blue knots are located at both the north and south sides of the disk. The Hα flux map from the GMOS/IFU data reproduces these optical features well.

The SFR surface density map shows that the distribution of star formation activity is strongly concentrated at the the center of the galaxy. We estimated a mean Balmer decrement, obtaining Hα/Hβ= 4.05 ± 0.82 ($A_V = 1.09$ mag). We derive a total SFR of 17.37 $M_\odot$ yr^{-1}, with a disk SFR of 14.09 $M_\odot$ yr^{-1}and a tail SFR of 3.28 $M_\odot$ yr^{-1} ($f_{\rm SFR} = 19\%$).

The radial velocity map shows a clear disk rotation on the axis of the east-west direction. The maximum rotation velocity within the disk is 122.0 km s^{-1}. The northern tail shows a radial velocity of ~ 120 km s^{-1} and the blue blob in the southern region shows a radial velocity of ~ -100 km s^{-1}. These disturbed features also rotate following the disk of this galaxy, which is similar to other jellyfish galaxies.

This galaxy shows a mean gas velocity dispersion of $\langle \sigma_{v,\rm gas} \rangle = 104.5$ km s^{-1}, which is much higher than those of MACSJ0916-JFG1 and MACSJ1752-JFG2, but similar to that of MACSJ1258-JFG1. This indicates that ionized gas in the star-forming knots of this galaxy seems to be more turbulent than that in the star-forming regions in other jellyfish galaxies. Other shock-heating mechanisms are likely to contribute to the gas ionization in this galaxy, as also suggested by its location in the composite region in the BPT diagram (see **Figure 3.4**).

3.5 Phase-space Diagrams of the Jellyfish Galaxies

Phase-space diagrams are useful to understand the impact of environmental effects on cluster galaxies in relation to their orbital histories (Rhee et al. 2017; Jaffé et al. 2018; Mun et al. 2021). We display the projected phase-space diagrams of our targets and the GASP jellyfish galaxies by categorizing the sample based on stellar mass (**Figure**

3.11) and host cluster velocity dispersion (**Figure 3.12**). We plot the 2D clustercentric distance normalized by the virial radius of the host cluster ($R_{\rm cl}/R_{200}$) on the x-axis, and we plot the velocity relative to the cluster normalized by the cluster velocity dispersion ($|\Delta v_{\rm los}|/\sigma_{v,{\rm cl}}$) on the y-axis. We measure the line-of-sight velocity of each galaxy with $\Delta v_{\rm los} = c \times (z_{\rm gal} - z_{\rm clu})/(1 + z_{\rm clu})$ where c is the speed of light, $z_{\rm gal}$ is the galaxy redshift, and $z_{\rm clu}$ is the cluster redshift. In **Figures 3.11** and **3.12**, we display total SFRs (left panels) and tail SFRs (right panels) at the top of each panel by categorizing the star formation activity: "weak" (red), "moderate" (green), and "strong" (blue) star formation. Gray dashed lines denote the regions (from A to E) classified in Rhee et al. (2017) and Mun et al. (2021), showing the approximate stages of galaxy infall to the clusters: Region A (first infall), B (recent infall), C (intermediate infall), D (ancient infall), and E (field). In this study, we classify the location of jellyfish galaxies as "inner region" ($R_{\rm cl}/R_{200} \leq 0.5$) and "outer region" ($R_{\rm cl}/R_{200} > 0.5$) in their host clusters.

In **Figure 3.11**, we plot phase-space diagrams for different bins of galaxy stellar mass: low-mass ($M_* < 5 \times 10^9\ M_\odot$), intermediate-mass ($5 \times 10^9\ M_\odot < M_* < 5 \times 10^{10}\ M_\odot$), and high-mass ($M_* > 5 \times 10^{10}\ M_\odot$). In the low-mass regime, almost all GASP jellyfish galaxies show weak star formation activity (17/18 in total SFR and 16/18 in tail SFR). They are primarily located in the outer region ($R_{\rm cl}/R_{200} > 0.5$), with only four of them in the inner region ($R_{\rm cl}/R_{200} \leq 0.5$). Note that no galaxies are located in the ancient infall region, implying that the low-mass jellyfish galaxies might be in the early stages of cluster infall.

In the intermediate-mass regime, the GASP jellyfish galaxies show a wide range of clustercentric distances and velocities in their host clusters. These galaxies are also primarily located in the outer region. Most of them show weak star formation activity in terms of tail SFRs. In contrast, four jellyfish galaxies in this study are located in the inner region of the clusters, and they show moderate or strong star activity. With the combined sample of the GASP survey and this study, this panel shows that the fraction of galaxies with weak star formation activity is higher in the outer region (9/18 in total SFR and 15/18 in tail SFR) than in the inner region (1/12 in total SFR and 4/12 in

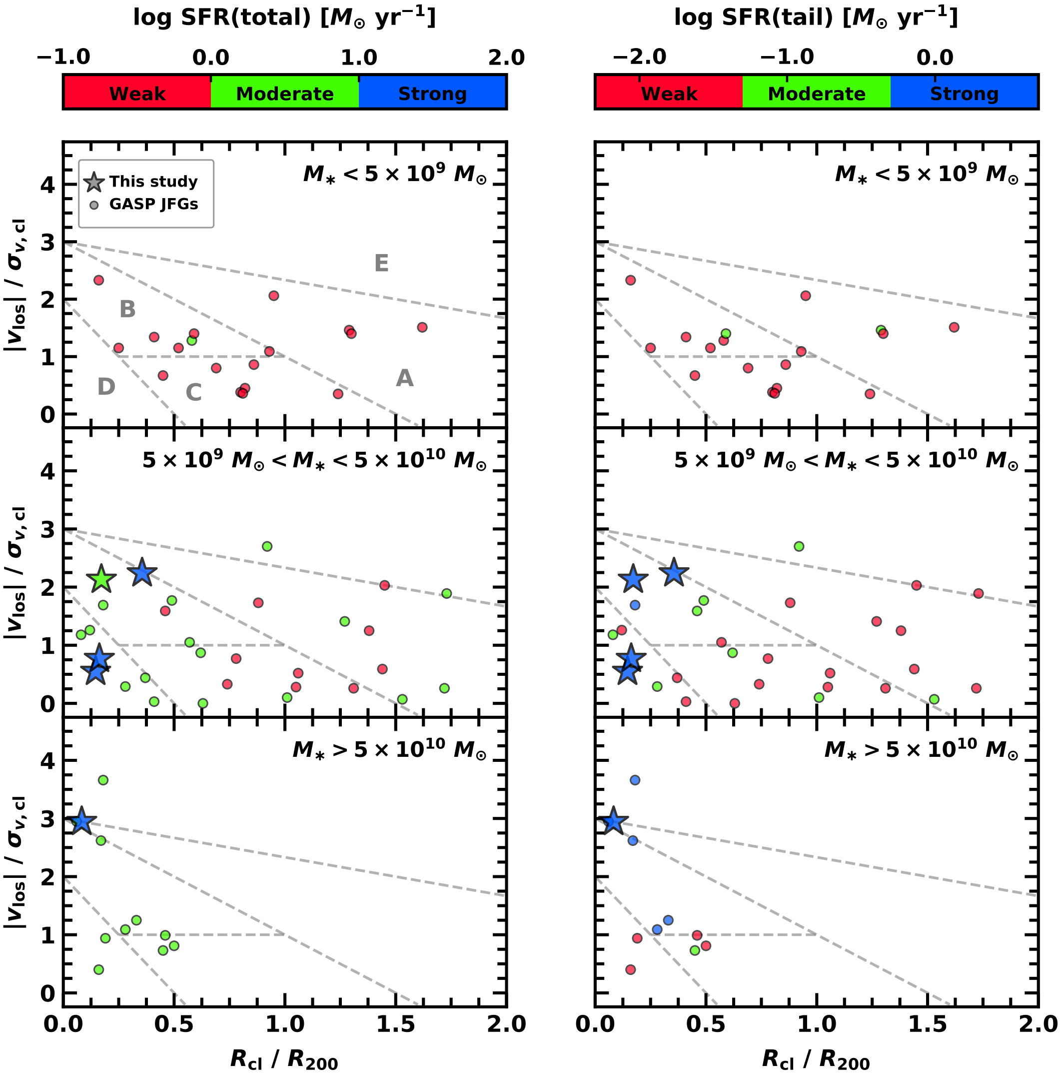

Figure 3.11. Projected phase-space diagrams of our sample (star symbols) and the GASP jellyfish galaxies (circles). We normalize clustercentric distance ($R_{\rm cl}$) and absolute relative velocity ($|v_{\rm los}|$) with cluster virial radius (R_{200}) and velocity dispersion ($\sigma_{v,\rm cl}$), respectively. All the data are color-coded by total SFR (left) and tail SFR (right). The color bars on the top denote the logarithmic scale of each SFR. Gray dashed lines represent the boundaries of the five regions that were roughly defined by infall stages of cluster galaxies (Rhee et al. 2017; Mun et al. 2021): Region A (first infall), B (recent infall), C (intemediate infall), D (ancient infall), and E (field). We divide the whole sample into three categories by stellar mass: low-mass ($M_* < 5 \times 10^9\ M_\odot$; upper), intermediate-mass ($5 \times 10^9\ M_\odot < M_* < 5 \times 10^{10}\ M_\odot$; middle), and high-mass ($M_* > 5 \times 10^{10}\ M_\odot$; lower) galaxies.

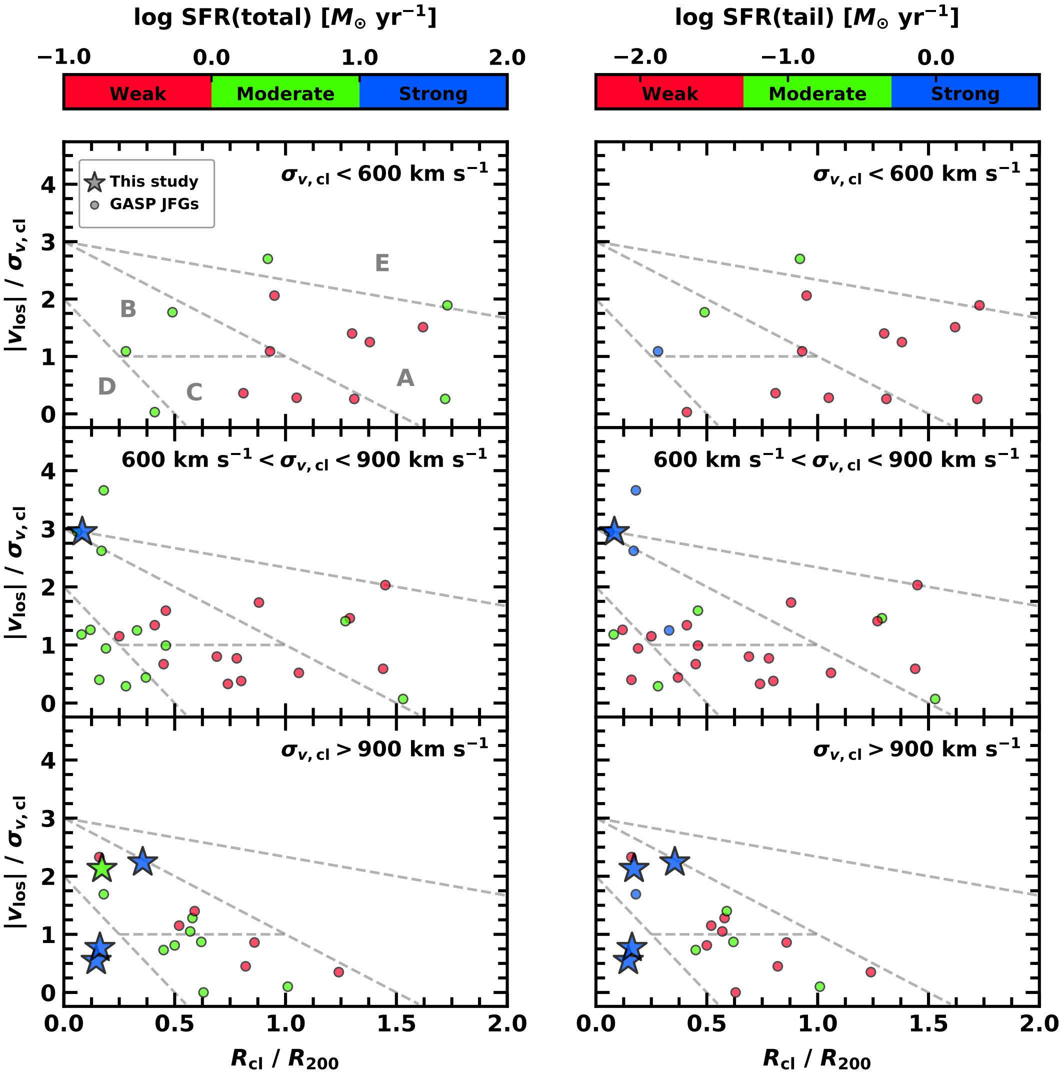

Figure 3.12. Same figure as **Figure 3.11**, but we divide the sample into three categories by cluster velocity dispersion: low-mass ($\sigma_{v,\mathrm{cl}} < 600$ km s^{-1}; upper), intermediate-mass (600 km s^{-1} $< \sigma_{v,\mathrm{cl}} <$ 900 km s^{-1}; middle), and high-mass ($\sigma_{v,\mathrm{cl}} >$ 900 km s^{-1}; lower) clusters.

tail SFR).

In the high-mass regime, there are 10 GASP jellyfish galaxies and MACSJ1258-JFG1 in this study. All massive jellyfish galaxies are located in the inner region of the host clusters. Most of the jellyfish galaxies show moderate or strong star formation activity. The panels in this figure indicates that jellyfish galaxies with higher stellar mass and lower clustercentric distances are likely to exhibit stronger star formation activity on both global (total SFR) and local (tail SFR) scales. This trend has also been observed in Gullieuszik et al. (2020) (see their Figure 4).

In **Figure 3.12**, we plot the phase-space diagrams in different bins of cluster velocity dispersion: low-mass hosts ($\sigma_{v,\rm cl} < 600$ km s^{-1}), intermediate-mass hosts (600 km s^{-1} $<$ $\sigma_{v,\rm cl} < 900$ km s^{-1}), and high-mass hosts ($\sigma_{v,\rm cl} > 900$ km s^{-1}). For the low-mass host clusters, half of the 14 GASP galaxies are located outside the virial radius. A majority of the jellyfish galaxies show weak star formation activity, but galaxies in the inner region mostly show stronger star formation activity than those in the outer region. This trend can be also seen in intermediate-mass host clusters. Most galaxies in the outer region show weak star formation activity (9/11 in total and tail SFR), whereas those in the inner region have a lower fraction of weak star formation activity (4/16 in total SFR and 9/16 in tail SFR). For the high-mass host clusters, there are 14 GASP jellyfish galaxies and 4 galaxies in this study. In terms of total SFRs, the fraction of galaxies with moderate and strong star formation activity (12/18) is higher in high-mass clusters than in low-mass (6/14) and intermediate-mass (13/27) clusters. This trend is also seen with tail SFRs: 3/14 in low-mass, 9/27 in intermediate-mass, and 8/18 in high-mass clusters. This indicates that the star formation activity of jellyfish galaxies in high-mass clusters is likely to be more enhanced compared to those in low-mass and intermediate-mass clusters. In addition, there are no GASP galaxies located in the first infall region (“A”) in these massive clusters in contrast to low- and intermediate-mass clusters. This implies that the jellyfish galaxies in massive clusters are at a later phase of cluster infall than in low-mass clusters.

Combining the GASP sample and our sample, these phase-space diagrams reveal the following. First, our jellyfish galaxy sample is located in the inner region with a wide range of relative velocities. Second, it is clearly shown that jellyfish galaxies in the inner region tend to have higher SFRs than those in the outer region. Third, the star formation activity of jellyfish galaxies tend to increase as galaxy stellar mass increases, as shown in **Figure 3.11**. Finally, the star formation activity of jellyfish galaxies tend to increase as the host cluster velocity dispersion increases, as shown in **Figure 3.12**. We discuss the relationship between the star formation activity of jellyfish galaxies and the host cluster properties further in Lee et al. (2022, submitted).

3.6 Summary

In this study, we observed the five jellyfish galaxies in the MACS clusters and Abell 2744 at $z > 0.3$ with Gemini GMOS/IFU. We investigated the ionized gas properties of these jellyfish galaxies such as ionization mechanisms, kinematics, and SFRs. Our main results can be summarized as follows.

1. The BPT diagrams of [O III]λ5007/Hβ and [N II]λ6584/Hα show that the five jellyfish galaxies have different ionization mechanisms. MACSJ0916-JFG1 and MACSJ1752-JFG2 are located in the star-forming region, indicating that the gas contents in these galaxies are ionized purely by photoionization. On the other hand, A2744-F0083 and MACSJ1258-JFG1 are located in the AGN region with high line ratios of [O III]λ5007/Hβ and [N II]λ6584/Hα. MACSJ1720-JFG1 is located in the composite region, implying a mixed contribution of photoionization and other shock-heating mechanisms.

2. The spatial distributions of the Hα flux are well-matched with the optical features in all five jellyfish galaxies. This indicates that the ionized gas distribution is consistent with that of the stellar light distribution in the jellyfish galaxies.

3. The radial velocity distributions of the jellyfish galaxies indicate that ionized gas in the disk and tail regions rotates around the center of each galaxy. Some tail

regions (e.g. eastern side of MACSJ1752-JFG2) show high relative velocities with respect to the center of the galaxy, which indicates signs of RPS.

4. MACSJ0916-JFG1, MACSJ1752-JFG2 and the tail regions in A2744-F0083 and MACSJ1258-JFG1 show a mean velocity dispersion lower than 50 km s^{-1}, which is consistent with the mean value of star-forming clumps in the GASP jellyfish galaxies. This implies that the ionized gas in those regions is dynamically cold. In contrast, MACSJ1720-JFG1 and the central regions in A2744-F0083 and MACSJ1258-JFG1 show mean velocity dispersions higher than 50 km s^{-1}, indicating that the ionized gas is more turbulent than typical star-forming regions. This could be associated with the AGN activity or other shock-heating mechanisms.

5. The total and tail SFRs of the five jellyfish galaxies are much higher than those of the GASP sample. The median SFRs of our targets are 23.8 $M_{\odot}$ yr^{-1} in total and 6.8 $M_{\odot}$ yr^{-1} in the tails, whereas those of the GASP sample are 1.1 $M_{\odot}$ yr^{-1} in total and 0.03 $M_{\odot}$ yr^{-1} in the tails. In addition, the median SFR fraction in the tail (f_{SFR}) is also much higher in this study ($f_{\mathrm{SFR}} = 22\%$) than in the GASP studies ($f_{\mathrm{SFR}} = 3\%$).

6. In the projected phase-space diagrams, the jellyfish galaxies in this study are located in the inner region with a wide range of orbital velocities relative to the cluster center. Combining the GASP sample and our sample, we find that jellyfish galaxies with higher stellar masses and higher host cluster velocity dispersions are more likely to be located in the inner region of the clusters with more enhanced star formation activity.

Chapter 4

Enhanced Star Formation Activity of Jellyfish Galaxies in Massive Clusters

4.1 Introduction

† A majority of gas-rich galaxies in galaxy clusters undergo ram-pressure stripping (RPS; Gunn & Gott 1972), which is the hydrodynamic interaction of the gas content in a galaxy with the intracluster medium (ICM). RPS effectively removes gas from cluster galaxies, but it can temporarily induce star formation activity in the galaxies. The stripped gas from the galaxies can be compressed by ram pressure, leading to its collapse and to the formation of new stars in the wake of RPS. This occurs within a few hundred Myr, as reproduced by simulations (Bekki & Couch 2003; Kronberger et al. 2008). This process can generate galaxies with jellyfish-like morphologies, showing disturbed tails and extraplanar star-forming knots (Ebeling et al. 2014; Poggianti et al. 2016). These jellyfish galaxies are important targets exhibiting a snapshot of starburst galaxies undergoing RPS.

[†] This chapter is accepted to be published in the Astrophysical Journal Letter (Lee, J. H., et al. 2022, ApJL, accepted, arXiv:2205.05258).

Recent observations have revealed that jellyfish galaxies show systematically enhanced star formation activity compared to normal star-forming galaxies. Using the sample from the GAs Stripping Phenomena (GASP) survey ($z = 0.04 - 0.07$), Vulcani et al. (2018) presented that the jellyfish galaxies show higher star formation rates (SFRs) in their disks by 0.2 dex compared to the control sample without RPS. In addition, observational results for jellyfish galaxies in the A901/2 (Román et al. 2019), A1758N (Ebeling & Kalita 2019), Coma (Roberts & Parker 2020), the clusters from DAFT/FADA and CLASH surveys (Durret et al. 2021), and A1367 (Pedrini et al. 2022) have been in agreement with their star formation enhancements.

The star formation enhancement of jellyfish galaxies is expected to be closely related to the host cluster properties such as cluster mass, cluster dynamics, or ICM density. Previous simulations predicted that the star formation activity of gas-rich galaxies could be strongly triggered in environments with high ICM pressure exerted by cluster merger or shocks (Kapferer et al. 2009; Bekki et al. 2010; Roediger et al. 2014).

However, there has been no observational consensus of any explicit correlation between the RPS-induced SFRs and the host cluster properties. For the GASP sample, Gullieuszik et al. (2020) found no dominant link between tail SFRs and cluster velocity dispersion, suggesting that their stellar mass, position, and velocity also play a role on the SFRs. This might be because the host clusters of the GASP jellyfish galaxies on average have low cluster velocity dispersion ($\langle\sigma_{v,\mathrm{cl}}\rangle \sim 700$ km s^{-1}) and low X-ray luminosity ($\log L_X < 44.5$ erg s^{-1}), implying that most GASP jellyfish galaxies except for a few extreme ones (like JO201 and JW100; Poggianti et al. 2019) are likely to experience weak or mild RPS effects with low ICM density. On the other hand, extreme jellyfish galaxies found in massive merging clusters (Owers et al. 2012; Ebeling & Kalita 2019) would be good examples of vigorous star formation triggered in high ram pressure environments, but quantitative studies of these targets in massive clusters are still lacking.

In this chapter, we address the relation of the SFRs of jellyfish galaxies with host cluster velocity dispersion, ICM density, and strength of ram pressure. Cluster velocity dispersion is a good tracer of cluster mass and dynamics (Munari et al. 2013), and it is also known to have a close correlation with the X-ray luminosity and the ICM density of the cluster (Zhang et al. 2011; Gullieuszik et al. 2020). We estimate the SFRs of five extreme jellyfish galaxies in the MAssive Cluster Survey (MACS) clusters and Abell 2744 ($\sigma_{v,\mathrm{cl}} \gtrsim 1000$ km s^{-1}) based on Gemini GMOS/IFU observations. We also combine the Hα-based SFR values of the known jellyfish samples in the literature in addition to those of our sample, to reveal the relation between SFRs and host cluster properties of the jellyfish galaxies.

This chapter is structured as follows. In **Section 4.2**, we describe the properties of the host clusters of jellyfish galaxies. In **Section 4.3**, we explain the GMOS/IFU data and the methods for analysis. In **Section 4.4**, we show the SFRs of jellyfish galaxies in relation to stellar mass, cluster velocity dispersion, and phase-space diagrams. In **Section 4.5**, we address the relation of the star formation activity of jellyfish galaxies with the host cluster properties and the degree of RPS. Throughout this paper, we use the cosmological parameters with $H_0 = 70$ km s^{-1} Mpc^{-1}, $\Omega_M = 0.3$, and $\Omega_\Lambda = 0.7$.

4.2 Host Cluster Properties

Figure 4.1 shows the relation for the host clusters of jellyfish galaxies between the cluster velocity dispersion ($\sigma_{v,\mathrm{cl}}$) and the X-ray luminosity (L_X) observed in the energy range of $0.1 - 2.4$ keV. The X-ray data of the clusters were obtained from the ROSAT All-Sky Survey (Boehringer et al. 1996; Ebeling et al. 1998; Voges et al. 1999). We plot the data of the GASP clusters (Poggianti et al. 2016; Gullieuszik et al. 2020), 4 nearby clusters (Coma, Abell 3627, Abell 1367, and Virgo; Boselli et al. 2021, and references therein), Abell 1758N (Ebeling & Kalita 2019), and the MACS and HFF clusters (Ebeling et al. 2007; Lotz et al. 2017; Richard et al. 2021), including the host clusters of five extreme jellyfish galaxies (red star symbols). The MACS and HFF clusters show much higher velocity dispersion and X-ray luminosity than the nearby clusters. In comparison with the GASP clusters ($\langle\sigma_{v,\mathrm{cl}}\rangle = 731$ km s^{-1}), the MACS and HFF clusters have a much higher mean velocity dispersion ($\langle\sigma_{v,\mathrm{cl}}\rangle = 1296$ km s^{-1}).

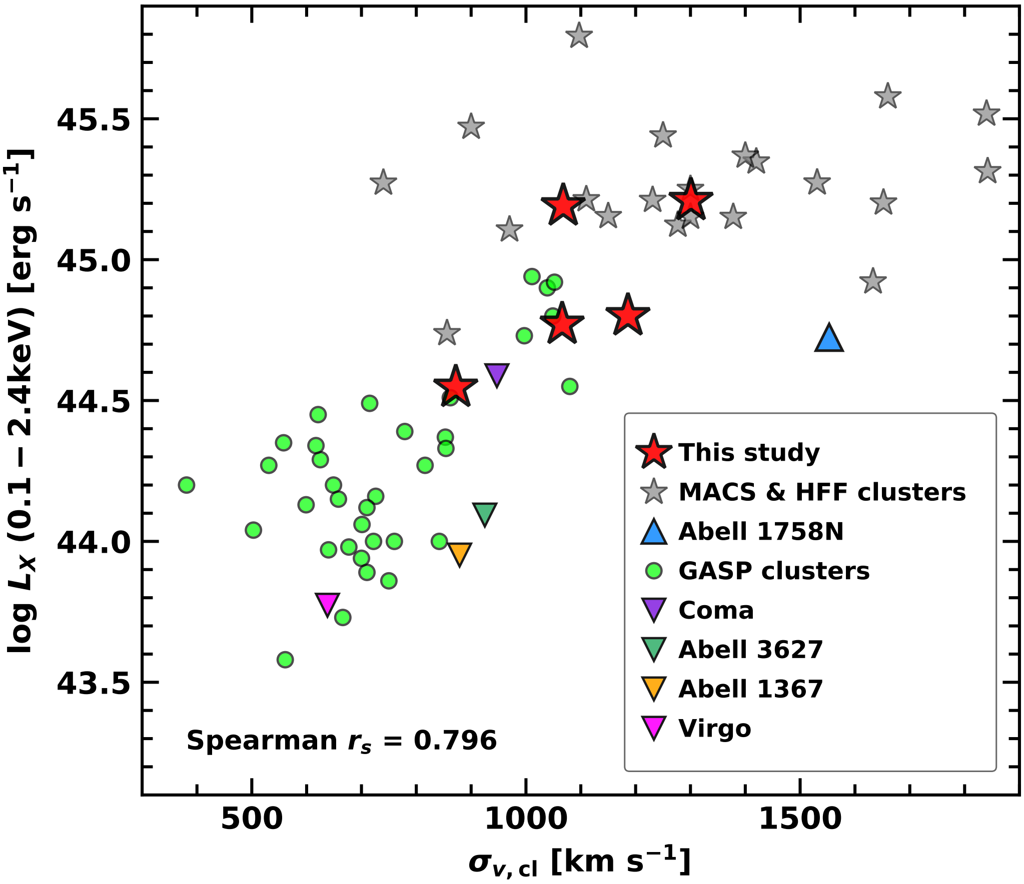

Figure 4.1. Distribution of the X-ray luminosity (L_X) of the host clusters of jellyfish galaxies as a function of the cluster velocity dispersion ($\sigma_{v,\mathrm{cl}}$). Green circles show the data of clusters observed by the GASP survey. Upside-down triangle symbols show several well-known clusters: the Coma cluster (purple), Abell 3627 (green), Abell 1367 (yellow), and the Virgo cluster (magenta). Blue triangle shows the data of Abell 1758N (Ebeling & Kalita 2019). Gray star symbols show cluster samples from the MACS and HFF survey (Ebeling et al. 2007; Lotz et al. 2017; Richard et al. 2021). Red star symbols show the data of the 5 clusters (MACSJ0916.1−0023, MACSJ1752.0+4440, Abell 2744, MACSJ1258.0+4702, and MACSJ1720.2+3536) in this study.

In addition, most of the GASP clusters show lower X-ray luminosity than $\log L_X = 44.5$ erg s^{-1}, but all the clusters from the MACS and HFF show $\log L_X > 44.5$ erg s^{-1}. This indicates that massive clusters like the MACS and HFF clusters have a much denser ICM than the nearby low-mass clusters. In addition, these massive clusters tend to be dynamically unstable with cluster collisions or major mergers, exerting shocks and increasing ram pressure to their member galaxies (Mann & Ebeling 2012; Owers et al. 2012). Thus, the five extreme jellyfish galaxies in the MACS clusters and Abell 2744 are expected to suffer from a much stronger degree of RPS compared to the local jellyfish galaxies such as the GASP sample. This can be also supported by the results from Moretti et al. (2022), which showed that jellyfish galaxies in the central region of the two HFF clusters (Abell 2744 and Abell 370) are undergoing strong RPS.

4.3 Data and Methods

4.3.1 Observations and Data Reduction

We observed five jellyfish galaxies (MACSJ0916-JFG1, MACSJ1752-JFG2, A2744-F0083, MACSJ1258-JFG1, and MACSJ1720-JFG1) during four GMOS/IFU observation programs from March 2019 to June 2021. These jellyfish galaxies were first reported in Owers et al. (2012) and McPartland et al. (2016). We used the 2-slit mode with the field-of-view (FOV) of $5'' \times 7''$ and the gratings of R400 (A2744-F0083) and R150 (the others). The science exposure times ranged from 1.2 hr to 4.2 hr. All the obtained GMOS/IFU data covered at least the Hα+[N II] regions. These GMOS/IFU data were reduced with the `PyRAF/Gemini` package and combined with a pixel scale of $0\farcs1$ pixel^{-1}. The detailed reduction process will be given in Lee et al. (2022, in preparation).

4.3.2 Emission Line Analysis and SFRs

SFRs were derived from Hα luminosity corrected for stellar absorption and dust extinction. We carried out Gaussian smoothing of GMOS/IFU spectra with masking emission lines and subtracted the smoothed continuum from the spectra. We then adopted the

Cardelli et al. (1989) dust extinction laws and the Chabrier (2003) initial stellar mass function (IMF), as used in the GASP studies. Since this study collects and compares the Hα-based SFR values of jellyfish galaxies in the A901/2 (Román et al. 2019, RO19 hereafter) and A1758N (Ebeling & Kalita 2019, EK19 hereafter), we also converted their SFR values to those for Chabrier (2003) IMF for consistency.

The spaxels with S/N (Hα) < 3 or AGN/LINER emission in the BPT diagrams ([O III]λ5007/Hβ vs. [N II]λ6584/Hα) are excluded for computing SFRs. If the Hβ+[O III] region is out of the wavelength coverage or has a lower S/N than 3 in the spectra, we only regarded the spaxels with log([N II]λ6584/Hα) < -0.4) as star-forming ones (Medling et al. 2018). Using these criteria, the spaxels in the central region ($R \lesssim 1''$) of two galaxies (A2744-F0083 and MACSJ1258-JFG1) are classified as the AGN/LINER region. Lee et al. (2022, in preparation) will present the detailed methods for emission line analysis and give the computed values of SFRs.

We also divided each jellyfish galaxy into the disk and tail regions, using the same definition as in the GASP study (Poggianti et al. 2019) to calculate the total SFR, the tail SFR, and the tail SFR fraction ($f_{\rm SFR}$ = SFR(tail)/SFR(total)). Unlike the MUSE IFU data used in the GASP studies, our GMOS/IFU spectra have too low S/N to perform the spectral continuum fitting. Instead, we estimated stellar masses of the jellyfish galaxies from their NIR fluxes within the GMOS/IFU FOV.

4.3.3 Strength of Ram Pressure

The ram pressure on a galaxy can be computed with $P_{\rm ram} = \rho_{\rm ICM} \times \Delta v_{\rm 3D}^2$, where $\rho_{\rm ICM}$ is the ICM density and $\Delta v_{\rm 3D}^2$ is the 3D relative velocity of the galaxy with respect to the surrounding ICM (Gunn & Gott 1972). For the ICM density, we assumed the static ICM β-model:

$$\rho_{\rm ICM}(r_{\rm cl,3D}) = \rho_0 \times \left[1 + \left(\frac{r_{\rm cl,3D}}{R_c}\right)^2\right]^{-3\beta/2}, \tag{4.1}$$

where ρ_0 is the ICM density at the cluster center, $r_{\rm cl,3D}$ is the 3D clustercentric distance, and R_c is the core radius of the host cluster. We assumed $\beta = 0.5$ and adopted Equation 16 in Gullieuszik et al. (2020) to derive ICM density from cluster velocity dispersion.

We converted the projected clustercentric distance ($R_{\rm cl}$) and the line-of-sight velocity ($\Delta v_{\rm los}$) to the 3D parameters ($r_{\rm cl,3D}$ and $\Delta v_{\rm 3D}$) by multiplying a factor of $\pi/2$ and $\sqrt{3}$, respectively (Jaffé et al. 2018).

There are several caveats of this method. First, the static ICM β-model might be difficult to be applied to clusters undergoing collisions or mergers. For example, merging clusters such as MACSJ1752.0+4440 and Abell 2744 exhibit a disturbed X-ray morphology (Owers et al. 2011; Finner et al. 2021), implying that the ICM distribution is not homogeneous. Second, the scaling relations in Gullieuszik et al. (2020) might have non-negligible scatter. These relations were derived from a simple linear interpolation of two model clusters (a low-mass cluster and a high-mass cluster) from Table 1 in Jaffé et al. (2018). Thus, the relations could be oversimplified for estimating the ICM density in clusters with a wide range of virial masses. Third, the projection effect could lead to scatter. Despite these limitations, we roughly computed the strength of ram pressure of jellyfish galaxies to investigate the relation between the star formation activity and the degree of RPS in **Section 4.5**.

4.4 Star Formation Activity of the Jellyfish Galaxies

4.4.1 Comparison of SFRs with the GASP Sample

In the left panels of **Figure 4.2**, we plot the total SFRs (upper), tail SFRs (middle), and $f_{\rm SFR}$ (lower) of our GMOS/IFU sample and the GASP sample as a function of stellar mass. The stellar mass range of our targets in this study is $\log M_*/M_\odot = 9.8 - 10.9$, which is comparable to that of the massive GASP jellyfish galaxies. Total SFRs of the GASP jellyfish galaxies are clearly proportional to stellar mass. Our targets show a similar trend, but the total SFRs are by a factor of 10 higher than those of the GASP sample in a similar stellar mass range. The five jellyfish galaxies show a median SFR of 23.8 $M_\odot$ yr^{-1} in total, whereas the GASP sample shows 1.1 $M_\odot$ yr^{-1}. Tail SFRs of the GASP jellyfish galaxies increase as the stellar mass increases in the range of $M_* > 10^{10}$ $M_\odot$. In the low-mass regime ($M_* < 10^{10}$ $M_\odot$), such trend is not clear due

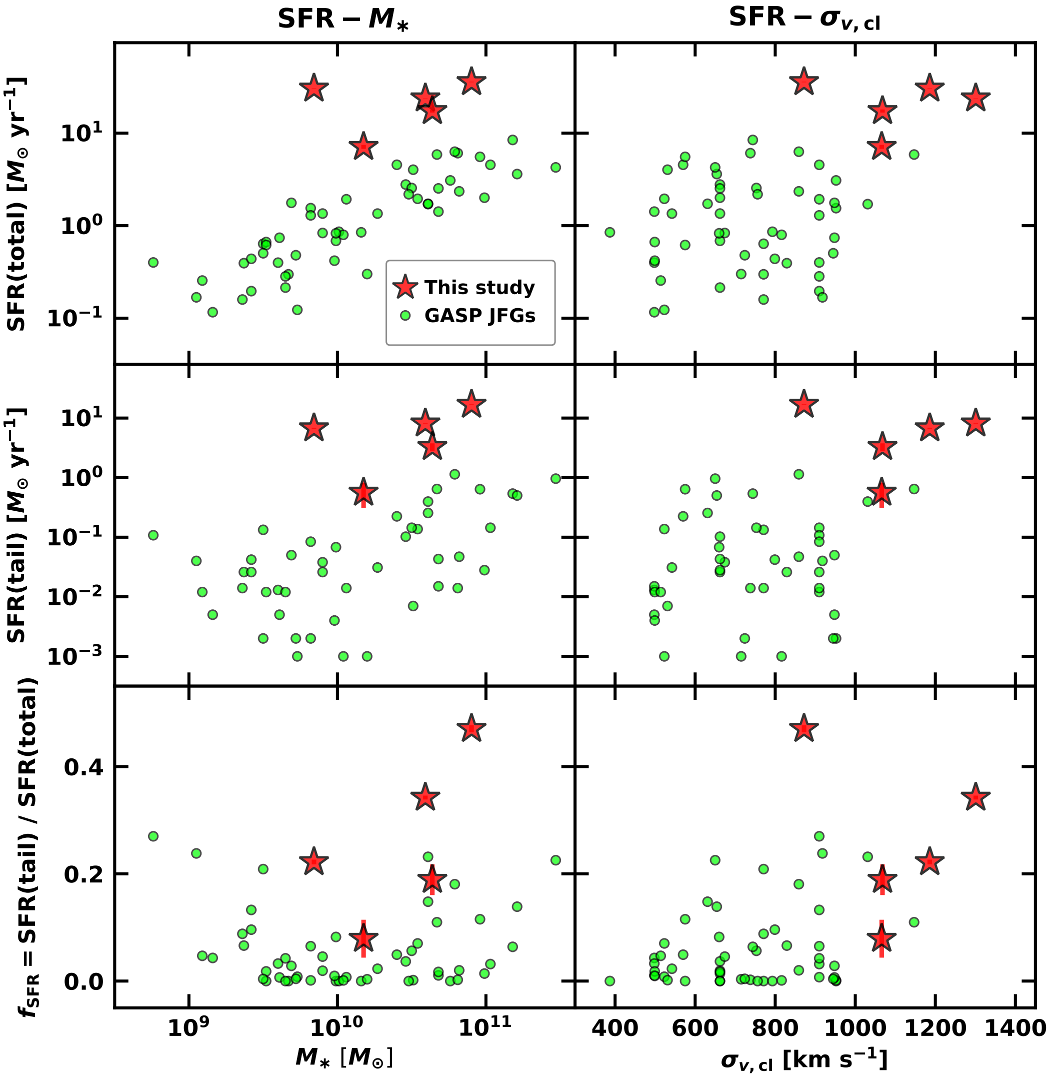

Figure 4.2. Total SFR (upper), tail SFR (middle), and the tail SFR fraction (f_{SFR}; lower) as a function of stellar mass (left) and cluster velocity dispersion (right). We plot our data (red star symbols) and 54 jellyfish galaxies observed by the GASP survey (green circles) for comparison.

to the large scatter. Our targets show higher tail SFRs (median = 6.8 $M_\odot$ yr^{-1}) than the GASP sample (median = 0.03 $M_\odot$ yr^{-1}). The median $f_{\rm SFR}$ of our sample is 22%, which is also by a factor of 10 higher than the GASP sample with $f_{\rm SFR} = 3\%$. Overall, the star formation activity of our sample is more enhanced than that of the GASP sample in terms of total SFR, tail SFR, and $f_{\rm SFR}$.

In the right panels, we plot the total SFR, tail SFR, and $f_{\rm SFR}$ versus the cluster velocity dispersion. The figures show that there is no significant correlation between SFRs (or $f_{\rm SFR}$) and the host cluster velocity dispersion when only the GASP sample is taken into account, as mentioned in Gullieuszik et al. (2020). The jellyfish galaxies in this study help us probe higher values of cluster velocity dispersion. The host clusters of our sample have a median velocity dispersion of $\sigma_{v,\rm cl} = 1068$ km s^{-1}, which is much higher than that of the GASP clusters (median $\sigma_{v,\rm cl} = 731$ km s^{-1}). Combining our data and the GASP sample, we find that the SFRs and $f_{\rm SFR}$ of jellyfish galaxies tend to increase as the cluster velocity dispersion increases. This implies there may be a positive correlation between the star formation activity and the cluster velocity dispersion in spite of large scatters. We discuss this correlation further in **Section 4.5**.

4.4.2 Phase-space Analysis with Jellyfish Morphology

In **Figure 4.3**, we illustrate the projected phase-space diagrams of our targets in addition to samples from the GASP survey (Gullieuszik et al. 2020), A901/2 supercluster (RO19), and A1758N (EK19). We color-code all the jellyfish galaxies with the total SFRs (left panels) and tail SFRs (right panels). Here we categorize the jellyfish galaxies with the visual classification in Poggianti et al. (2016): JClass = 1, 2, 3 (tentative or probable jellyfish candidates) and JClass = 4, 5 (classical jellyfish galaxies). The jellyfish galaxies with higher JClass show stronger RPS signatures such as bright tails and extraplanar knots in the optical images or Hα flux distributions. For the GASP sample, the JClass values were given in Gullieuszik et al. (2020). RO19 also adopted the JClass as a morphological index of the selected jellyfish sample. EK19 classified their sample into galaxies with discernible tails (JFG1 and d1 to d3) and ambiguous

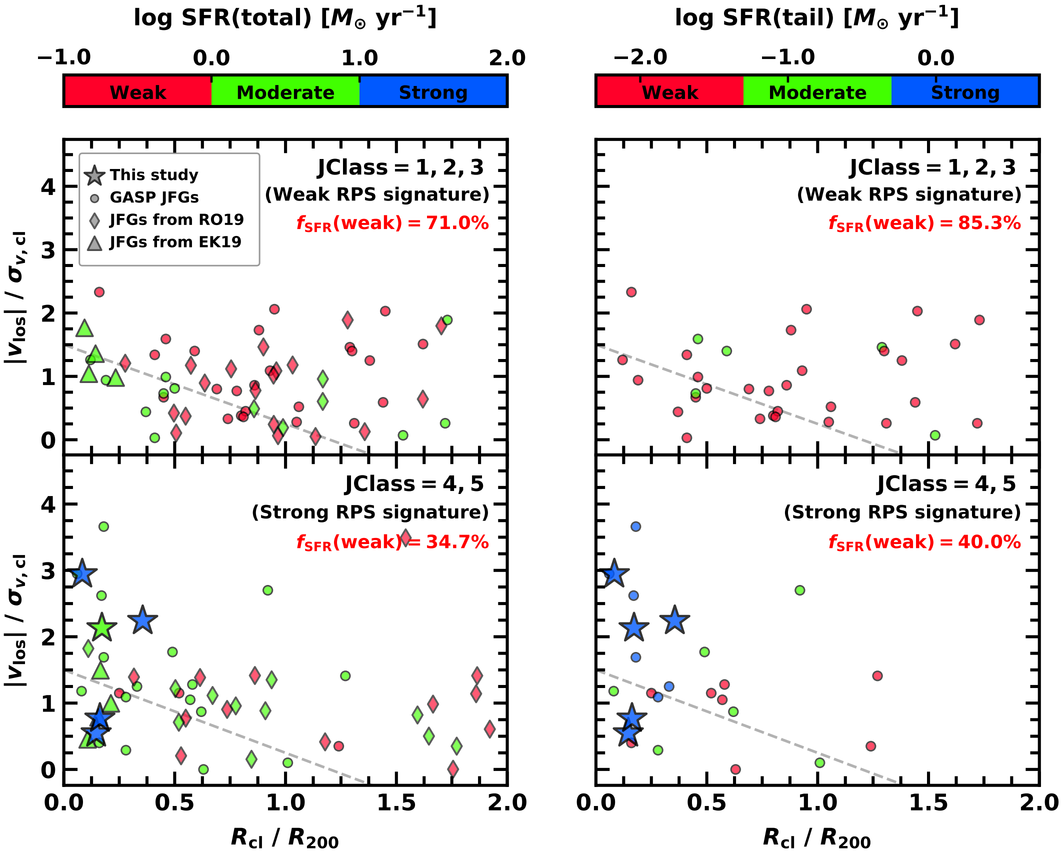

Figure 4.3. Projected phase-space diagrams of our sample (star symbols), the GASP jellyfish galaxies (circles), the A901/2 sample (RO19; diamonds), and the A1758N sample (EK19; triangles). We normalize clustercentric distance ($R_{\rm cl}$) and absolute relative velocity ($|v_{\rm los}|$) with cluster virial radius (R_{200}) and velocity dispersion ($\sigma_{v,\rm cl}$), respectively. All the data are color-coded by total SFR (left) and tail SFR (right). The color bars on the top denote the logarithmic scale of each SFR, showing the three categories of star formation activity: ‘weak’, ‘moderate’, and ‘strong’. Gray dashed lines represent a boundary of virialized region and recent infall region (Jaffé et al. 2015). We divide the whole sample into two categories by JClass from the GASP studies (Poggianti et al. 2016; Jaffé et al. 2018; Gullieuszik et al. 2020): weak RPS signature (JClass = 1, 2, 3; upper) and strong RPS signature (JClass = 4, 5; lower) in the jellyfish galaxies.

RPS features (d4 to d7). Our GMOS/IFU targets were regarded as classical examples of jellyfish galaxies in previous studies (Ebeling et al. 2014; McPartland et al. 2016), so we classified all our targets as “strong RPS signature”.

The phase-space diagrams show that the jellyfish galaxies with strong RPS signatures show higher SFRs in total and in tails than those with weak RPS signatures. Furthermore, the GASP and RO19 samples with strong RPS features are more concentrated on the cluster center than those with weak RPS features (p-value = 0.06 for one-sided Kolmogorov-Smirnov test). This implies that the jellyfish galaxies with stronger RPS signatures show more enhanced star formation activity compared to those with weaker ones.

4.4.3 Comparison of SFRs with the SFMS

In **Figure 4.4**, we plot the integrated SFR-M_* diagrams of the jellyfish galaxies in comparison with the star formation main sequence (SFMS) at the median redshifts of the jellyfish samples: the GASP galaxies ($z = 0.05$; a), the A901/2 sample ($z = 0.17$; b), the A1758N jellyfish galaxies ($z = 0.28$; c), and our sample ($z = 0.34$; d). We adopted the following SFMS in Speagle et al. (2014) as a function of stellar mass and cosmic time.

$$\log \mathrm{SFR}(M_*,\ t) = (0.84 - 0.026 \times t) \log M_* - (6.51 - 0.11 \times t), \tag{4.2}$$

where t is the age of the universe at the redshift of the galaxies in Gyr. This SFMS model was derived from a compilation of 25 previous studies, most of which studied star-forming galaxies in the field environments. Note that the SFRs of cluster galaxies could be more suppressed compared to the above SFMS because the SFR-M_* relation also depends on the environment as shown in the studies of star-forming galaxies at low-z (Paccagnella et al. 2016) and intermediate-z (Vulcani et al. 2010).

In the upper panels, we plot the data of the GASP sample (left) and the A901/2 sample (right) whose host systems have on average lower velocity dispersions than 1000 km s^{-1}. The GASP clusters have a mean cluster velocity dispersion of 731 km s^{-1}, and the 4 subgroups in A901/2 have velocity dispersions of $\sigma_{v,\mathrm{cl}} = 878$ km s^{-1} for

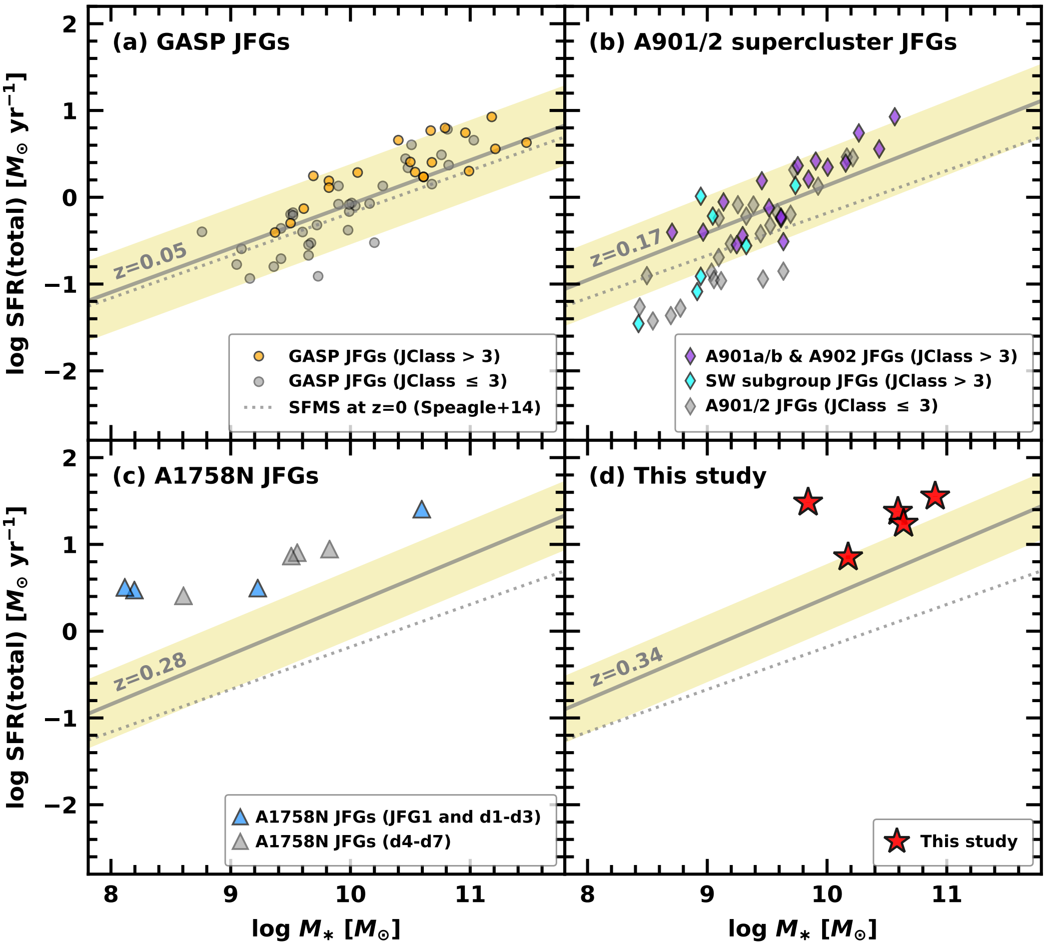

Figure 4.4. The SFR-M_* diagrams of jellyfish galaxies from the GASP survey (upper left), the A901/2 supercluster (RO19; upper right), A1758N (EK19; lower left), and our GMOS/IFU study (lower right) compared with the star formation main sequence (SFMS) at the median redshift of each sample. In the left panel, we mark jellyfish galaxies with strong RPS signatures as colored symbols and those with weak RPS signatures as gray symbols. Solid lines and shaded regions show the linear-fit lines of the SFMS and their uncertainty suggested by Speagle et al. (2014). Gray dashed lines denote the linear-fit line of the SFMS at $z = 0$.

A901a, $\sigma_{v,\rm cl} = 937$ km s^{-1} for A901b, $\sigma_{v,\rm cl} = 808$ km s^{-1} for A902, and $\sigma_{v,\rm cl} = 585$ km s^{-1} for the southwest (SW) group (Weinzirl et al. 2017). For the GASP sample, most jellyfish galaxies with JClass > 3 exhibit higher SFRs than not only those with JClass ≤ 3 but also those that lie along the SFMS. The jellyfish galaxies in the A901/2 supercluster seem to follow a similar trend with the GASP sample. Furthermore, the jellyfish galaxies with JClass > 3 in more massive subgroups (A901a/b and A902) show higher SFR excess relative to the SFMS than those in the SW group. These results indicate that the jellyfish sample exhibits more enhanced star formation activity as their RPS features become stronger and their hosts become more massive.

In the lower panels, we plot the data of A1758N sample and our sample in massive clusters ($\sigma_{v,\rm cl} \gtrsim 1000$ km s^{-1}). All the jellyfish galaxies of A1758N and ours are located clearly above the SFMS, implying that the jellyfish galaxies in massive clusters tend to show more enhanced star formation activity compared to those in the GASP clusters and the A901/2 subgroups. Thus, the significant enhancement of the star formation activity could be due to the difference in the properties of the host clusters (e.g. the cluster mass, cluster velocity dispersion, or ICM density) which affects the strength of ram pressure on the jellyfish galaxies.

4.5 The Relation between the Star Formation Activity and RPS

In this section, we explore how the star formation activity of jellyfish galaxies depends on their host cluster velocity dispersion and the strength of ram pressure. We estimate the value of starburstiness ($R_{\rm SB}$) of the jellyfish galaxies, defined as a ratio between the specific star formation rate (sSFR) of a galaxy to that of the SFMS at the same redshift, indicative of relative star formation activity with respect to the normal galaxies (Elbaz et al. 2011).

Figure 4.5 illustrates the starburstiness of the jellyfish galaxies as a function of the host cluster velocity dispersion (left panel), the ICM density (middle panel), and

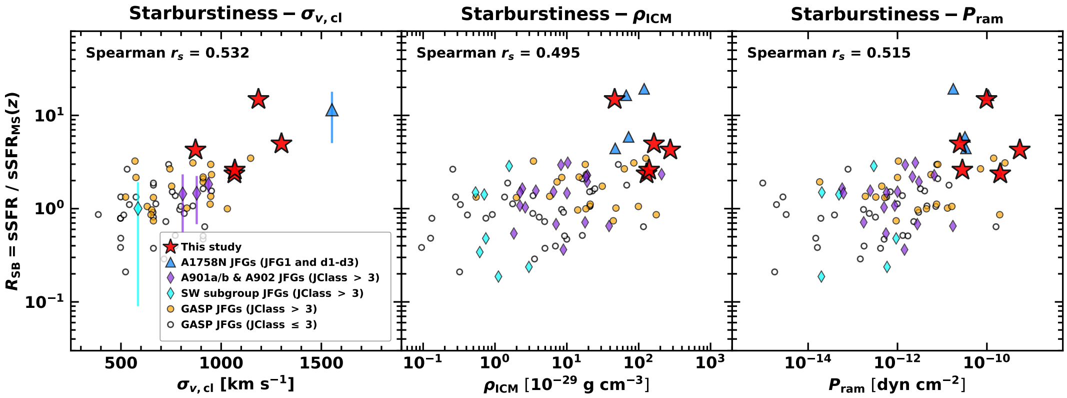

Figure 4.5. Starburstiness (R_{SB}) of jellyfish galaxies as a function of cluster velocity dispersion ($\sigma_{v,\mathrm{cl}}$; left), the ICM density (ρ_{ICM}; middle), and the degree of ram pressure (P_{ram}; right). Error bars in the left panel represent standard deviations of starburstiness of jellyfish galaxies in the same host clusters. We plot the data of jellyfish samples with strong RPS signatures as described in **Figure 4.3**. The Spearman's rank correlation coefficients are shown at the top of each panel.

the strength of ram pressure (right panel). For all the panels, we plot the starburstiness of our sample (star symbols) in addition to the GASP (circles), RO19 (diamonds), and EK19 (triangles) sample with strong RPS signature (JClass > 3) This selection allows us to compare the star formation activity of jellyfish galaxies with similar morphological classes.

In the left panel, the starburstiness of the GASP and RO19 samples with JClass > 3 does not seem to have a clear correlation with the cluster velocity dispersion. However, we note that there is a positive correlation between R_{SB} and $\sigma_{v,\mathrm{cl}}$ by adding the data of our sample and the A1758N sample in massive clusters ($\sigma_{v,\mathrm{cl}} \gtrsim 1000$ km s^{-1}). The Spearman's rank correlation coefficient (r_s) is 0.532 (p-value $= 3.4 \times 10^{-5}$), indicating that this correlation is reliable. In the middle and right panels, this trend similarly appears in the relations of R_{SB} vs. ρ_{ICM} ($r_s = 0.50$ and p-value $= 1.4 \times 10^{-4}$) and R_{SB} vs. P_{ram} ($r_s = 0.51$ and p-value $= 8.0 \times 10^{-5}$) because the cluster velocity dispersion is closely related to the ICM density and the strength of ram pressure as described in

Section 4.3.3.

These results imply that the star formation activity of the jellyfish galaxies with similar morphological classes has positive correlations with the host cluster velocity dispersion and the degree of RPS. Furthermore, these correlations can be more strengthened considering that the starburstiness of our sample and EK19 sample might be underestimated due to possible suppression of SFRs of the SFMS in the cluster central region (Paccagnella et al. 2016). In the previous literature, Gullieuszik et al. (2020) pointed out that the star formation activity of the GASP jellyfish galaxies hardly shows remarkable relations with the cluster velocity dispersion. However, the reliable correlations between star formation activity and RPS could be found in this work thanks to the data of jellyfish galaxies in clusters more massive ($\sigma_{v,\mathrm{cl}} \gtrsim 1000$ km s^{-1}) than those in the GASP and RO19 studies. We interpret that this relation clearly shows the short-term effect of RPS on the star formation activity of jellyfish galaxies in clusters. Although it is expected that stronger RPS will eventually strip the gas of cluster galaxies, it could trigger the star formation activity more strongly in jellyfish galaxies instead.

4.6 Summary

In this study, we investigate the relation between the star formation activity of jellyfish galaxies and their host cluster properties. We use the Gemini GMOS/IFU observations of five extreme jellyfish galaxies in the MACS clusters and Abell 2744 at $z > 0.3$ for our study. We computed Hα-based SFRs and compared them to those from the GASP, RO19, and EK19 samples using the SFR$-M_*$ and phase-space diagrams. We summarize our results as follows.

1. In the SFR$-M_*$ and SFR$-\sigma_{v,\mathrm{cl}}$ diagrams, the total SFRs, tail SFRs, and f_{SFR}(tail) of the five jellyfish galaxies are an order of magnitude higher than those of the GASP jellyfish galaxies. Combining our data and the GASP results, the SFRs and f_{SFR} of jellyfish galaxies tend to increase as the stellar mass and cluster velocity

dispersion increase.

2. The projected phase-space diagrams of the combined sample of the GASP survey, RO19, EK19, and ours indicate that jellyfish galaxies with strong RPS signatures (JClass > 3) show more enhanced star formation activity compared to those with weak RPS signatures (JClass ≤ 3).

3. In the SFR-M_* diagram, our sample and the EK19 sample are located above the SFMS at their median redshifts. The SFR excess of our sample and the EK19 sample (massive clusters) is also higher than that of the GASP and RO19 sample (low-mass clusters), implying that the star formation activity of jellyfish galaxies in massive clusters is more enhanced.

4. Combining all the jellyfish galaxies with strong RPS features, we find that starbustiness correlates positively with the cluster velocity dispersion, ICM density, and strength of ram pressure. This implies that jellyfish galaxies show more enhanced star formation activity with increasing host cluster mass and degree of ram pressure.

Chapter 5

Summary and Conclusion

In this thesis, we investigated the environmental effects on the observational properties of UDGs and jellyfish galaxies in massive galaxy clusters. The formation and evolution of these two galaxy populations are closely involved with RPS or tidal interactions, which are the most significant environmental effects in cluster environments. Massive galaxy clusters tend to have a much stronger RPS effect than low-mass clusters. Thus, rich and massive clusters are ideal laboratories to explore the influence of RPS on the galaxy properties of UDGs and jellyfish galaxies.

For these scientific goals, we detected UDGs and jellyfish galaxies in the HFF and MACS clusters at intermediate redshifts and studied their observational properties with imaging and spectroscopic data. We used very deep and high-resolution *HST* images of the three HFF clusters (Abell 370, Abell S1063, and Abell 2744) to study UDGs in massive clusters. We also obtained GMOS/IFU data of five jellyfish galaxies in the MACS clusters and Abell 2744 at $z > 0.3$ to understand the role of RPS on jellyfish galaxies.

In Chapter 2, we detected UDGs in Abell 370 and investigated their properties by combining UDGs in two other massive HFF clusters, Abell 2744 and Abell S1063. We found 46 UDGs and 112 LSB dwarfs in the HST fields of Abell 370. Their CMDs show that most UDGs are located in the low-luminosity end of the red sequence, while a few UDGs show blue colors. Composite RDPs of the UDGs show a flattening in the central region of the HFF clusters, in contrast to those of bright galaxies. This discrepancy means that a considerable fraction of UDGs might have been tidally disrupted in the central region of the clusters. We investigated the relation between the number of UDGs and the virial mass of their host systems. We obtained a power-law relation between the UDG abundance ($N(\mathrm{UDG})$) and the masses of their hosts (M_{200}) with a slope close to one: $N(\mathrm{UDG}) \propto M_{200}^{1.00\pm0.05}$. This relation implies that the survival efficiency of UDGs is not dependent on the masses of their host systems. We estimated the virial masses (M_{200}) of the UDGs with the fundamental manifold method, finding that most UDGs have dwarf-like masses with $M_{200} = 10^{10} - 10^{11}\ M_{\odot}$. From these results, we concluded that UDGs in massive clusters are similar to those in the low-mass clusters in the local universe.

In **Chapter 3**, we presented a GMOS/IFU study of five jellyfish galaxies in the MACS clusters and Abell 2744 at $z > 0.3$. The Hα flux distributions are spatially consistent with stellar emission in all jellyfish galaxies. BPT diagrams show that these jellyfish galaxies show various gas ionization mechanisms such as photoionization, AGN, and mixed effects. The radial velocity distributions of ionized gas seem to follow disk rotation of galaxies, with the appearance of a few high-velocity components in the tails as a sign of RPS. Mean gas velocity dispersion is lower than 50 km s^{-1} in most star-forming regions, which implies that the ionized gas in those regions is dynamically cold. In the projected phase-space diagrams, the jellyfish galaxies in this study are located in the inner region with a wide range of orbital velocities relative to the cluster center. Combining the GASP sample and our sample, we find that jellyfish galaxies with higher stellar masses and higher host cluster velocity dispersions are more likely to be located in the inner region of the clusters with more enhanced star formation activity.

In **Chapter 4**, we performed a more detailed analysis of the relationship between the star formation activity of jellyfish galaxies and their host cluster properties. We compared the star formation activity of jellyfish galaxies with Hα-derived SFRs of the samples from the GASP survey, Abell 901/2, and Abell 1758N. The SFRs and the tail SFR fraction of jellyfish galaxies tend to increase as the stellar mass and cluster velocity dispersion increase. The projected phase-space diagrams of the combined sample of jellyfish galaxies indicate that jellyfish galaxies with strong RPS signatures show more enhanced star formation activity compared to those with weak RPS signatures. The SFR-M_* diagram shows that jellyfish galaxies in massive clusters are located above the SFMS at their median redshifts. Combining all the jellyfish galaxies with strong RPS features, we find that starbustiness correlates positively with the cluster velocity dispersion, ICM density, and strength of ram pressure.

In conclusion, we summarize our results from the studies on UDGs and jellyfish galaxies. UDGs in massive clusters behave like dwarf galaxies, implying that UDGs are an extreme version of dwarf galaxies. UDGs in cluster environments can undergo environmental effects such as RPS and tidal disruption, as consistently shown in massive and low-mass clusters. Jellyfish galaxies also show similar ionized-gas properties in high-mass and low-mass clusters. However, their star formation activity is more strongly triggered in massive clusters due to high ram pressure.

We can picture the overall evolutionary tracks of UDGs and jellyfish galaxies with our results. The progenitors of UDGs might be gas-rich dwarf galaxies or disk galaxies, but their gas can be stripped by RPS or tidal interactions in clusters. Throughout these processes, gas-deficient UDGs can form and evolve in clusters, which is similar to early-type dwarf galaxies. Jellyfish galaxies are short-lived RPS galaxies showing a snapshot of the starburst phase during RPS. Thus, jellyfish galaxies show star formation activity for several hundred Myrs, with the SFR dependent on the strength of ram pressure from host clusters. After jellyfish galaxies consume gas with star formation, they evolve into post-starburst galaxies or quiescent disk galaxies in clusters. These evolutionary tracks of both UDGs and jellyfish galaxies are closely related to environmental effects.

Bibliography

Abolfathi, B., Aguado, D. S., Aguilar, G., et al. 2018, ApJS, 235, 42

Afanasiev, A. V., Chilingarian, I. V., Mieske, S., et al. 2018, MNRAS, 477, 4856

Ahn, C. P., Seth, A. C., den Brok, M., et al. 2017, ApJ, 839, 72

Ahn, C. P., Seth, A. C., Cappellari, M., et al. 2018, ApJ, 858, 102

Alabi, A., Ferré-Mateu, A., Romanowsky, A. J., et al. 2018, MNRAS, 479, 3308

Amorisco, N. C., & Loeb, A. 2016, MNRAS, 459, L51

Amorisco, N. C., Monachesi, A., Agnello, A., & White, S. D. M. 2018, MNRAS, 475, 4235

Arrigoni Battaia, F., Gavazzi, G., Fumagalli, M., et al. 2012, A&A, 543, A112

Baldwin, J. A., Phillips, M. M., & Terlevich, R. 1981, PASP, 93, 5

Bamford, S. P., Nichol, R. C., Baldry, I. K., et al. 2009, MNRAS, 393, 1324

Baushev, A. N. 2018, , 60, 69

Beasley, M. A., Romanowsky, A. J., Pota, V., et al. 2016, ApJ, 819, L20

Beasley, M. A., & Trujillo, I. 2016, ApJ, 830, 23

Bekki, K. & Couch, W. J. 2003, ApJ, 596, L13

Bekki, K., Couch, W. J., Drinkwater, M. J., et al. 2003, MNRAS, 344, 399

Bekki, K. 2009, MNRAS, 399, 2221

Bekki, K., Owers, M. S., & Couch, W. J. 2010, ApJ, 718, L27.

Bellhouse, C., Jaffé, Y. L., Hau, G. K. T., et al. 2017, ApJ, 844, 49

Bellhouse, C., Jaffé, Y. L., McGee, S. L., et al. 2019, MNRAS, 485, 1157

Bellazzini, M., Belokurov, V., Magrini, L., et al. 2017, MNRAS, 467, 3751

Bender, R., Burstein, D., & Faber, S. M. 1993, ApJ, 411, 153

Bennet, P., Sand, D. J., Zaritsky, D., et al. 2018, ApJ, 866, L11

Bertin, E., & Arnouts, S. 1996, A&AS, 117, 393

Boehringer, H., Neumann, D. M., Schindler, S., et al. 1996, ApJ, 467, 168

Boschin, W., Girardi, M., Spolaor, M., et al. 2006, A&A, 449, 461

Boselli, A. & Gavazzi, G. 2006, PASP, 118, 517

Boselli, A., Cuillandre, J. C., Fossati, M., et al. 2016, A&A, 587, A68

Boselli, A., Epinat, B., Contini, T., et al. 2019, A&A, 631, A114

Boselli, A., Fossati, M., & Sun, M. 2021, arXiv:2109.13614

Bradley L., et al., 2019, astropy/photutils: v1.0.2, doi:10.5281/zenodo.2533376

Broadhurst, T., Umetsu, K., Medezinski, E., Oguri, M., & Rephaeli, Y. 2008, ApJ, 685, L9

Bruzual, G., & Charlot, S. 2003, MNRAS, 344, 1000

Byrd, G. & Valtonen, M. 1990, ApJ, 350, 89

Caldwell, N., & Bothun, G. D. 1987, AJ, 94, 1126

Cano-Díaz, M., Ávila-Reese, V., Sánchez, S. F., et al. 2019, MNRAS, 488, 3929

Cappellari, M. & Copin, Y. 2003, MNRAS, 342, 345

Cardelli, J. A., Clayton, G. C., & Mathis, J. S. 1989, ApJ, 345, 245

Carleton, T., Errani, R., Cooper, M., et al. 2019, MNRAS, 485, 382

Castignani, G., Combes, F., & Salomé, P. 2020, A&A, 635, L10

Chabrier, G. 2003, PASP, 115, 763

Chan, T. K., Kereš, D., Wetzel, A., et al. 2018, MNRAS, 478, 906

Chilingarian, I. V., Mieske, S., Hilker, M., et al. 2011, MNRAS, 412, 1627

Chilingarian, I. V., Afanasiev, A. V., Grishin, K. A., et al. 2019, ApJ, 884, 79

Chung, A., van Gorkom, J. H., Kenney, J. D. P., et al. 2009, AJ, 138, 1741

Cohen, Y., van Dokkum, P., Danieli, S., et al. 2018, ApJ, 868, 96

Collins, M. L. M., Chapman, S. C., Rich, R. M., et al. 2013, ApJ, 768, 172

Collins, M. L. M., Tollerud, E. J., Rich, R. M., et al. 2019, MNRAS, 2833

Conselice, C. J., Gallagher, J. S., & Wyse, R. F. G. 2003, AJ, 125, 66

Conselice, C. J. 2018, Research Notes of the American Astronomical Society, 2, 43

Consolandi, G., Gavazzi, G., Fossati, M., et al. 2017, A&A, 606, A83

Cortese, L., Marcillac, D., Richard, J., et al. 2007, MNRAS, 376, 157

Cowie, L. L. & Songaila, A. 1977, Nature, 266, 501

Cramer, W. J., Kenney, J. D. P., Sun, M., et al. 2019, ApJ, 870, 63

Crnojević, D., Sand, D. J., Spekkens, K., et al. 2016, ApJ, 823, 19

Di Cintio, A., Brook, C. B., Dutton, A. A., et al. 2017, MNRAS, 466, L1

Dressler, A. 1980, ApJ, 236, 351

Dressler, A. 1984, ARA&A, 22, 185

Drinkwater, M. J., Jones, J. B., Gregg, M. D., et al. 2000, PASA, 17, 227

Durret, F., Chiche, S., Lobo, C., et al. 2021, A&A, 648, A63

Ebeling, H., Edge, A. C., Bohringer, H., et al. 1998, MNRAS, 301, 881

Ebeling, H., Edge, A. C., & Henry, J. P. 2001, ApJ, 553, 668

Ebeling, H., Barrett, E., Donovan, D., et al. 2007, ApJ, 661, L33

Ebeling, H., Edge, A. C., Mantz, A., et al. 2010, MNRAS, 407, 83

Ebeling, H., Stephenson, L. N., & Edge, A. C. 2014, ApJ, 781, L40

Ebeling, H., Qi, J., & Richard, J. 2017, MNRAS, 471, 3305

Ebeling, H. & Kalita, B. S. 2019, ApJ, 882, 127

Elbaz, D., Dickinson, M., Hwang, H. S., et al. 2011, A&A, 533, A119

Eskew, M., Zaritsky, D., & Meidt, S. 2012, AJ, 143, 139

Evrard, A. E., Bialek, J., Busha, M., et al. 2008, ApJ, 672, 122

Fabian, A. C. & Nulsen, P. E. J. 1977, MNRAS, 180, 479

Fabian, A. C. 1994, ARA&A, 32, 277

Fellhauer, M. & Kroupa, P. 2002, MNRAS, 330, 642

Ferré-Mateu, A., Alabi, A., Forbes, D. A., et al. 2018, MNRAS, 479, 4891

Finner, K., HyeongHan, K., Jee, M. J., et al. 2021, ApJ, 918, 72

Foreman-Mackey, D., Hogg, D. W., Lang, D., et al. 2013, PASP, 125, 306

Fossati, M., Fumagalli, M., Boselli, A., et al. 2016, MNRAS, 455, 2028

Fujita, Y. & Nagashima, M. 1999, ApJ, 516, 619

Fumagalli, M., Fossati, M., Hau, G. K. T., et al. 2014, MNRAS, 445, 4335

Geha, M., Blanton, M. R., Masjedi, M., & West, A. A. 2006, ApJ, 653, 240

Golovich, N., Dawson, W. A., Wittman, D. M., et al. 2019, ApJS, 240, 39

Golovich, N., Dawson, W. A., Wittman, D. M., et al. 2019, ApJ, 882, 69

Gómez, P. L., Nichol, R. C., Miller, C. J., et al. 2003, ApJ, 584, 210

Greco, J. P., Greene, J. E., Strauss, M. A., et al. 2018a, ApJ, 857, 104

Greco, J. P., Goulding, A. D., Greene, J. E., et al. 2018b, ApJ, 866, 112

Greener, M. J., Aragón-Salamanca, A., Merrifield, M. R., et al. 2020, MNRAS, 495, 2305

Grishin, K. A., Chilingarian, I. V., Afanasiev, A. V., et al. 2021, Nature Astronomy, 5, 1308

Gu, M., Conroy, C., Law, D., et al. 2018, ApJ, 859, 37

Gullieuszik, M., Poggianti, B. M., McGee, S. L., et al. 2020, ApJ, 899, 13

Gunawardhana, M. L. P., Hopkins, A. M., Sharp, R. G., et al. 2011, MNRAS, 415, 1647

Gunn, J. E. & Gott, J. R. 1972, ApJ, 176, 1

Harris, W. E. 2010, arXiv e-prints, arXiv:1012.3224

Harris, W. E., Blakeslee, J. P., & Harris, G. L. H. 2017, ApJ, 836, 67

Hester, J. A., Seibert, M., Neill, J. D., et al. 2010, ApJ, 716, L14

Hilker, M., Infante, L., Vieira, G., et al. 1999, A&AS, 134, 75

Hogg, D. W., Blanton, M. R., Brinchmann, J., et al. 2004, ApJ, 601, L29

Hopkins, A. M., Miller, C. J., Nichol, R. C., et al. 2003, ApJ, 599, 971

Illingworth, G. D., Magee, D., Oesch, P. A., et al. 2013, ApJS, 209, 6

Impey, C., Bothun, G., & Malin, D. 1988, ApJ, 330, 634

Jáchym, P., Kenney, J. D. P., Sun, M., et al. 2019, ApJ, 883, 145

Jaffé, Y. L., Smith, R., Candlish, G. N., et al. 2015, MNRAS, 448, 1715

Jaffé, Y. L., Poggianti, B. M., Moretti, A., et al. 2018, MNRAS, 476, 4753

Janssens, S., Abraham, R., Brodie, J., et al. 2017, ApJ, 839, L17

Janssens, S. R., Abraham, R., Brodie, J., et al. 2019, ApJ, 887, 92

Jarrett, T. H., Cohen, M., Masci, F., et al. 2011, ApJ, 735, 112

Kadowaki, J., Zaritsky, D., & Donnerstein, R. L. 2017, ApJ, 838, L21

Kalita, B. S. & Ebeling, H. 2019, ApJ, 887, 158

Kapferer, W., Sluka, C., Schindler, S., et al. 2009, A&A, 499, 87

Kashibadze, O. G., Karachentsev, I. D., & Karachentseva, V. E. 2020, A&A, 635, A135

Kauffmann, G., Heckman, T. M., Tremonti, C., et al. 2003, MNRAS, 346, 1055

Kenney, J. D. P., Geha, M., Jáchym, P., et al. 2014, ApJ, 780, 119

Kennicutt, R. C. 1998, ARA&A, 36, 189

Kennicutt, R. C. & Evans, N. J. 2012, ARA&A, 50, 531

Kewley, L. J., Dopita, M. A., Sutherland, R. S., et al. 2001, ApJ, 556, 121

Koda, J., Yagi, M., Yamanoi, H., & Komiyama, Y. 2015, ApJ, 807, L2

Kronberger, T., Kapferer, W., Ferrari, C., et al. 2008, A&A, 481, 337

Kubo, J. M., Stebbins, A., Annis, J., et al. 2007, ApJ, 671, 1466

Lagattuta, D. J., Richard, J., Clément, B., et al. 2017, MNRAS, 469, 3946

Larson, R. B., Tinsley, B. M., & Caldwell, C. N. 1980, ApJ, 237, 692

Lee, N., Sanders, D. B., Casey, C. M., et al. 2015, ApJ, 801, 80

Lee, M. G. & Jang, I. S. 2016, ApJ, 819, 77

Lee, M. G., Kang, J., Lee, J. H., & Jang, I. S. 2017, ApJ, 844, 157

Leisman, L., Haynes, M. P., Janowiecki, S., et al. 2017, ApJ, 842, 133

Lewis, I., Balogh, M., De Propris, R., et al. 2002, MNRAS, 334, 673

Lim, S., Peng, E. W., Côté, P., et al. 2018, ApJ, 862, 82

Liu, Q., Yee, H. K. C., Drissen, L., et al. 2021, ApJ, 908, 228

Lotz, J. M., Koekemoer, A., Coe, D., et al. 2017, ApJ, 837, 97

Mamon, G. A., Biviano, A., & Murante, G. 2010, A&A, 520, A30

Mancera Piña, P. E., Peletier, R. F., Aguerri, J. A. L., et al. 2018, MNRAS, 481, 4381

Mancera Piña, P. E., Aguerri, J. A. L., Peletier, R. F., et al. 2019, MNRAS, 485, 1036

Mann, A. W. & Ebeling, H. 2012, MNRAS, 420, 2120

Martínez-Delgado, D., Läsker, R., Sharina, M., et al. 2016, AJ, 151, 96

Martín-Navarro, I., Romanowsky, A. J., Brodie, J. P., et al. 2019, MNRAS, 484, 3425

McConnachie, A. W. 2012, AJ, 144, 4

McLaughlin, D. E., & van der Marel, R. P. 2005, ApJS, 161, 304

McPartland, C., Ebeling, H., Roediger, E., et al. 2016, MNRAS, 455, 2994

Medezinski, E., Battaglia, N., Umetsu, K., et al. 2018, PASJ, 70, S28

Medling, A. M., Cortese, L., Croom, S. M., et al. 2018, MNRAS, 475, 5194

Merluzzi, P., Busarello, G., Dopita, M. A., et al. 2013, MNRAS, 429, 1747

Merritt, D. 1983, ApJ, 264, 24

Merritt, D. 1985, ApJ, 289, 18

Merritt, A., van Dokkum, P., Danieli, S., et al. 2016, ApJ, 833, 168

Mieske, S., Hilker, M., Jordán, A., et al. 2008, A&A, 487, 921

Mihos, J. C., Durrell, P. R., Ferrarese, L., et al. 2015, ApJ, 809, L21

Mihos, J. C., Harding, P., Feldmeier, J. J., et al. 2017, ApJ, 834, 16

Moore, B., Katz, N., Lake, G., et al. 1996, Nature, 379, 613

Moore, B., Lake, G., & Katz, N. 1998, ApJ, 495, 139

Moretti, A., Radovich, M., Poggianti, B. M., et al. 2022, ApJ, 925, 4

Morrissey, P., Conrow, T., Barlow, T. A., et al. 2007, ApJS, 173, 682

Müller, O., Jerjen, H., & Binggeli, B. 2018, A&A, 615, A105

Munari, E., Biviano, A., Borgani, S., et al. 2013, MNRAS, 430, 2638

Mun, J. Y., Hwang, H. S., Lee, M. G., et al. 2021, Journal of Korean Astronomical Society, 54, 17

Muñoz, R. P., Eigenthaler, P., Puzia, T. H., et al. 2015, ApJ, 813, L15

Nulsen, P. E. J. 1982, MNRAS, 198, 1007

Ordenes-Briceño, Y., Eigenthaler, P., Taylor, M. A., et al. 2018, ApJ, 859, 52

Osato, K., Shirasaki, M., Miyatake, H., et al. 2020, MNRAS, 492, 4780

Ostriker, J. P. & Hausman, M. A. 1977, ApJ, 217, L125

Owen, F. N., Keel, W. C., Wang, Q. D., et al. 2006, AJ, 131, 1974

Owers, M. S., Randall, S. W., Nulsen, P. E. J., et al. 2011, ApJ, 728, 27

Owers, M. S., Couch, W. J., Nulsen, P. E. J., et al. 2012, ApJ, 750, L23

Paccagnella, A., Vulcani, B., Poggianti, B. M., et al. 2016, ApJ, 816, L25

Pandya, V., Mulchaey, J., & Greene, J. E. 2016, ApJ, 819, 162

Pandya, V., Romanowsky, A. J., Laine, S., et al. 2018, ApJ, 858, 29

Papastergis, E., Adams, E. A. K., & Romanowsky, A. J. 2017, A&A, 601, L10

Peacock, M. B., Maccarone, T. J., Knigge, C., et al. 2010, MNRAS, 402, 803

Pedrini, A., Fossati, M., Gavazzi, G., et al. 2022, MNRAS, 511, 5180

Peng, C. Y., Ho, L. C., Impey, C. D., & Rix, H.-W. 2010, AJ, 139, 2097

Peng, E. W., & Lim, S. 2016, ApJ, 822, L31

Pfeffer, J. & Baumgardt, H. 2013, MNRAS, 433, 1997

Phillipps, S., Drinkwater, M. J., Gregg, M. D., et al. 2001, ApJ, 560, 201

Pizagno, J., Prada, F., Weinberg, D. H., et al. 2007, AJ, 134, 945

Planck Collaboration, Ade, P. A. R., Aghanim, N., et al. 2016, A&A, 594, A27

Poggianti, B. M., Fasano, G., Omizzolo, A., et al. 2016, AJ, 151, 78

Poggianti, B. M., Moretti, A., Gullieuszik, M., et al. 2017, ApJ, 844, 48

Poggianti, B. M., Gullieuszik, M., Tonnesen, S., et al. 2019, MNRAS, 482, 4466

Postman, M. & Geller, M. J. 1984, ApJ, 281, 95

Rawle, T. D., Altieri, B., Egami, E., et al. 2014, MNRAS, 442, 196

Repp, A. & Ebeling, H. 2018, MNRAS, 479, 844

Rhee, J., Smith, R., Choi, H., et al. 2017, ApJ, 843, 128

Rich, J. A., Kewley, L. J., & Dopita, M. A. 2011, ApJ, 734, 87

Richard, J., Claeyssens, A., Lagattuta, D., et al. 2021, A&A, 646, A83

Roberts, I. D. & Parker, L. C. 2020, MNRAS, 495, 554

Roediger, E., Bruggen, M., Owers, M. S., et al. 2014, MNRAS, 443, L114

Román, J., & Trujillo, I. 2017a, MNRAS, 468, 703

Román, J., & Trujillo, I. 2017b, MNRAS, 468, 4039

Román, J., Beasley, M. A., Ruiz-Lara, T., et al. 2019, MNRAS, 486, 823

Roman-Oliveira, F. V., Chies-Santos, A. L., Rodríguez del Pino, B., et al. 2019, MNRAS, 484, 892

Rong, Y., Guo, Q., Gao, L., et al. 2017, MNRAS, 470, 4231

Rykoff, E. S., Rozo, E., Busha, M. T., et al. 2014, ApJ, 785, 104

Salpeter, E. E. 1955, ApJ, 121, 161

Sandage, A. 1972a, ApJ, 178, 1

Sandage, A. 1972b, ApJ, 173, 485

Sandage, A., & Binggeli, B. 1984, AJ, 89, 919

Schlafly, E. F. & Finkbeiner, D. P. 2011, ApJ, 737, 103

Seo, G., Sohn, J., & Lee, M. G. 2020, ApJ, 903, 130

Sereno, M. & Ettori, S. 2017, MNRAS, 468, 3322

Seth, A. C., van den Bosch, R., Mieske, S., et al. 2014, Nature, 513, 398

Sharp, R. G. & Bland-Hawthorn, J. 2010, ApJ, 711, 818

Sheen, Y.-K., Smith, R., Jaffé, Y., et al. 2017, ApJ, 840, L7

Shi, D. D., Zheng, X. Z., Zhao, H. B., et al. 2017, ApJ, 846, 26

Shipley, H. V., Lange-Vagle, D., Marchesini, D., et al. 2018, ApJS, 235, 14

Sifón, C., van der Burg, R. F. J., Hoekstra, H., Muzzin, A., & Herbonnet, R. 2018, MNRAS, 473, 3747

Simon, J. D., & Geha, M. 2007, ApJ, 670, 313

Smith, R. J., Lucey, J. R., Hammer, D., et al. 2010, MNRAS, 408, 1417

Sohn, J., Geller, M. J., Zahid, H. J., et al. 2017, ApJS, 229, 20

Speagle, J. S., Steinhardt, C. L., Capak, P. L., et al. 2014, ApJS, 214, 15

Spekkens, K., & Karunakaran, A. 2018, ApJ, 855, 28

Springob, C. M., Masters, K. L., Haynes, M. P., Giovanelli, R., & Marinoni, C. 2007, ApJS, 172, 599

Steinhardt, C. L., Jauzac, M., Acebron, A., et al. 2020, ApJS, 247, 64

Steinhauser, D., Haider, M., Kapferer, W., et al. 2012, A&A, 544, A54

Stott, J. P., Swinbank, A. M., Johnson, H. L., et al. 2016, MNRAS, 457, 1888

Struble, M. F., & Rood, H. J. 1999, ApJS, 125, 35

Toloba, E., Sand, D. J., Spekkens, K., et al. 2016, ApJ, 816, L5

Toloba, E., Lim, S., Peng, E., et al. 2018, ApJ, 856, L31

Toomre, A. & Toomre, J. 1972, ApJ, 178, 623

Trujillo, I., Roman, J., Filho, M., & Sánchez Almeida, J. 2017, ApJ, 836, 191

Umetsu, K., Broadhurst, T., Zitrin, A., Medezinski, E., & Hsu, L.-Y. 2011, ApJ, 729, 127

Umetsu, K., Sereno, M., Tam, S.-I., et al. 2018, ApJ, 860, 104

van der Burg, R. F. J., Muzzin, A., & Hoekstra, H. 2016, A&A, 590, A20 van der Burg, R. F. J., Hoekstra, H., Muzzin, A., et al. 2017, A&A, 607, A79

van Dokkum, P. G., Abraham, R., Merritt, A., et al. 2015, ApJ, 798, L45

van Dokkum, P., Abraham, R., Brodie, J., et al. 2016, ApJ, 828, L6

van Dokkum, P., Abraham, R., Romanowsky, A. J., et al. 2017, ApJ, 844, L11

van Dokkum, P., Wasserman, A., Danieli, S., et al. 2019, ApJ, 880, 91

Venhola, A., Peletier, R., Laurikainen, E., et al. 2017, A&A, 608, A142

Voges, W., Aschenbach, B., Boller, T., et al. 1999, A&A, 349, 389

Vollmer, B., Cayatte, V., Balkowski, C., et al. 2001, ApJ, 561, 708

Vulcani, B., Poggianti, B. M., Finn, R. A., et al. 2010, ApJ, 710, L1

Vulcani, B., Poggianti, B. M., Gullieuszik, M., et al. 2018, ApJ, 866, L25

Vulcani, B., Poggianti, B. M., Smith, R., et al. 2022, ApJ, 927, 91

Weinzirl, T., Aragón-Salamanca, A., Gray, M. E., et al. 2017, MNRAS, 471, 182

Whitmore, B. C., Gilmore, D. M., & Jones, C. 1993, ApJ, 407, 489

Wittmann, C., Lisker, T., Ambachew Tilahun, L., et al. 2017, MNRAS, 470, 1512

Woudt, P. A., Kraan-Korteweg, R. C., Lucey, J., et al. 2008, MNRAS, 383, 445

Wright, E. L., Eisenhardt, P. R. M., Mainzer, A. K., et al. 2010, AJ, 140, 1868

Yagi, M., Yoshida, M., Komiyama, Y., et al. 2010, AJ, 140, 1814

Yagi, M., Koda, J., Komiyama, Y., & Yamanoi, H. 2016, ApJS, 225, 11

Yoshida, M., Yagi, M., Komiyama, Y., et al. 2012, ApJ, 749, 43

Yozin, C., & Bekki, K. 2015, MNRAS, 452, 937

Yun, K., Pillepich, A., Zinger, E., et al. 2019, MNRAS, 483, 1042

Zaritsky, D., Gonzalez, A. H., & Zabludoff, A. I. 2006a, ApJ, 638, 725

Zaritsky, D., Gonzalez, A. H., & Zabludoff, A. I. 2006b, ApJ, 642, L37

Zaritsky, D., Zabludoff, A. I., & Gonzalez, A. H. 2008, ApJ, 682, 68

Zaritsky, D., Colucci, J. E., Pessev, P. M., et al. 2012, ApJ, 761, 93

Zaritsky, D., Colucci, J. E., Pessev, P. M., et al. 2013, ApJ, 770, 121

Zaritsky, D., Colucci, J. E., Pessev, P. M., et al. 2014, ApJ, 796, 71

Zaritsky, D. 2017, MNRAS, 464, L110

Zenteno, A., Mohr, J. J., Desai, S., et al. 2016, MNRAS, 462, 830

Zhang, Y.-Y., Andernach, H., Caretta, C. A., et al. 2011, A&A, 526, A105

Appendix A

Catalogs of UDGs and LSB Dwarfs in Abell 370

A.1 UDGs in the Central Field of Abell 370

A.2 UDGs in the Parallel Field of Abell 370

A.3 LSB Dwarfs in the Central Field of Abell 370

A.4 LSB Dwarfs in the Parallel Field of Abell 370

Table A.1. A Catalog of UDGs in the Central Field of Abell 370

Name	R.A. (J2000)	Decl. (J2000)	$F814W$	$F814W - F105W$	$R_{\mathrm{eff,c}}{}^{a}$ [kpc]	$\langle\mu\rangle_{\mathrm{e,abs}}(r')^{b}$ [mag arcsec^{-2}]	n	b/a
UDG-C01	39.94771	−1.58373	25.18 ± 0.01	0.22 ± 0.01	1.78 ± 0.11	23.96 ± 0.08	1.25 ± 0.12	0.81 ± 0.03
UDG-C02	39.94916	−1.58248	23.90 ± 0.01	-0.07 ± 0.01	2.82 ± 0.02	24.01 ± 0.02	0.53 ± 0.02	0.50 ± 0.00
UDG-C03	39.94958	−1.58445	25.17 ± 0.01	0.21 ± 0.01	1.64 ± 0.08	24.01 ± 0.07	0.80 ± 0.08	0.87 ± 0.03
UDG-C04	39.95016	−1.57992	26.23 ± 0.03	0.20 ± 0.02	1.94 ± 0.19	24.98 ± 0.14	1.20 ± 0.20	0.76 ± 0.05
UDG-C05	39.95378	−1.57341	24.81 ± 0.01	0.45 ± 0.01	1.90 ± 0.06	24.07 ± 0.05	0.62 ± 0.04	0.35 ± 0.01
UDG-C06	39.95519	−1.56997	25.69 ± 0.02	0.13 ± 0.01	1.63 ± 0.09	24.31 ± 0.09	0.64 ± 0.07	0.66 ± 0.03
UDG-C07	39.95963	−1.59164	25.11 ± 0.01	0.22 ± 0.01	1.77 ± 0.08	24.07 ± 0.07	0.71 ± 0.07	0.57 ± 0.02
UDG-C08	39.96002	−1.56734	25.57 ± 0.02	0.06 ± 0.01	1.56 ± 0.08	24.20 ± 0.08	0.89 ± 0.11	0.56 ± 0.02
UDG-C09	39.96030	−1.57025	24.55 ± 0.01	0.24 ± 0.01	2.26 ± 0.08	24.02 ± 0.05	0.73 ± 0.05	0.80 ± 0.02
UDG-C10	39.96300	−1.56976	24.90 ± 0.01	0.18 ± 0.01	2.28 ± 0.13	24.08 ± 0.09	1.31 ± 0.11	0.64 ± 0.02
UDG-C11	39.96416	−1.58529	25.23 ± 0.01	0.21 ± 0.01	1.95 ± 0.10	24.27 ± 0.07	0.97 ± 0.10	0.73 ± 0.03
UDG-C12	39.96416	−1.55755	26.24 ± 0.02	0.15 ± 0.02	2.02 ± 0.34	24.95 ± 0.30	1.91 ± 0.34	0.77 ± 0.08
UDG-C13	39.96655	−1.57844	25.52 ± 0.02	0.17 ± 0.02	1.94 ± 0.06	24.62 ± 0.06	0.34 ± 0.03	0.34 ± 0.01
UDG-C14	39.97001	−1.55845	25.46 ± 0.02	0.22 ± 0.01	1.57 ± 0.06	24.30 ± 0.06	0.58 ± 0.04	0.62 ± 0.02
UDG-C15	39.97003	−1.56770	25.79 ± 0.02	0.23 ± 0.02	1.70 ± 0.14	24.50 ± 0.10	0.92 ± 0.11	0.57 ± 0.03
UDG-C16	39.97215	−1.59249	25.62 ± 0.01	0.26 ± 0.01	1.85 ± 0.28	24.14 ± 0.30	2.71 ± 0.37	0.61 ± 0.05
UDG-C17	39.97284	−1.56010	26.57 ± 0.03	0.25 ± 0.03	1.54 ± 0.13	24.85 ± 0.13	0.76 ± 0.14	0.75 ± 0.06
UDG-C18	39.97305	−1.58762	24.87 ± 0.01	0.31 ± 0.01	2.62 ± 0.08	24.33 ± 0.04	0.69 ± 0.05	0.53 ± 0.01
UDG-C19	39.97485	−1.58816	25.31 ± 0.01	0.30 ± 0.01	1.64 ± 0.11	23.82 ± 0.12	1.83 ± 0.20	0.81 ± 0.04
UDG-C20	39.97550	−1.59880	25.84 ± 0.02	0.01 ± 0.02	1.64 ± 0.16	24.48 ± 0.15	1.28 ± 0.21	0.80 ± 0.06
UDG-C21	39.97690	−1.59003	25.96 ± 0.02	0.18 ± 0.02	1.54 ± 0.13	24.31 ± 0.15	1.55 ± 0.24	0.85 ± 0.05

Table A.1. (cont'd)

Name	R.A. (J2000)	Decl. (J2000)	$F814W$	$F814W - F105W$	$R_{\mathrm{eff,c}}{}^{a}$ [kpc]	$\langle\mu\rangle_{\mathrm{e,abs}}(r')^{b}$ [mag arcsec^{-2}]	n	b/a
UDG-C22	39.97747	−1.56852	25.17 ± 0.02	0.21 ± 0.02	6.16 ± 0.36	25.18 ± 0.08	0.82 ± 0.05	0.85 ± 0.01
UDG-C23	39.97847	−1.56356	25.79 ± 0.02	0.32 ± 0.02	2.65 ± 0.19	25.31 ± 0.07	0.35 ± 0.05	0.47 ± 0.03
UDG-C24	39.97904	−1.58595	26.50 ± 0.03	0.20 ± 0.02	1.60 ± 0.23	24.81 ± 0.25	1.79 ± 0.38	0.79 ± 0.08
UDG-C25	39.98145	−1.59366	26.27 ± 0.03	0.02 ± 0.02	1.57 ± 0.13	24.67 ± 0.12	0.80 ± 0.14	0.77 ± 0.05
UDG-C26	39.98167	−1.56965	27.02 ± 0.05	0.29 ± 0.04	1.71 ± 0.45	25.41 ± 0.32	0.40 ± 0.19	0.78 ± 0.10
UDG-C27	39.98251	−1.56423	26.51 ± 0.03	0.10 ± 0.03	1.59 ± 0.13	24.99 ± 0.13	0.91 ± 0.18	0.64 ± 0.04
UDG-C28	39.98629	−1.58198	25.71 ± 0.02	0.17 ± 0.01	1.62 ± 0.09	24.24 ± 0.08	0.88 ± 0.10	0.96 ± 0.04
UDG-C29	39.98698	−1.58227	24.29 ± 0.01	0.09 ± 0.01	2.82 ± 0.09	24.06 ± 0.05	0.99 ± 0.06	0.83 ± 0.02
UDG-C30	39.98868	−1.58373	25.89 ± 0.03	0.38 ± 0.02	2.35 ± 0.13	25.22 ± 0.08	0.52 ± 0.06	0.62 ± 0.03
UDG-C31	39.98896	−1.57945	26.27 ± 0.03	0.26 ± 0.03	1.59 ± 0.10	25.09 ± 0.09	0.49 ± 0.08	0.54 ± 0.03
UDG-C32	39.98977	−1.56513	25.19 ± 0.02	0.03 ± 0.01	2.23 ± 0.04	24.60 ± 0.07	0.21 ± 0.02	0.76 ± 0.01
UDG-C33	39.99112	−1.57224	25.40 ± 0.02	0.11 ± 0.01	1.72 ± 0.10	24.35 ± 0.09	0.64 ± 0.08	0.71 ± 0.03
UDG-C34	39.99189	−1.57429	25.67 ± 0.02	0.04 ± 0.02	2.08 ± 0.12	24.84 ± 0.08	0.61 ± 0.07	0.82 ± 0.04

Table A.2. A Catalog of UDGs in the Parallel Field of Abell 370

Name	R.A. (J2000)	Decl. (J2000)	$F814W$	$F814W - F105W$	$R_{\mathrm{eff,c}}$ [a] [kpc]	$\langle\mu\rangle_{\mathrm{e,abs}}(r')$ [b] [mag arcsec^{-2}]	n	b/a
UDG-P01	40.03918	−1.63519	27.13 ± 0.05	0.33 ± 0.05	1.69 ± 0.26	25.47 ± 0.23	0.69 ± 0.22	0.58 ± 0.08
UDG-P02	40.04298	−1.61598	24.49 ± 0.01	0.16 ± 0.01	2.25 ± 0.10	24.11 ± 0.06	0.49 ± 0.05	0.67 ± 0.02
UDG-P03	40.04494	−1.63532	25.17 ± 0.02	0.31 ± 0.01	1.85 ± 0.08	24.22 ± 0.09	0.54 ± 0.07	0.74 ± 0.03
UDG-P04	40.04976	−1.63644	26.55 ± 0.04	0.14 ± 0.03	1.58 ± 0.18	24.93 ± 0.17	0.95 ± 0.23	1.00 ± 0.10
UDG-P05	40.05123	−1.64018	25.96 ± 0.03	0.26 ± 0.02	1.66 ± 0.17	24.60 ± 0.15	0.70 ± 0.14	0.78 ± 0.06
UDG-P06	40.05204	−1.63427	26.14 ± 0.03	-0.00 ± 0.02	1.70 ± 0.30	24.72 ± 0.15	0.94 ± 0.20	0.99 ± 0.15
UDG-P07	40.05553	−1.62619	25.13 ± 0.01	0.06 ± 0.01	1.64 ± 0.09	23.86 ± 0.08	0.76 ± 0.09	0.40 ± 0.02
UDG-P08	40.06543	−1.63148	24.75 ± 0.01	0.18 ± 0.01	2.04 ± 0.09	23.97 ± 0.07	0.34 ± 0.05	0.75 ± 0.03
UDG-P09	40.06554	−1.64139	25.84 ± 0.02	0.18 ± 0.02	1.59 ± 0.16	24.48 ± 0.13	0.82 ± 0.15	0.74 ± 0.06
UDG-P10	40.06972	−1.62257	26.90 ± 0.04	-0.11 ± 0.04	1.80 ± 0.37	25.35 ± 0.36	1.60 ± 0.44	0.52 ± 0.07
UDG-P11	40.07316	−1.62275	26.01 ± 0.02	0.23 ± 0.02	2.00 ± 0.06	24.12 ± 0.06	0.34 ± 0.03	0.47 ± 0.01
UDG-P12	40.07511	−1.62316	24.58 ± 0.01	0.14 ± 0.01	2.61 ± 0.13	24.14 ± 0.07	1.01 ± 0.08	0.79 ± 0.03

Table A.3. A Catalog of LSB Dwarfs in the Central Field of Abell 370

Name	R.A. (J2000)	Decl. (J2000)	$F814W$	$F814W - F105W$	$R_{\mathrm{eff,c}}{}^{a}$ [kpc]	$\langle\mu\rangle_{\mathrm{e,abs}}(r')^{b}$ [mag arcsec^{-2}]	n	b/a
LDw-C01	39.94725	−1.58327	25.58 ± 0.02	0.06 ± 0.01	1.44 ± 0.09	24.02 ± 0.08	0.83 ± 0.10	0.63 ± 0.03
LDw-C02	39.95024	−1.58280	26.29 ± 0.02	-0.29 ± 0.02	1.09 ± 0.17	24.04 ± 0.30	2.45 ± 0.52	0.57 ± 0.07
LDw-C03	39.95126	−1.57900	25.72 ± 0.02	0.27 ± 0.01	1.39 ± 0.10	24.04 ± 0.08	1.00 ± 0.13	0.81 ± 0.04
LDw-C04	39.95405	−1.57715	25.87 ± 0.02	0.32 ± 0.01	1.22 ± 0.05	23.99 ± 0.07	0.59 ± 0.04	0.60 ± 0.02
LDw-C05	39.95444	−1.56964	26.53 ± 0.03	0.01 ± 0.02	1.28 ± 0.14	24.48 ± 0.14	1.39 ± 0.23	0.59 ± 0.05
LDw-C06	39.95529	−1.57075	25.78 ± 0.02	0.05 ± 0.02	1.40 ± 0.08	24.31 ± 0.12	0.51 ± 0.11	0.46 ± 0.02
LDw-C07	39.95654	−1.58182	25.79 ± 0.02	0.26 ± 0.01	1.26 ± 0.08	23.99 ± 0.11	0.59 ± 0.11	0.60 ± 0.03
LDw-C08	39.95708	−1.57794	25.96 ± 0.02	0.17 ± 0.02	1.48 ± 0.10	24.27 ± 0.11	1.09 ± 0.16	0.91 ± 0.05
LDw-C09	39.95860	−1.57763	26.79 ± 0.03	-0.19 ± 0.03	1.12 ± 0.15	24.49 ± 0.19	1.34 ± 0.34	0.62 ± 0.07
LDw-C10	39.95893	−1.56260	26.65 ± 0.04	0.11 ± 0.03	1.28 ± 0.06	24.60 ± 0.08	0.26 ± 0.05	0.34 ± 0.02
LDw-C11	39.95919	−1.57446	25.49 ± 0.01	0.10 ± 0.01	1.36 ± 0.06	23.96 ± 0.09	0.43 ± 0.07	0.69 ± 0.03
LDw-C12	39.95921	−1.57553	25.58 ± 0.01	0.13 ± 0.01	1.24 ± 0.51	23.92 ± 0.58	0.44 ± 0.34	0.76 ± 0.12
LDw-C13	39.96018	−1.56815	25.91 ± 0.02	0.29 ± 0.01	1.31 ± 0.18	24.01 ± 0.24	1.98 ± 0.33	0.90 ± 0.08
LDw-C14	39.96027	−1.59115	26.22 ± 0.02	0.17 ± 0.02	1.04 ± 0.09	23.97 ± 0.14	0.69 ± 0.15	0.84 ± 0.06
LDw-C15	39.96039	−1.59014	25.77 ± 0.02	0.28 ± 0.01	1.25 ± 0.08	23.99 ± 0.09	0.59 ± 0.09	0.80 ± 0.04
LDw-C16	39.96112	−1.58754	26.37 ± 0.02	-0.01 ± 0.02	1.02 ± 0.10	24.03 ± 0.13	0.86 ± 0.18	0.74 ± 0.06
LDw-C17	39.96121	−1.58554	26.89 ± 0.04	0.04 ± 0.03	1.24 ± 0.11	24.73 ± 0.13	0.43 ± 0.09	0.90 ± 0.08
LDw-C18	39.96128	−1.58562	26.15 ± 0.02	0.15 ± 0.02	1.16 ± 0.09	24.10 ± 0.13	0.63 ± 0.11	0.35 ± 0.02
LDw-C19	39.96170	−1.56769	26.29 ± 0.03	0.02 ± 0.02	1.23 ± 0.07	24.52 ± 0.10	0.56 ± 0.06	0.39 ± 0.02
LDw-C20	39.96209	−1.57524	26.56 ± 0.03	0.02 ± 0.02	1.04 ± 0.07	24.39 ± 0.13	0.26 ± 0.08	0.51 ± 0.04
LDw-C21	39.96241	−1.55540	25.98 ± 0.02	-0.00 ± 0.02	1.34 ± 0.09	24.35 ± 0.12	0.63 ± 0.12	0.49 ± 0.03

Table A.3. (cont'd)

Name	R.A. (J2000)	Decl. (J2000)	$F814W$	$F814W - F105W$	$R_{\mathrm{eff,c}}{}^{a}$ [kpc]	$\langle\mu\rangle_{\mathrm{e,abs}}(r')^{b}$ [mag arcsec^{-2}]	n	b/a
LDw-C22	39.96415	−1.58914	25.57 ± 0.02	0.13 ± 0.01	1.39 ± 0.10	24.12 ± 0.12	1.26 ± 0.19	0.61 ± 0.03
LDw-C23	39.96459	−1.59198	26.45 ± 0.03	0.17 ± 0.02	1.14 ± 0.07	24.39 ± 0.13	0.44 ± 0.12	0.52 ± 0.03
LDw-C24	39.96473	−1.58924	26.56 ± 0.03	0.25 ± 0.02	1.13 ± 0.09	24.56 ± 0.13	0.61 ± 0.12	0.71 ± 0.05
LDw-C25	39.96484	−1.59290	26.65 ± 0.03	0.08 ± 0.02	1.07 ± 0.14	24.32 ± 0.19	1.09 ± 0.27	0.51 ± 0.06
LDw-C26	39.96511	−1.59478	27.11 ± 0.04	0.17 ± 0.04	1.03 ± 0.11	24.76 ± 0.17	0.49 ± 0.14	0.80 ± 0.08
LDw-C27	39.96531	−1.57447	27.78 ± 0.06	0.14 ± 0.07	1.44 ± 0.07	25.31 ± 0.73	0.18 ± 0.05	0.61 ± 0.02
LDw-C28	39.96574	−1.55654	27.09 ± 0.05	0.09 ± 0.04	1.20 ± 0.07	25.13 ± 0.13	0.56 ± 0.10	0.66 ± 0.04
LDw-C29	39.96576	−1.58103	25.40 ± 0.01	0.27 ± 0.01	1.47 ± 0.06	23.99 ± 0.07	0.55 ± 0.06	0.72 ± 0.02
LDw-C30	39.96659	−1.55781	26.17 ± 0.02	0.15 ± 0.02	1.10 ± 0.13	23.94 ± 0.20	1.96 ± 0.38	0.54 ± 0.05
LDw-C31	39.96684	−1.57084	26.26 ± 0.02	0.26 ± 0.02	1.11 ± 0.07	24.21 ± 0.08	0.44 ± 0.06	0.82 ± 0.04
LDw-C32	39.96704	−1.56818	27.09 ± 0.04	0.10 ± 0.04	1.44 ± 0.31	24.89 ± 0.20	0.52 ± 0.16	0.43 ± 0.07
LDw-C33	39.96754	−1.59538	26.09 ± 0.02	0.13 ± 0.02	1.19 ± 0.12	24.26 ± 0.15	0.67 ± 0.17	0.84 ± 0.06
LDw-C34	39.96762	−1.56388	27.15 ± 0.05	0.00 ± 0.04	1.14 ± 0.08	25.03 ± 0.19	0.21 ± 0.06	0.57 ± 0.03
LDw-C35	39.96818	−1.58200	26.74 ± 0.03	0.00 ± 0.03	1.23 ± 0.07	24.77 ± 0.10	0.47 ± 0.06	0.68 ± 0.04
LDw-C36	39.96951	−1.57587	25.28 ± 0.01	0.30 ± 0.01	1.46 ± 0.06	23.81 ± 0.05	0.48 ± 0.03	0.96 ± 0.04
LDw-C37	39.96979	−1.58661	27.58 ± 0.05	-0.11 ± 0.06	1.20 ± 0.15	25.10 ± 0.16	0.24 ± 0.13	0.44 ± 0.06
LDw-C38	39.97017	−1.58826	26.51 ± 0.03	0.16 ± 0.02	1.03 ± 0.11	24.13 ± 0.17	1.30 ± 0.30	0.60 ± 0.06
LDw-C39	39.97107	−1.59294	25.71 ± 0.02	0.19 ± 0.01	1.40 ± 0.07	24.15 ± 0.07	0.50 ± 0.06	0.75 ± 0.03
LDw-C40	39.97170	−1.59613	25.99 ± 0.02	0.26 ± 0.02	1.34 ± 0.09	24.33 ± 0.10	0.70 ± 0.11	0.87 ± 0.06
LDw-C41	39.97173	−1.56458	26.50 ± 0.03	0.18 ± 0.03	1.20 ± 0.15	24.54 ± 0.17	1.04 ± 0.24	0.82 ± 0.09
LDw-C42	39.97178	−1.56361	26.21 ± 0.02	0.20 ± 0.02	1.05 ± 0.11	24.05 ± 0.14	0.98 ± 0.20	0.79 ± 0.06

Table A.3. (cont'd)

Name	R.A. (J2000)	Decl. (J2000)	$F814W$	$F814W - F105W$	$R_{\mathrm{eff,c}}$ [a] [kpc]	$\langle\mu\rangle_{\mathrm{e,abs}}(r')$ [b] [mag arcsec^{-2}]	n	b/a
LDw-C43	39.97212	−1.57670	27.11 ± 0.04	0.02 ± 0.04	1.10 ± 0.08	24.92 ± 0.12	0.48 ± 0.07	0.91 ± 0.06
LDw-C44	39.97219	−1.55760	25.80 ± 0.02	0.03 ± 0.01	1.36 ± 0.06	24.11 ± 0.08	0.45 ± 0.04	0.51 ± 0.02
LDw-C45	39.97283	−1.59131	26.88 ± 0.03	0.02 ± 0.03	1.10 ± 0.19	24.55 ± 0.24	1.23 ± 0.38	0.56 ± 0.07
LDw-C46	39.97292	−1.56841	26.95 ± 0.04	0.19 ± 0.03	1.05 ± 0.07	24.78 ± 0.11	0.39 ± 0.07	0.64 ± 0.04
LDw-C47	39.97334	−1.57793	26.10 ± 0.02	0.09 ± 0.02	1.05 ± 0.06	23.93 ± 0.10	0.49 ± 0.09	0.84 ± 0.04
LDw-C48	39.97367	−1.58653	26.57 ± 0.03	0.06 ± 0.03	1.06 ± 0.12	24.48 ± 0.15	0.91 ± 0.22	0.76 ± 0.06
LDw-C49	39.97424	−1.59041	27.76 ± 0.07	−0.01 ± 0.07	1.07 ± 0.27	25.23 ± 0.33	0.50 ± 0.27	0.76 ± 0.17
LDw-C50	39.97454	−1.56662	25.89 ± 0.02	0.14 ± 0.02	1.24 ± 0.13	23.98 ± 0.15	1.42 ± 0.23	0.89 ± 0.06
LDw-C51	39.97504	−1.58944	25.72 ± 0.02	0.11 ± 0.01	1.37 ± 0.09	23.99 ± 0.09	0.95 ± 0.13	0.39 ± 0.02
LDw-C52	39.97507	−1.57282	26.63 ± 0.03	0.15 ± 0.02	1.09 ± 0.08	24.49 ± 0.12	0.73 ± 0.12	0.79 ± 0.06
LDw-C53	39.97619	−1.56863	25.89 ± 0.02	0.20 ± 0.01	1.11 ± 0.08	23.88 ± 0.11	0.86 ± 0.14	0.66 ± 0.04
LDw-C54	39.97625	−1.56775	27.49 ± 0.06	0.17 ± 0.06	1.16 ± 0.18	25.28 ± 0.20	0.54 ± 0.16	0.69 ± 0.10
LDw-C55	39.97718	−1.56833	26.11 ± 0.02	0.38 ± 0.02	1.10 ± 0.28	24.23 ± 0.31	0.76 ± 0.21	0.77 ± 0.11
LDw-C56	39.97731	−1.56967	26.05 ± 0.02	−0.05 ± 0.02	1.06 ± 0.06	23.92 ± 0.11	0.42 ± 0.10	0.53 ± 0.03
LDw-C57	39.97765	−1.56119	25.86 ± 0.02	0.18 ± 0.01	1.13 ± 0.08	23.82 ± 0.11	1.09 ± 0.16	0.43 ± 0.03
LDw-C58	39.97836	−1.59729	26.66 ± 0.03	0.13 ± 0.03	1.26 ± 0.15	24.69 ± 0.14	0.99 ± 0.22	1.00 ± 0.09
LDw-C59	39.97844	−1.58836	26.21 ± 0.02	0.25 ± 0.02	1.39 ± 0.16	24.41 ± 0.15	1.15 ± 0.22	0.90 ± 0.07
LDw-C60	39.97894	−1.56264	26.32 ± 0.02	0.24 ± 0.02	1.00 ± 0.09	23.99 ± 0.12	0.84 ± 0.16	0.89 ± 0.07
LDw-C61	39.97936	−1.57982	26.37 ± 0.02	0.12 ± 0.02	1.10 ± 0.05	24.40 ± 0.09	0.38 ± 0.05	0.51 ± 0.02
LDw-C62	39.97963	−1.57271	26.44 ± 0.02	0.23 ± 0.02	1.14 ± 0.11	24.33 ± 0.13	1.19 ± 0.19	0.48 ± 0.03
LDw-C63	39.97974	−1.59216	27.26 ± 0.05	−0.01 ± 0.04	1.03 ± 0.09	24.92 ± 0.18	0.29 ± 0.13	0.94 ± 0.11

Table A.3. (cont'd)

Name	R.A. (J2000)	Decl. (J2000)	$F814W$	$F814W - F105W$	$R_{\mathrm{eff,c}}{}^{a}$ [kpc]	$\langle\mu\rangle_{\mathrm{e,abs}}(r')^{b}$ [mag arcsec^{-2}]	n	b/a
LDw-C64	39.97998	−1.57673	26.98 ± 0.04	0.14 ± 0.03	1.28 ± 0.14	24.80 ± 0.19	1.24 ± 0.30	0.73 ± 0.06
LDw-C65	39.98009	−1.57125	26.32 ± 0.03	0.27 ± 0.02	1.06 ± 0.09	24.11 ± 0.12	0.93 ± 0.17	0.79 ± 0.06
LDw-C66	39.98037	−1.59056	26.49 ± 0.02	0.19 ± 0.02	1.12 ± 0.16	24.26 ± 0.18	1.20 ± 0.27	0.83 ± 0.10
LDw-C67	39.98061	−1.56261	26.47 ± 0.02	0.07 ± 0.02	1.36 ± 0.20	24.47 ± 0.26	2.16 ± 0.45	0.72 ± 0.08
LDw-C68	39.98125	−1.56685	26.69 ± 0.04	0.07 ± 0.03	1.47 ± 0.12	25.26 ± 0.14	0.67 ± 0.14	0.58 ± 0.03
LDw-C69	39.98142	−1.56151	25.94 ± 0.02	-0.04 ± 0.02	1.28 ± 0.08	24.09 ± 0.10	0.83 ± 0.12	0.36 ± 0.02
LDw-C70	39.98150	−1.58937	26.66 ± 0.03	0.13 ± 0.03	1.20 ± 0.10	24.78 ± 0.11	0.54 ± 0.09	0.82 ± 0.06
LDw-C71	39.98207	−1.59104	26.49 ± 0.03	0.16 ± 0.03	1.12 ± 0.10	24.56 ± 0.19	0.47 ± 0.17	0.60 ± 0.04
LDw-C72	39.98207	−1.59581	26.15 ± 0.02	-0.24 ± 0.02	1.30 ± 0.14	24.41 ± 0.16	1.11 ± 0.23	0.45 ± 0.04
LDw-C73	39.98416	−1.56604	26.54 ± 0.03	0.20 ± 0.02	1.18 ± 0.09	24.45 ± 0.11	0.80 ± 0.15	0.82 ± 0.05
LDw-C74	39.98516	−1.59133	25.76 ± 0.02	-0.01 ± 0.01	1.23 ± 0.10	23.93 ± 0.12	0.93 ± 0.15	0.72 ± 0.04
LDw-C75	39.98682	−1.56735	26.68 ± 0.03	0.08 ± 0.03	1.12 ± 0.12	24.71 ± 0.16	0.49 ± 0.13	0.53 ± 0.04
LDw-C76	39.98719	−1.56585	26.50 ± 0.03	0.19 ± 0.03	1.46 ± 0.12	24.98 ± 0.13	0.62 ± 0.12	0.77 ± 0.05
LDw-C77	39.98756	−1.57207	26.07 ± 0.02	0.08 ± 0.02	1.03 ± 0.06	23.89 ± 0.09	0.43 ± 0.07	0.51 ± 0.03
LDw-C78	39.98818	−1.58240	25.66 ± 0.01	-0.45 ± 0.01	1.30 ± 0.10	23.88 ± 0.11	0.57 ± 0.10	0.64 ± 0.04
LDw-C79	39.98973	−1.58194	26.74 ± 0.03	-0.37 ± 0.03	1.35 ± 0.20	24.65 ± 0.19	1.32 ± 0.30	0.57 ± 0.07
LDw-C80	39.99185	−1.57522	26.45 ± 0.03	0.31 ± 0.02	1.02 ± 0.06	24.18 ± 0.09	0.65 ± 0.06	0.37 ± 0.02

Table A.4. A Catalog of LSB Dwarfs in the Parallel Field of Abell 370

Name	R.A. (J2000)	Decl. (J2000)	$F814W$	$F814W - F105W$	$R_{\rm eff,c}$[a] [kpc]	$\langle\mu\rangle_{\rm e,abs}(r')$[b] [mag arcsec^{-2}]	n	b/a
LDw-P01	40.03841	−1.63844	25.35 ± 0.02	−0.03 ± 0.01	1.37 ± 0.08	23.89 ± 0.10	0.64 ± 0.10	0.78 ± 0.04
LDw-P02	40.04068	−1.62495	26.41 ± 0.03	0.19 ± 0.02	1.22 ± 0.14	24.39 ± 0.14	0.64 ± 0.14	0.97 ± 0.09
LDw-P03	40.04080	−1.63529	27.38 ± 0.06	0.13 ± 0.05	1.10 ± 0.07	24.85 ± 0.12	0.46 ± 0.10	0.60 ± 0.04
LDw-P04	40.04113	−1.62559	26.38 ± 0.03	0.11 ± 0.02	1.01 ± 0.11	24.22 ± 0.17	0.58 ± 0.16	0.63 ± 0.06
LDw-P05	40.04382	−1.61977	26.67 ± 0.04	0.26 ± 0.03	1.10 ± 0.16	24.61 ± 0.22	1.00 ± 0.31	0.79 ± 0.08
LDw-P06	40.04447	−1.63674	26.24 ± 0.03	0.02 ± 0.02	1.01 ± 0.10	23.93 ± 0.14	0.76 ± 0.17	0.40 ± 0.04
LDw-P07	40.04498	−1.62001	25.86 ± 0.02	−0.01 ± 0.02	1.39 ± 0.20	23.98 ± 0.22	1.67 ± 0.31	0.59 ± 0.06
LDw-P08	40.04796	−1.63103	26.77 ± 0.04	0.27 ± 0.03	1.09 ± 0.13	24.65 ± 0.20	0.48 ± 0.15	0.34 ± 0.03
LDw-P09	40.04937	−1.64250	25.55 ± 0.02	0.00 ± 0.01	1.47 ± 0.09	24.07 ± 0.11	0.47 ± 0.08	0.86 ± 0.04
LDw-P10	40.05027	−1.63033	26.71 ± 0.04	−0.18 ± 0.03	1.08 ± 0.13	24.52 ± 0.20	0.52 ± 0.17	0.61 ± 0.07
LDw-P11	40.05146	−1.64179	26.88 ± 0.04	0.40 ± 0.03	1.08 ± 0.19	24.59 ± 0.24	0.91 ± 0.31	0.74 ± 0.11
LDw-P12	40.05170	−1.62769	26.60 ± 0.04	0.05 ± 0.03	1.27 ± 0.30	24.63 ± 0.40	0.90 ± 0.30	0.61 ± 0.08
LDw-P13	40.05426	−1.63050	26.63 ± 0.03	−0.14 ± 0.03	1.20 ± 0.18	24.43 ± 0.13	0.25 ± 0.12	0.60 ± 0.08
LDw-P14	40.05554	−1.62703	27.71 ± 0.10	0.28 ± 0.08	1.06 ± 0.40	25.48 ± 0.41	0.71 ± 0.44	0.90 ± 0.29
LDw-P15	40.05599	−1.64699	26.49 ± 0.03	0.06 ± 0.02	1.05 ± 0.16	24.13 ± 0.18	1.11 ± 0.28	0.94 ± 0.11
LDw-P16	40.05679	−1.61511	26.17 ± 0.03	−0.02 ± 0.02	1.36 ± 0.13	24.48 ± 0.12	0.61 ± 0.12	0.93 ± 0.07
LDw-P17	40.05728	−1.63752	26.32 ± 0.03	0.33 ± 0.03	1.45 ± 0.21	24.85 ± 0.19	0.91 ± 0.24	0.55 ± 0.06
LDw-P18	40.05751	−1.61837	26.41 ± 0.03	0.06 ± 0.02	1.08 ± 0.13	24.25 ± 0.18	0.92 ± 0.24	0.89 ± 0.09
LDw-P19	40.05809	−1.64830	26.52 ± 0.03	0.21 ± 0.03	1.00 ± 0.11	24.38 ± 0.20	0.41 ± 0.17	0.95 ± 0.09
LDw-P20	40.05819	−1.63034	25.84 ± 0.03	0.44 ± 0.02	1.12 ± 0.14	24.07 ± 0.19	1.22 ± 0.31	0.48 ± 0.05
LDw-P21	40.05858	−1.63605	25.70 ± 0.02	0.17 ± 0.01	1.20 ± 0.10	23.85 ± 0.12	0.79 ± 0.15	0.61 ± 0.04

Table A.4. (cont'd)

Name	R.A. (J2000)	Decl. (J2000)	$F814W$	$F814W - F105W$	$R_{\rm eff,c}{}^{a}$ [kpc]	$\langle\mu\rangle_{\rm e,abs}(r')^{b}$ [mag arcsec^{-2}]	n	b/a
LDw-P22	40.05872	−1.64700	26.71 ± 0.04	0.02 ± 0.03	1.10 ± 0.13	24.70 ± 0.19	0.49 ± 0.18	0.72 ± 0.07
LDw-P23	40.06005	−1.63322	26.62 ± 0.03	0.20 ± 0.03	1.01 ± 0.12	24.40 ± 0.20	0.53 ± 0.18	0.90 ± 0.08
LDw-P24	40.06253	−1.63382	26.01 ± 0.02	0.01 ± 0.02	1.15 ± 0.07	23.97 ± 0.11	0.27 ± 0.08	0.63 ± 0.04
LDw-P25	40.06460	−1.62331	26.59 ± 0.04	0.06 ± 0.04	1.47 ± 0.20	24.99 ± 0.22	0.54 ± 0.19	0.48 ± 0.05
LDw-P26	40.06577	−1.62326	25.83 ± 0.02	0.26 ± 0.02	1.31 ± 0.11	24.09 ± 0.11	0.88 ± 0.16	0.97 ± 0.07
LDw-P27	40.06775	−1.61435	25.97 ± 0.02	0.25 ± 0.02	1.42 ± 0.06	24.00 ± 0.11	0.48 ± 0.06	0.32 ± 0.01
LDw-P28	40.06842	−1.61912	26.64 ± 0.04	-0.08 ± 0.03	1.45 ± 0.20	24.69 ± 0.20	0.82 ± 0.20	0.42 ± 0.05
LDw-P29	40.06881	−1.61990	26.25 ± 0.03	0.35 ± 0.02	1.20 ± 0.11	24.25 ± 0.14	0.80 ± 0.16	0.58 ± 0.05
LDw-P30	40.06966	−1.61145	25.80 ± 0.02	0.33 ± 0.02	1.38 ± 0.12	24.15 ± 0.11	0.67 ± 0.11	1.00 ± 0.07
LDw-P31	40.07038	−1.62406	27.38 ± 0.06	0.22 ± 0.05	1.14 ± 0.20	24.99 ± 0.27	0.52 ± 0.20	0.40 ± 0.07
LDw-P32	40.07397	−1.62423	26.80 ± 0.04	-0.17 ± 0.03	1.09 ± 0.21	24.58 ± 0.29	1.36 ± 0.45	0.56 ± 0.10

요　　약

가스를 지닌 은하는 은하단과 같은 고밀도 환경에서 다양한 환경 효과를 받으며 가스를 잃어버린다. 환경 효과는 은하의 가스와 별에 전반적으로 큰 영향을 미치는데, 그 결과 은하단에는 다양한 은하 종족이 생겨나기도 한다. 그 중 '크고 희미한 은하 (ultra-diffuse galaxies)'와 '해파리은하 (jellyfish galaxies)'는 환경 효과를 받는 대표적인 은하 종족들이다. 크고 희미한 은하는 일반적인 왜소은하와 표면 밝기가 비슷하지만 크기가 우리은하만큼 큰 은하이다. 해파리은하는 충차압으로 인해 가스가 쓸려나가면서 새로운 별을 생성하여 꼬리 모양의 구조가 보이는 것이 특징이다. 현재까지 이 두 은하 종족에 관한 연구는 주로 가까운 우주에 있는 비교적 가벼운 은하단 위주로 이루어졌다. 본 학위논문에서는 적색이동 값이 0.3보다 더 큰 멀리 있는 무거운 은하단에서 크고 희미한 은하와 해파리은하의 특성을 연구한다. 우리는 허블 우주 망원경 영상과 제미니 망원경의 GMOS/IFU 분광 자료를 이용하여 MACS 서베이와 허블 프론티어 필드의 무거운 은하단을 탐사하였다.

첫 번째, 우리는 허블 프론티어 필드의 무거운 은하단 Abell 370에서 46개의 크고 희미한 은하를 찾아냈다. 그리고 이 샘플을 허블 프론티어 필드의 다른 두 무거운 은하단(Abell S1063과 Abell 2744)에서 찾은 크고 희미한 은하들과 합쳐서 함께 살펴보았다. 우리는 이 샘플을 바탕으로 1) 개수 밀도 분포, 2) 크고 희미한 은하의 개수와 모은하군/은하단의 질량 사이의 관계, 3) 은하의 역학적 질량 등을 분석하였다. 은하의 개수 밀도 분포를 은하단 중심으로부터 거리에 따라 그려보면, 크고 희미한 은하는 은하단 중심 영역에서 밝은 은하보다 개수 밀도가 감소하는 경향을 확인할 수 있었다. 이는 크고 희미한 은하가 은하단 중심부에서 환경 효과로 인해 대부분 파괴되었음을 의미한다. 크고 희미한 은하의 전체 개수와 모은하군/은하단의 역학적 질량은 지수가 1에 가깝게 정비례하는 상관관계가 있다. 이러한 관계는 크고 희미한 은하의 전체적인 생존 효율은 모은하군/은하단의 질량과 크게 관련이 없음을 시사한다. 크고 희미한 은하의 역학적 질량을 추정해보면 대부분은 왜소은하와 비슷하지만, 소수는 우리은하 정도로 무거운 은하도 존재한다. 이는 기존 연구들과 마찬가지로 크고 희미한 은하의 기원이 여러 갈래로 나뉠 수 있다는 의미이다. 결론적으로 무거운 은하단에 있는 크고 희미한 은하는 가까운 우주에 있는 은하들과 비슷한 성질을 지닌다.

두 번째, 우리는 무거운 은하단에 있는 해파리은하의 이온화된 가스의 특성을 제미니

망원경의 GMOS/IFU 분광 자료를 통해 분석하였다. 이 연구에서는 MACS 서베이와 허블 프론티어 필드 은하단에서 총 5개의 해파리은하(MACSJ0916-JFG1, MACSJ1752-JFG2, Abell 2744, MACSJ1258-JFG1, MACSJ1720-JFG1)를 분광 관측하였다. 이 은하들이 위치한 모은하단은 매우 무겁고 엑스선 광도도 밝아서 가까운 우주에 있는 가벼운 은하단보다 훨씬 더 강한 충차압 효과를 볼 수 있다. Hα선을 방출하는 가스의 공간 분포는 광학 영상에서 보이는 젊은 별의 공간 분포와 거의 일치한다. 이온화된 가스의 시선 속도 분포를 살펴보면 가스가 원반면에서 은하 중심을 회전하고 있음을 확인할 수 있는데, 은하 중심에서 멀리 떨어진 꼬리 부분에서는 가스가 높은 시선 속도를 보이기도 한다. 이는 충차압에 의한 효과일 가능성이 높다. 가스의 속도 분산은 별 형성 지역에서 대부분 50 km/s 이하로 일반적인 나선은하와 비슷한 값을 보였다. Hα선의 광도를 이용해 추정한 별 형성 비율은 가까운 우주에 있는 가벼운 은하단에서 발견된 해파리은하보다 훨씬 높은 값을 보여주었다. 이는 무거운 은하단의 강한 충차압으로 인해 해파리은하에서 폭발적으로 별이 만들어지고 있음을 의미한다. 결론적으로 무거운 은하단에 있는 해파리은하는 가스의 운동과 역학적 상태가 기존에 알려진 해파리은하들과 비슷하지만, 별 형성 비율은 매우 높다.

마지막으로, 우리는 해파리은하의 별 형성 활동을 모은하단의 특성과 관련 지어 더 자세히 분석하였다. 해파리은하의 별 형성 활동과 모은하단의 특성은 분명 관련이 있으리라 추측되지만 아직까지 명확한 관계가 밝혀지지는 않았다. 우리는 앞서 제미니 GMOS/IFU를 이용해 관측한 5개의 해파리은하를 이용해 기존에 알려진 해파리은하와 별 형성 활동이 어느 정도로 차이를 보이는지 확인하였다. 해파리은하의 별 형성 활동은 모은하단의 속도 분산이 클수록 활발한 경향을 보였다. 우리는 해파리은하의 별 생성 비율이 해당 적색이동에서 일반적으로 알려진 별 생성 비율과 비교해 얼마나 높은지 알아보기 위해 starburstiness를 정의하였다. 해파리 구조가 뚜렷하게 보이는 해파리은하들은 starburstiness가 모은하단의 속도 분산, 은하간물질(ICM)의 밀도, 충차압의 세기와 분명한 양의 상관관계를 보였다. 이 관계는 충차압에 의한 가스 쓸림 현상이 강할수록 해파리은하의 별 생성이 일시적으로 더 강하게 촉진된다는 사실을 의미한다.

주요어: 은하단, 환경 효과, 은하 진화, 별 형성, 크고 희미한 은하, 해파리은하, 충차압에 의한 가스 손실

학 번: 2015-22604

감 사 의 글

대학원생 꼬꼬마이던 시절, 졸업하는 선배님들의 감사의 글을 볼 때면 참 멋지다는 생각이 들었습니다. 수년간의 대학원 생활을 기어코 이겨내고 나서 남기는 화려한 피날레 같아 보였달까요. 저의 대학원 생활 또한 대부분 어렵고 힘든 시간이었지만 ‘언젠가 나도 저렇게 감사의 글을 쓰겠지’ 하고 생각하면 신기하게도 좀 더 버텨볼 힘이 났던 것 같습니다. 이래서 감사의 힘은 대단한가 봅니다.

7년 간의 대학원 생활, 그리고 인턴과 학부 졸업 연구까지 포함하면 더 긴 시간 동안 저를 지도해주신 이명균 교수님께 진심으로 감사드립니다. 오랜 시간 동안 거의 무한한 인내심으로 저의 성장 과정을 지켜봐주시고 이끌어주셨습니다. 처음 찾아뵈었을 때 허블 프론티어 필드를 직접 소개해주셨던 기억이 납니다. 돌이켜보면 저의 모든 학위 연구 주제도 거기서 출발했던 것 같아 신기합니다. 연구뿐만 아니라 인생의 다방면에서 많은 이야기를 나눌 수 있었고 저 또한 많이 배울 수 있었습니다. 선생님께서 계셨기에 저희 팀도 항상 남부럽지 않은 좋은 분위기를 유지할 수 있었다고 생각합니다.

학위 논문을 심사해주신 분들께도 감사드립니다. 항상 눈과 귀를 사로잡는 재미있는 톡을 해주셨던 임명신 교수님, 생각해보니 미디엄 밴드 특강 수업 한 번만 겹쳤던 것 같아 아쉽습니다. 학부 때부터 명강의로 저와 동기들을 이끌어주셨던 김웅태 교수님, 천문학 지식뿐만 아니라 연구자로서 살아남기 위해 지녀야 할 태도에 대해 정말 많이 배웠습니다. 대학원에 들어오자마자 인사드리게 되어 몇 달만에 탁구대회까지 같이 나갈 정도로 가까워졌던 황호성 교수님, 늘 유쾌하고 긍정적이셔서 마음이 편했고 힘이 되는 말씀을 많이 해주셔서 감사합니다. 제가 들어간 첫 콜로퀴움 때 해파리은하를 소개해주셨던 신윤경 박사님, 워크샵이나 여름학교 등에서 자주 뵙게 되어 좋았고 항상 웃으시고 친근한 느낌을 주셔서 즐겁게 얘기를 나눌 수 있었습니다.

학부 때부터 지금까지 저를 한 명의 천문학자로 성장할 수 있게 해주신 천문학과의 모든 교수님들께도 감사드립니다. 10년 넘게 받았던 가르침을 항상 새기며 살아가도록 하겠습니다. 또한 학과의 여러 일도 귀찮아 하지 않고 도맡아주셨던 행정실 선생님들과 서진국 조교님께도 감사드립니다. 대학원 생활이란 혼자 힘으로만 되는 것이 아님을 다시 한 번 느낄 수 있었습니다.

어디에 내놓아도 자랑스러울만큼 분위기가 좋은 우리 관측우주론 팀원들께도 감사드립니다. 많은 분들이 졸업을 하고 떠나셔서 팀원이 줄어든 것이 늘 아쉽습니다. 서로의 합이 너무 잘 맞아서 알게 모르게 가장 많이 의지했던 지수, 새로운 일에도 조만간 익숙해질 거야 화이팅! 유일한 팀 동기로서 함께 동고동락하며 영어 스피킹 기회도 많이 준 브라이언, 덕분에 영어도 많이 늘었고 한 학기 뒤 무사히 졸업하길 응원해요. 어려웠을 대학원 생활을 이겨내신 은총이 누나, 새로운 곳에서도 일이 잘 풀리길 바라고 파이썬도 곧 무사히 갈아타실 수 있을 거에요. 은근히 인연이 오래된 다재다능 성아, 고생 많았고 꼭 이모티콘 출시해줘, 내가 다 사줄게. 내가 존경해 마지않는 후배 유정이, LA에서도 즐겁게 보내고 있어서 뿌듯해. 긍정적이고 멋진 데이터분석가 강일이, 이제 곧 전문연도 끝이 보인다! 매사 진지하고 자신감 있는 모습이 보기 좋았던 재연이, 머나먼 호주에서 MUSE 데이터 정복하고 올 거라 믿어 의심치 않아. JWST와 함께 첫 학기를 불태우는 장호, 꾸준히 하다보면 전문가가 되어 있을 거야.

팀 선배들에게 진 빚도 다 갚지 못할 만큼 너무나 큽니다. 팀 막내 시절부터 많이 챙겨주신 삼성맨 광호형, 인턴 때 기꺼이 멘토를 맡아주셨던 주비형 (손 교수님), 박학다식하시고 분위기도 늘 띄워주시는 진혁이형, 콸콸 멤버의 핵심이자 저희 15학번 동기들을 너무나 좋아해주셨던 유경이누나, 별 측광 최고 전문가 인성이형, 선배 관측법 조교님 재형이형, 언제나 멋쟁이 룩 나원누나, 모두 언제 뵈어도 반갑게 인사드릴 수 있을 것 같습니다. 또한 저와 겹치지 않아 대학원에서 많이 뵙지는 못했지만 여기저기서 빛나고 계시는 관측우주론 팀 선배님들도 모두 존경스럽고 감사드립니다.

팀은 달라도 늘 끈끈하게 지내오고 있는 천문학과 사람들께도 감사드립니다. 2년 동안 룸메이트이자 대화도 잘 통하는 미식가 구형, 조용한 듯 은근히 재미있으신 준호형, 언제 봐도 어제 본 것처럼 사투리 쓰며 수다 떨 수 있는 상윤이, 감수성 넘치는 사진가이자 맥잘알 겨레, 듬직한 야구 포수이며 최고의 요리사 하늘이, 누구보다 생각이 깊은 청계천 러버 소피아, 배울 점이 너무나 많은 천생 학자들 윤수와 호진이, 늘 하회탈 같은 인상이어서 마음이 편해지는 상혁이, 심심하면 불쑥 찾아가 산책 토킹을 하곤 했던 건우, 정말 성실하고 둥글둥글한 운동맨 승학이, 스쿼시 프렌드이자 얘기하면 막힐 일이 없는 가인이, 그리고 조교의 서툰 진행에도 불구하고 끝까지 수업을 잘 따라와준 관측법 수강생 분들까지... 언급하고 싶은 분들이 이보다 더 많을 정도로 천문학과는 모두가 편한 친구 같았습니다. 제가 앞으로 어딜 가더라도 우리 천문학과처럼 단란한 분위기를 누리지는 못할 것 같습니다.

무뚝뚝해서 연락도 잘 하지 않는데도 늘 같이 놀아준 나의 친구들에게도 감사합니다. 11년 탁구 친구 보경이, 언젠가는 너를 이길 테다...가 아니고 이번에 함께 박사 졸업 축하해! 베스트 프렌드 민현이, 그렇게 좋아하는 아이들하고 즐겁게 어울릴 수 있는 참선생님이 곧 되리라 믿어! 1년에 한 번은 어떻게든 만나서 노는 성우, 슬기, 덕형, 문희, 다음에 모여서 놀 날이 곧 왔으면 좋겠다. 여행 동아리에서 한 조였던 추억 하나로 몇 년째 인연을 이어오고 있는 가람 누나, 승화 누나, 가끔씩 만나서 넋두리할 때가 제일 마음 편하고 즐거웠어. 모두 고맙고 앞날을 응원할게.

마지막으로 10년 넘게 타향살이를 하며 공부하는 저를 늘 응원하고 지지해주신 우리 가족들에게 감사의 말씀을 올립니다. 아들이 하는 연구를 잘 모르셔도 천문학 공부하는 걸 항상 자랑스러워 해주신 부모님, 늘 몸도 마음도 건강하시면 좋겠습니다. 요즘 통기타에 유난히 재미들리신 아버지와 서예와 수놓기의 달인이신 어머니 모두 원하는 취미 생활도 마음껏 하시면서 행복하시길 바랍니다. 무슨 얘기든 편하게 나눌 수 있는 영혼의 콤비이자 가장 가까운 친구 같은 동생 기환이, 취업 준비하느라 바쁘고 힘들텐데 잘 챙겨먹고 힘내자, 화이팅! 그리고 이보다 더 귀여울 순 없는 6살짜리 고양이 자매 천방지축이, 대학원 생활에 큰 힐링이 되어주어 고마웠어, 앞으로도 아프지 말고 건강하자구 :)

2022년 8월
이 정 환 올림